

https://dspace.org/

Investigating the strength of the scissors resonance in 151Sm

Magagula, Sebenzile Pretty Engelinah

2022
https://hdl.handle.net/10539/36974

Downloaded from a DSpace repository. https://dspace.org/

Investigating the strength of the scissors resonance in ^{151}Sm

Sebenzile Pretty Engelinah Magagula
University of the Witwatersrand, Johannesburg
1113061



Supervisor : Prof. Mathis Wiedeking
University of the Witwatersrand/iThemba LABS
Co-Supervisors: Dr. Kgashane L. Malatji
iThemba LABS
: Dr Luna Pellegri
University of the Witwatersrand/iThemba LABS

This work is based on the research supported in part by the National Research Foundation of South Africa (Grant Number: 118846) and the International Atomic Energy Agency under Research Contract 20454.

Declaration

I declare that this work is entirely mine, and every information taken from other sources has been explicitly referenced. This work is being submitted for the Master of Science degree to the University of the Witwatersrand. I have not submitted this work for any type of examination to any university previously.

Date 08 July 2022



Abstract

The isotopic chain of samarium is one of the isotopic chains with a number of stable isotopes. The scissors resonance (SR) of ^{151}Sm was studied with the aim of understanding the evolution of the SR along the Sm isotopic chain. Change in deformation of a nucleus from prolate through spherical to oblate, leads to changes in statistical properties, particularly the γ-strength function (γSF) and nuclear level density (NLD). The evolution of the resonance modes such as the SR depends on the deformation of the isotopes.
The experiment was performed at the Oslo Cyclotron laboratory where a ^{152}Sm self-supporting target was bombarded with a 13.5 MeV deuteron beam.
The reaction ^{152}Sm(d,tγ)^{151}Sm populated the nucleus of interest. An array of Sodium Iodine $\big($NaI(Tl)$\big)$ detectors, CACTUS, detected γ-rays and the silicon particle telescope array, SiRi, was used to detect charged particles in coincidence. The NLD and γSF were extracted below the neutron separation energy, S_n, using the Oslo Method.

These results were used to investigate the SR in the ^{151}Sm and the extracted B(M1) was compared to that of previously measured samarium isotopes. This study provides a near complete picture of the evolution of the SR for the Sm isotopic chain.

Dedication

I dedicate this work to my mother Maria Dudu Nkosi and my siblings Kenneth, Prudence, Thobani and Thabisile Matsaba.

Sicalo lesi kusekukhulu lokutako

Acknowledgements

"*No one who achieves success does so without acknowledging the help of others. The wise and confident acknowledge this help with gratitude*"
.....Alfred North Whitehead

I would like to extend my gratitude to the National Research Foundation of South Africa and the International Atomic Energy Agency for funding me throughout the course of this research. The University of Witwatersrand and iThemba LABS for the working space and working material they provided towards my studies.

To my principal supervisor Professor Mathis Wiedeking, thank you for being a great and patient teacher. Even though my quantum mechanics background was not so good your patience in teaching me got me this far. Thank you for making sure I had everything I needed for my work to be a success through the hardships of the pandemic. Thank you for believing in me and giving me this opportunity and building me towards my career.

To my supervisor Doctor Kgashane L. Malatji, I am very grateful for your guidance through the analysis of the data none of the work would have been possible without you. You were never too busy to help me be it day, night, weekend thank you for the long calls we had using your airtime for more than 3 hour calls, for the long zoom meetings you never complained even once. Thank you for your advises not only towards my academics but also towards life.

To both Kgashane and Mathis, thank you for caring about my general life and my well being.

My co-supervisor Doctor Luna Pellegri thank you for being my role model as a young researcher and showing me that women can strive in nuclear physics careers.

Greatful to the Oslo group for the data and the virtual meeting we had with some.

I am very greatful to my mother Ngingacalakuphi ngiyabonga kungikhulisa wangenta ngaba ngulomunftu lenginguye namuhla. Bekungekho lula kodvwa bowentangako konke lokusemandleni, kukhulu lokutako ngisatokujabulisa futi ngiyakutsandza. Ngitsembe kutsi utayibona imizamo yami.

My siblings Kenneth, Prudence, Thobani and Thabisile Matsaba ngiyabonga ngako konke, lusito lwenu ngetimali, ngokukhuluma nekungicondzisa, ningeluleka bengingeke ngibe la kube beningekho. Thabi ngema calls kungihlola nje ngiyabonga ngiswela emavi.

To my friends and colleagues Sinegugu, Refilwe and Sifundo thank you for the discussions both academical and general, Sinegugu thankyou for keeping me sane during the first stages of the pandemic when we were away from home for too long that's when we became sisters ngiyabonga kakhulu maMthembu wam.

Natasha Melody my best friend despite the long distance I have never ran short of your love thank you for the long calls and chats and always checking up on me. ndinokudawo muskana.

To my boyfriend Andile Magwaca thank you so much for allowing me to follow my career dreams while that caused us to be in a long distance relationship you never stopped supporting me. Not even one day has passed without us talking, thank you for being my emotional support, you are one of the major reasons I keep going strong enkosi Tolo.

Contents

Declaration i

Abstract ii

Dedication iii

Acknowledgements iv

List of Figures xi

List of Tables xii

Abbreviations xiii

1 Introduction 1

2 Theory 4
2.1 The Nuclear Level Density . . . 4
2.1.1 Fermi Gas model . . . 4
2.1.1.1 Back-Shifted Fermi-Gas model . . . 5
2.1.2 Rigid Moment of Inertia . . . 6
2.1.3 Constant Temperature Model . . . 8
2.2 Gamma-ray strength function . . . 9
2.3 Nuclear models . . . 9
2.4 Nuclear excitation modes . . . 13
2.4.1 Scissors resonance . . . 13
2.4.2 Paring and deformation . . . 15
2.4.3 Spin-flip resonances . . . 16
2.4.4 Low Energy Enhancement (LEE) . . . 17
2.4.5 Giant dipole resonance . . . 18
2.4.6 Pygmy dipole resonance . . . 19
2.5 Lorentzian functions . . . 19

3 The Oslo Method 21
3.1 Unfolding of the γ-ray spectra . . . 21
3.2 The folding iterative procedure . . . 23
3.3 Compton Subtraction . . . 25
3.4 The first generation γ-ray spectrum . . . 27
3.5 Extracting the nuclear level density (NLD) and the gamma strength function γSF . . . 30

3.6 Normalization of the NLD and γSF . . . 31
3.6.1 Normalization of the NLD . . . 32
3.6.2 Normalizing the γ-ray strength function . . . 32
3.7 The possible uncertainties of the Oslo method . . . 34
3.7.1 Spin and Parity distribution . . . 34
3.7.2 The Unfolding method . . . 38
3.7.3 The first-generation method . . . 38
3.7.4 The Brink hypothesis and the extraction of the NLD and γSF . . . 38

4 Experimental setup **40**
4.1 Detector systems . . . 41
4.1.1 The CACTUS detector array . . . 41
4.1.2 SiRi particle telescope . . . 41
4.1.3 Electronics . . . 43
4.2 Target and Reaction . . . 44

5 Data analysis **45**
5.1 Calibration . . . 45
5.1.1 The SiRi array . . . 45
5.2 CACTUS array . . . 48
5.3 Time Calibration . . . 51
5.4 Particle-γ coincidence Matrix . . . 52

6 Results **55**
6.1 Full energy deposits . . . 55
6.2 Over subtraction . . . 56
6.3 Extraction and normalization of the NLD and γSF . . . 59
6.4 Extracting the scissors resonance . . . 64

7 Discussion **66**

8 Summary and Conclusion **72**
8.1 Summary . . . 72
8.2 Conclusion . . . 72

Bibliography **82**

A Extra figures **83**

List of Figures

1.1 A schematic representation of the nuclear level density as a function of excitation energy. Γ is the γ-decay width and D is the level spacing, the relationship between Γ and D is shown as excitation energy (E_x) increases [4] 2

1.2 The isotopic chain of samarium showing a range from near spherical ^{144}Sm (in white) where $\beta_2 = 0$ to well deformed ^{155}Sm isotopes (in red). The values of the deformation parameter β_2 are taken from Ref. [10], $\beta_2 > 0$ means the nucleus is prolate shaped and $\beta_2 < 0$ is for oblate shaped nuclei. 2

2.1 A comparison of NLD modes namely the Constant Temperature Model(top),the Generalized Superfluid (bottom) Model and the Back-shifted Fermi gas Model(middle) [20], Where the black data represents values modified to experimental data for each nucleus, the blue data points show the global (collective) systematic values and the black line is asymptotic limit for the level density parameter. 5

2.2 A graph showing the result of different moments of inertia against mass number of the isotopes of hafnium from Ref. [19]. 7

2.3 Comparison between the Constant Temperature model and another model called the Moments method [23] 8

2.4 This diagram shows an example of the shell model and a few of the magic numbers known [26]. 10

2.5 The Nilsson diagram showing nuclei from the 82 to 126 shell gaps. The numbers in the square brackets are labels of the states, the first number is the principal quantum number N of the oscillator shell which gives information about the states parity $(-1)^N$, the last number is the component Ω which is the projection of the total angular momentum of the nucleon on the symmetry axis. The solid lines indicate states with even parity and the dotted lines indicate states with odd parity [25]. 11

2.6 Deformations of the nucleus: Prolate where $\beta < 0$ (left, maroon), spherical where $\beta = 0$ (middle, green) and oblate where $\beta > 0$ (right, blue) 11

2.7 Some of the known nuclear response modes which have been observed in the total γSF [27]. 13

2.8 The scissors resonance in macroscopic view [30], in which protons and neutrons oscillate against each other like the shears of a scissor. 14

2.9 A schematic diagram of the effects of deformation on the Ω orbits and the M1 scissors transitions [41]. 16

2.10 An example of the LEE from the work of Wiedeking et al [56] where the LEE was extracted using the X method in comparison with the work of Guttormsen et al [62] where the LEE was extracted using the Y method. Picture taken from [56] 17

2.11 The movement of neutrons and protons in the giant electric dipole resonance [30]. 18
2.12 An illustration of the motion of protons and neutrons in isoscalar (left) and isovector (right) [30]. 18
2.13 A representation of the neutron skin oscillating against an isospin neutron and proton systematic core [30]. 19

3.1 A schematic representation of the Compton scattering process where θ is the angle of the recoil electron and ϕ is the angle of the the scattered photon [75]. 22
3.2 The process of pair production, clearly showing how the scattering angle (θ) of the positron and the electron are equal [76]. 22
3.3 An illustrative picture of the energy deposited by the three interaction modes explained above, how photons interact with the detector material, resulting in full or partial γ-ray energy deposition [77]. 23
3.4 The diagram shows how continuously repeating the folding iterative procedure affects the spectrum, F_u is the same as R_u defined above [78]. . . 24
3.5 Schematic representation of the interpolation of the Compton part from the measured response functions c1 and c2 [78]. θ is scattering angle and it increases with the increase in the energy transferred to the electron. . . 24
3.6 The γ-ray spectrum through and after the Compton subtraction process raw matrix (top), Unfolded (middle) and the Primary γ-ray matrix (bottom). 26
3.7 A schematic representation of a decay cascade between excitation energies. The arrows shows γ -rays decaying from one excited state to another [72]. 29
3.8 An example of normalised NLD of neighbouring Dy isotopes, exhibiting little mass dependence at high energies [4]. 33
3.9 Diagram showing the γ-ray transmission coefficient of ^{51}V, The data points between the arrows are used to fit the exponential function to the experimental data [72]. 34
3.10 The three initial spin ranges used and their effects on NLD (left) and γSF (right). The spin ranges are $1/2 \leq J \leq 7/2$ (top), $1/2 \leq J \leq 13/2$ (middle) and $7/2 \leq J \leq 13/2$ (bottom). On the left the blue solid line represents the NLD over all the spin ranges, the dotted line is the input data for specific spin ranges. On the right the solid red line represents the input γSF. The open squares shows the smoothed first-generation data the closed squares shows the data on the specific spin range. The data displayed is for the ^{57}Fe isotope [13]. 36
3.11 Relative spin distributions for ^{44}Sc at $E_\gamma = 8.0$ MeV which are used in calculating level density at S_n [13]. 37

4.1 The facility layout at the Oslo cyclotron laboratory figure taken from [93]. 40
4.2 The NaI(Tl) multi-detector array CACTUS [72]. 41
4.3 The SiRi particle telescope (top right). Layout of the front ΔE detector (top left) and a schematic presentation of each detector strip divided into a thick back detector and a thin front detector(bottom) [94]. 42
4.4 The schematic diagram of the electronics used at the Oslo Cyclotron laboratory [95]. 43

5.1 Energy signals detected in $\Delta E-E$ detectors, showing the reaction channels before calibration, this plot is known as the banana plot for ^{152}Sm(d,X) where X = pγ, dγ, and tγ. 46
5.2 The energy detected in $\Delta E - E$ detectors, calibrated reaction channels. . 46
5.3 The range spectrum showing the depth at which each particle traveled inside the E detector, note the dotted lines are representing the particle gates for the ^{152}Sm(d, tγ)^{151}Sm reaction. 47
5.4 The energy detected in ΔE– E detectors, calibrated reaction channels plotted together with the calculated values from the kinematic calculator. . . 47
5.5 The energy detected in ΔE– E detectors, calibrated for the ^{28}Si(d,X)^{29}Si reactions, this was used to calibrate the particle detector. 48
5.6 The calibrated peak plot for the ^{28}Si(d,pγ)^{29}Si reaction, gated on the ejected protons. 48
5.7 The calibrated banana plot for the ^{152}Sm (d,tγ)^{151}Sm reaction, gated at the ejected tritons. 49
5.8 The calibrated excitation energy spectrum of the ^{152}Sm(d,tγ)^{151}Sm reaction. 49
5.9 The calibrated excitation energy spectrum of the ^{28}Si(d,pγ)^{29}Si reaction. 50
5.10 The calibrated gamma ray energy spectrum of ^{29}Si. 51
5.11 The γ-ray spectra gated at the 2028 and 4933 states as labeled, these shows how when a gate is placed on a certain excitation energy the spectrum will only retain γ-rays decaying from the gated excitation energy. 51
5.12 The ^{152}Sm(d,tγ) energy vs time matrix for the NaI(Tl) detectors before walk effect correction. 52
5.13 The ^{152}Sm(d,tγ) energy vs time matrix for the NaI(Tl) detectors after being corrected for the time walk effect. 53
5.14 The projection of the time matrix from figure 5.13, the pink lines represent the gate on the prompt peak and the black lines represent the gate on the random events which are used to reduce the background. 53
5.15 The excitation energy-γ ray energy matrix of ^{151}Sm before the application of the Oslo Method, the black diagonal line represents decays to ground state where $E_x = E_\gamma$. 54

6.1 The unfolded coincidence matrix for ^{151}Sm and the dotted line represents the S_n. It is observed that the number of counts decreases as E_x increases hence there are no counts towards and at the S_n. 55
6.2 The unfolded γ-ray spectrum for ^{151}Sm. 56
6.3 The first generation matrix of ^{151}Sm, populated through the ^{152}Sm(d,tγ) reaction. The area marked with red dots represents the energy region used to extract the NLD and γSF. 57
6.4 The first generation γ-rays spectrum of ^{151}Sm projected on the γ-ray energies E$_\gamma$. 57
6.5 Comparing the experimental first generation γ-ray spectra (blue circles) of ^{151}Sm from gated initial excitation energies E_x, to the $\rho(E_x - E_\gamma) \times T(E_\gamma)$ product (maroon solid curve). 58

6.6 The NLD of ^{151}Sm, the black full squares are the experimental NLD extracted using the Oslo method, the open square is the NLD at S_n denoted as ($\rho(S_n)$), the dotted line is the constant temperature model interpolated NLD, and the arrows indicate the normalization points used, the normalization points at low energies are chosen such that the data fits well on the known discrete states and the ones on higher energies is a pair that best align the interpolation to agree with most data points. 59
6.7 The normalized γSF of ^{151}Sm, extracted from the ^{152}Sm(d,t γ) reaction. . 60
6.8 The observed γ-ray transmission coefficient of ^{151}Sm with some of the uncertainties mentioned in Tab. 6.2. The arrows indicate the normalisation points used, see text. 61
6.9 The NLD of ^{151}Sm plotted with its lower error band and upper error band, a discrepancy is observed at lower energies around 0.1 to 0.6 MeV between the current data and the known levels, see text. 62
6.10 The extracted γSF of ^{151}Sm, including the lower and upper error bands from the uncertainties that are mentioned in Tab. 6.2. These show the possible location of each data point on account of all the possible uncertainties contributing to the data. 63
6.11 Comparison of the (d,tγ)^{151}Sm exponential γSF from the current study, with measurements of the other isotopes in the samarium isotopic chain. The data are also compared with the average resonance capture (ARC) [101] and further plotted with the Giant Electric Dipole Resonance (GEDR) [102] from the given references. 64
6.12 The extracted SR of ^{151}Sm, the teal circles represent the present experimental γSF, the black squares are used for background subtraction connected by the black solid line, the blue diamonds show the extracted SR and the orange line is the fit by the Standard Lorentzian function (SLO). 65

7.1 A comparison of the NLD of ^{152}Sm(d,tγ)^{151}Sm with measurements of (p,dγ)^{151,153}Sm [105] and (d,pγ)^{153,155}Sm [103]. 66
7.2 The experimental γSF from current ^{152}Sm(d,tγ)^{151}Sm reaction, plotted data from previously studied γSF as referenced on diagram 69
7.3 The comparison of the $B(M1)_{SR}$ strength against atomic mass number A obtained from this work (purple diamond) to teal stars [103], and red crossed squares [7]. This figure displays the trend of the B(M1) as deformation increases in the samarium isotopic chain. 70

A.1 The ^{151}Sm raw matrix with the red line representing decays to ground state where $E_g = E_x$ 83
A.2 The ^{152}Sm(d,tγ) energy vs time matrix for the NaI(Tl) detectors after being corrected for the time walk effect, with the red line showing the accuracy of the walk effect on the main events. 84

List of Tables

5.1 γ - ray photo peaks on each gated state used while calibrating the γ -ray detector array CACTUS, the information on the γ -rays and states studied was taken from [99] 50

6.1 The normalization parameters for ^{151}Sm used in this work, with D_0 and $< \Gamma_\gamma(S_n) >$ taken from Ref. [100]. σ and $\rho(S_n)$ are calculated as shown by Eq. 3.30. 60
6.2 The parameters used to obtain the error bands for the NLD and γSF of ^{151}Sm. 63

7.1 Table showing the extracted B(M1)$_{SR}$ strength for different samarium isotopes and their respective deformation parameters β_2 taken from Ref. [106] (where $\beta_2 \approx \delta^2$), the centroid energy ω_{SR} and data references. This information is compared in Fig. 7.3 70

Abbreviations

NLD Nuclear level density
γSF γ-ray strength function
SR Scissors Resonance
B(M1) Strength of the SR
PDR Pygmy Dipole Resonance
LEE Low-Energy Enhancement
GDR Giant Dipole Resonance
OCL Oslo Cyclotron Laboratory
E_x Excitation energy
E_γ Gamma ray energy
TFA Time Filter Amplifier
ADC Analog-to-Digital Converter
LED Leading Edge Discriminator
TDC Time to Digital Converter

Chapter 1

Introduction

The smallest form in which chemical elements and their isotopes can exist is called an atom. An atom is composed of a nucleus surrounded by a cloud of negatively charged particles called electrons. The nucleus is a small concentrated area of about 1.70×10^{15} m [1] at the center of the atom, which consists of neutral and positively charged subatomic particles, the neutrons and protons, respectively. The atom was discovered by Ernest Rutherford in 1911 [2, 3].
The nucleus, like the atom, also resembles a quantum system and has discrete (quantized) energy levels. When the nucleus is populated through a nuclear reaction it becomes excited.

When excited, one or more particles in the nucleus are promoted to a higher energy level. Following the reaction, the nucleus de-excites and releases either nucleons or γ-ray radiation. The emitted γ-rays can be measured individually when they are emitted from discrete levels at low excitation energies E_x. As the excitation energy rapidly increase the nuclear levels as well increases exponentially. The region where individual levels cannot be resolved because of the big decrease in the level spacing is called the quasi-continuum, the continuum is the region between the discrete state and the quasi-continuum. These individual levels overlap and cannot be resolved due to limitations of current instruments' resolution. In this regime, the γ-rays released can no longer be separately studied. Therefore, the average statistical properties become meaningful quantities. In particular, the average statistical properties of interest to this work are the Nuclear Level Density (NLD) and the γ-ray Strength Function (γSF) also known as radiative or photon strength function.

The NLD is simply an indication of the number of levels per energy bin or per unit excitation energy. The γSF expresses the average strength of γ-ray transitions from high excitation energies to lower levels and is directly related to the transition probability.
The NLD and γSF can be studied further and the γSF can be used to observe excitation energy modes such as the pygmy dipole resonances (PDR) and scissors resonances (SR). The SR was discovered in 1984 during an inelastic electron scattering experiment of ^{156}Gd [5].
The SR is observed in the excitation energy range of 2.0 MeV to 4.0 MeV for rare earth nuclei. SR occurs around low excitation energies compared to other M1 resonances such as spin flip resonances. It is also characterised by strong M1 transitions. Lastly the SR is believed to exist in all deformed nuclei and it has been mostly observed in more deformed

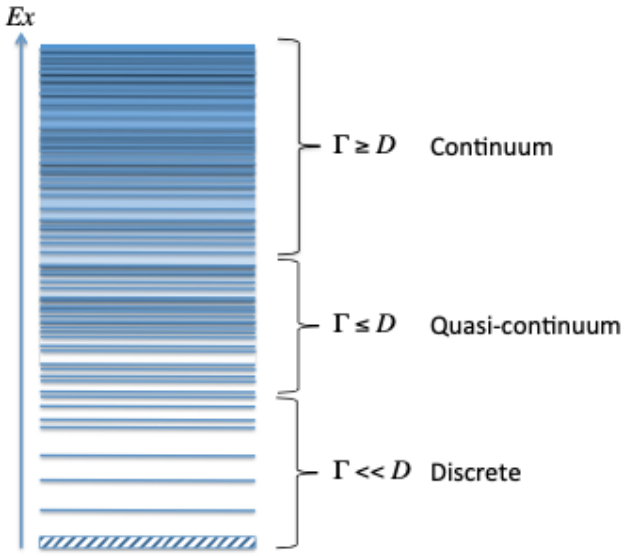


Figure 1.1: A schematic representation of the nuclear level density as a function of excitation energy. Γ is the γ-decay width and D is the level spacing, the relationship between Γ and D is shown as excitation energy (E_x) increases [4]

nuclei in comparison to less deformed nuclei [6]. The strength of the SR is proportional to the square of the ground-state deformation parameter [7]. As a result, even-even nuclei were initially considered the best candidates to exhibit well-developed SR modes. More information on the scissors resonance is discussed in Sec.2.4.1. It was soon discovered that this mode is also found in even-odd and odd-odd systems, even though its intensity might be significantly fragmented making it not to be easily detected [8, 9].

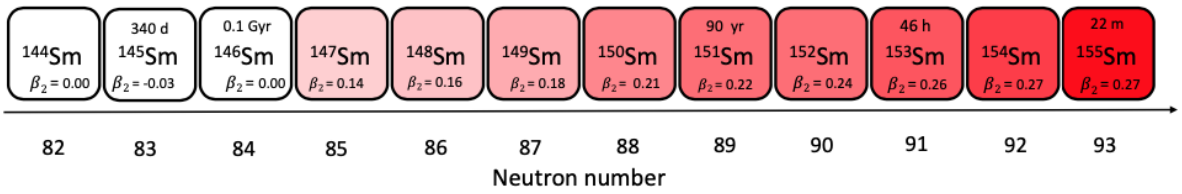


Figure 1.2: The isotopic chain of samarium showing a range from near spherical ^{144}Sm (in white) where $\beta_2 = 0$ to well deformed ^{155}Sm isotopes (in red). The values of the deformation parameter β_2 are taken from Ref. [10], $\beta_2 > 0$ means the nucleus is prolate shaped and $\beta_2 < 0$ is for oblate shaped nuclei.

The rule of deformation squared, called the "δ^2 law", states that the strength of the SR is directly proportional to the square of the deformation parameter, and it is given as follows [6]:

$$\sum_f B_f(M1) \uparrow \sim B(E2; 0_1^+ \longrightarrow 2_1^+) \sim \delta^2, \tag{1.1}$$

where $\delta^2 \approx 3/4 \times \sqrt{5/\pi} \times \beta_2$ is the nuclear ground state's quadrupole deformation, approximated to first order f. β_2 is the axial deformation parameter [10, 11], and $B_f(M1)$ is the reduced transition strength of the SR.

The changes of the strength of the SR along an isotopic chain and how these changes are impacted by deformation will be investigated using the samarium isotopic chain. Samarium is one of the elements that has a number of stable isotopes which range from near oblate through spherical to prolate nuclei as shown in Fig. 1.2 . ^{151}Sm the nuclei of interest is an even-odd system.
In this thesis the answer to the following question will be presented. How is the strength of the SR affected as deformation changes in comparison to neighboring Sm isotopes? This will be done by comparing results from this study to previous studies of other isotopes of samarium.
The aim and objectives of this project are to extract the average electromagnetic properties, the NLD and γSF of the samarium (Sm) isotope ^{151}Sm using the analytical technique, the Oslo Method [12, 13]. The γSF in particular will be used to investigate the evolution of the SR in the Sm isotopic chain. The objectives of this work are:

- To measure the strength of the scissors resonance in the above nucleus.
- To compare the results obtained to other measurements in order to investigate how the SR changes as a function of deformation across the isotopic chain.

Chapter 2

Theory

2.1 The Nuclear Level Density

The number of quantum levels at a clearly defined excitation energy within a given energy bin, is known as the nuclear level density (NLD). The amount of quasi-particles available is the basis for determining the NLD.
A cooper pair is a set of two fermions that are bound together at low temperatures (below 93K) in a certain way, which was first described by Leon Cooper in 1956 [14].
Additional states in the nucleus are created when the nucleon cooper pairs with angular momentum equal to zero (J=0) break. The free nucleons then get exited to the available single particle levels around the Fermi surface, leading to the exponential increase of the NLD [15].
The following subsections will describe in detail the NLD models that are important in this study. These models are the Constant Temperature model [16], Fermi-Gas model [17], Back-Shifted Fermi-Gas model [18] and the rigid moment of inertia (RMI) [19]. Studies have repeatedly proven the functionality of these models such as Ref. [20] and references therein.

2.1.1 Fermi Gas model

The Fermi-Gas model was brought forward in 1936 by Bethe [17]. In this model Bethe illustrates the nucleus as a free non-interacting gas of fermions which are allocated separately in single particle orbits of equal energy spacing. Starting from an individual particle picture and using Fermi statistics, Bethe calculated the level density as a function of excitation energy as shown below [17].

$$\rho(E_x) = \frac{\sqrt{\pi}}{12} \frac{exp(2\sqrt{aE_x})}{a^{1/4}E_x^{5/4}}, \tag{2.1}$$

where E_x is the excitation energy and a denotes the level density parameter and it is adjustable to allow fitting to available experimental data [21]. Like all scientific models none is precise, so the shortcomings of this model include that factors such as pairing correlations, collective phenomena and shell-effects are not taken into account during the prediction. The above information leads to the further developed version of this model called the Back-Shifted Fermi-Gas model (BSFG) [18].

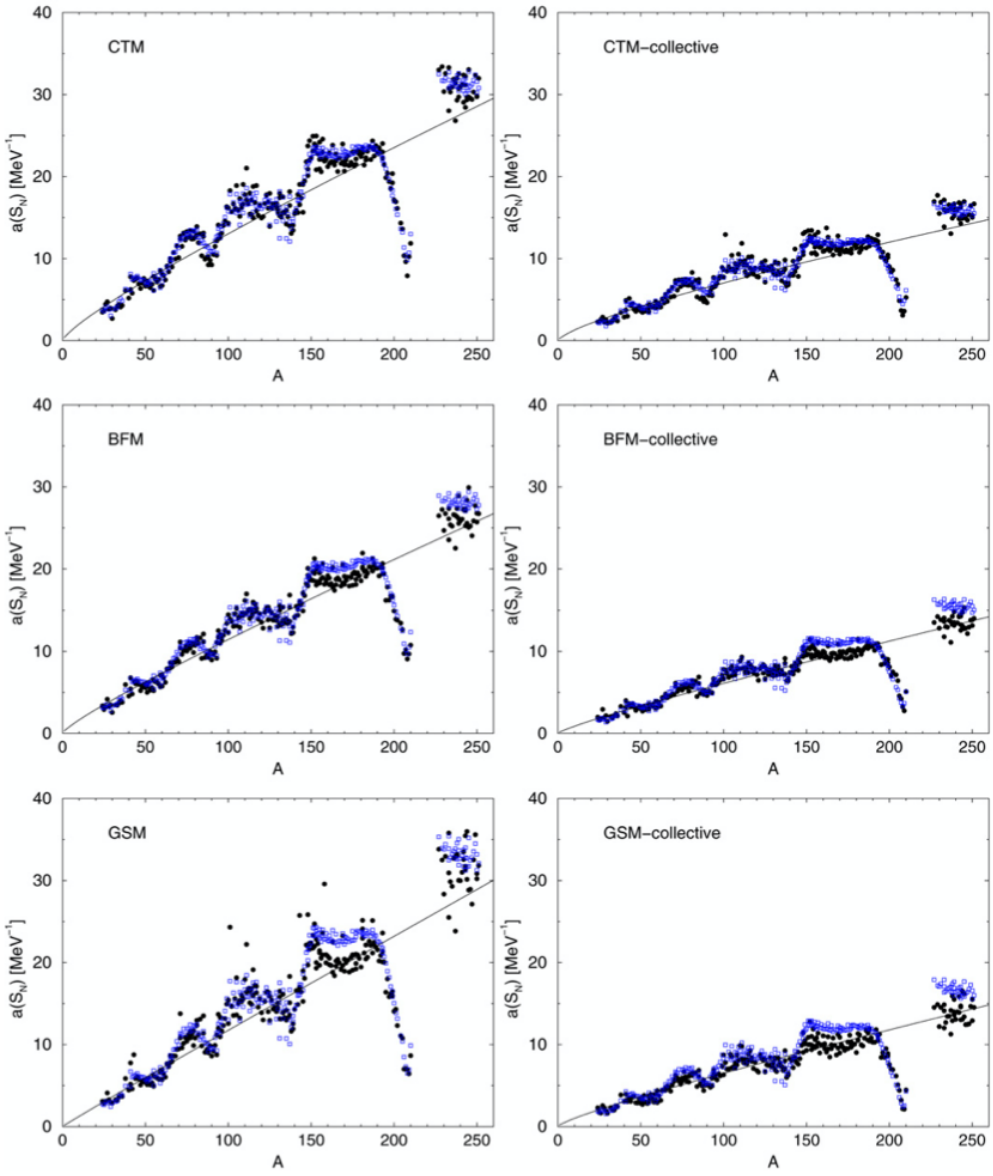


Figure 2.1: A comparison of NLD modes namely the Constant Temperature Model(top),the Generalized Superfluid (bottom) Model and the Back-shifted Fermi gas Model(middle) [20], Where the black data represents values modified to experimental data for each nucleus, the blue data points show the global (collective) systematic values and the black line is asymptotic limit for the level density parameter.

2.1.1.1 Back-Shifted Fermi-Gas model

This is a modified version of the Fermi Gas Model. In the Back-Shifted Fermi-Gas model shown in Fig. 2.1 the energy shift and level-density parameters are treated as free parameters. It is called back shifted because of the excitation energy E_x being shifted by Δ, the pairing energy of the proton and the neutron. This is done so that the model achieves better agreement with experimental results. The shift turns out to be too large such that it has to be back shifted. The model is given by the following equation [18]:

$$\rho(E_x, J) = \frac{(2J+1)exp\left(-\frac{\left(J+\frac{1}{2}\right)^2}{2\sigma^2}\right)}{2\sqrt{2\pi}\sigma^3} \frac{\sqrt{\pi}exp\left(2\sqrt{aU}\right)}{12a^{\frac{1}{4}}U^{\frac{5}{4}}}, \tag{2.2}$$

where $U = E_x - \Delta$, J is the angular momentum for all parities and σ is the spin cut-off parameter [18]. By integrating the above equation over all possible angular momenta the level density can be obtained as follows [18]:

$$\rho(E_x) = \frac{exp\left(2\sqrt{aU}\right)}{12a^{\frac{1}{4}}U^{\frac{5}{4}}\sqrt{2}\sigma}. \tag{2.3}$$

This model is used to calculate the nuclear level density using the angular momentum, the spin cut off parameter and the level density parameter as input parameters [16, 18].

2.1.2 Rigid Moment of Inertia

A rotational band reflects the collective motion of the nucleus, which alters the system's orientation without affecting its intrinsic structure or shape. Whenever all particles of a body take part in rotation and have the same angular velocity (ω) that situation can be described by the rigid moment of inertia (RMI) implying the moment of inertia of a rigid body. The angular momentum in this case is given as $J = \omega I_0$ and I_0 is the moment of inertia. The RMI plays an important role in the study of the NLD which in turn plays a big role in studies about nuclear structure [19].
The NLD can be used to determine the nuclear temperature in the following way [19]:

$$\frac{1}{T} = \frac{d}{dE} ln\big(\rho(E)\big), \tag{2.4}$$

where T is the nuclear temperature and $\rho(E)$ is the NLD at excitation energy E. Integrating over Eq. (2.4) produces the Fermi gas formula as follows [19]:

$$\rho(E) = \frac{1}{T} exp\left[\left(\frac{E-E_0}{T}\right)\right], \tag{2.5}$$

where E_0 is the ground state back shift energy. T and E_0 depend on the reaction being analyzed. Considering Bethe's level density formula for the Back-Shifted Fermi Gas model. If $U = E - E_1$ then Eq. (2.3) can be written as follows [19]:

$$\rho(E) = \frac{exp\left(2\sqrt{E-E_1}\right)}{12\sqrt{2}\sigma a^{1/4}(E-E_1)^{5/4}}, \tag{2.6}$$

Where a is the level density parameter and can be obtained from the reaction being studied at a time, the spin cut-off parameter σ^2 is used to determine the spin distribution.

$$f(s) = \frac{2s+1}{2\sigma^2} exp\left[-\frac{(s+1/2)^2}{2\sigma^2}\right], \tag{2.7}$$

where s is the spin and the spin-dependent level density is given as follows [19]:

$$\rho(E, s) = \rho(E) f(s). \tag{2.8}$$

The relationship between the spin cut-off parameter, the effective moment of inertia which is the reasonable approximation of all I towards the center of any deformed body, now the nuclear temperature is given as follows [19]:

$$\sigma^2 = \frac{I_{eff}T}{\hbar^2}. \tag{2.9}$$

Therefore the moment of inertia for a rigid body is given as [19]:

$$I_{rigid} = \frac{2}{5}MR^2, \tag{2.10}$$

where M is equal to the mass number (A) of the isotope being studied, R is the radius of the nucleus, and $\sigma^2 = 0.0150A^{5/3}T$.

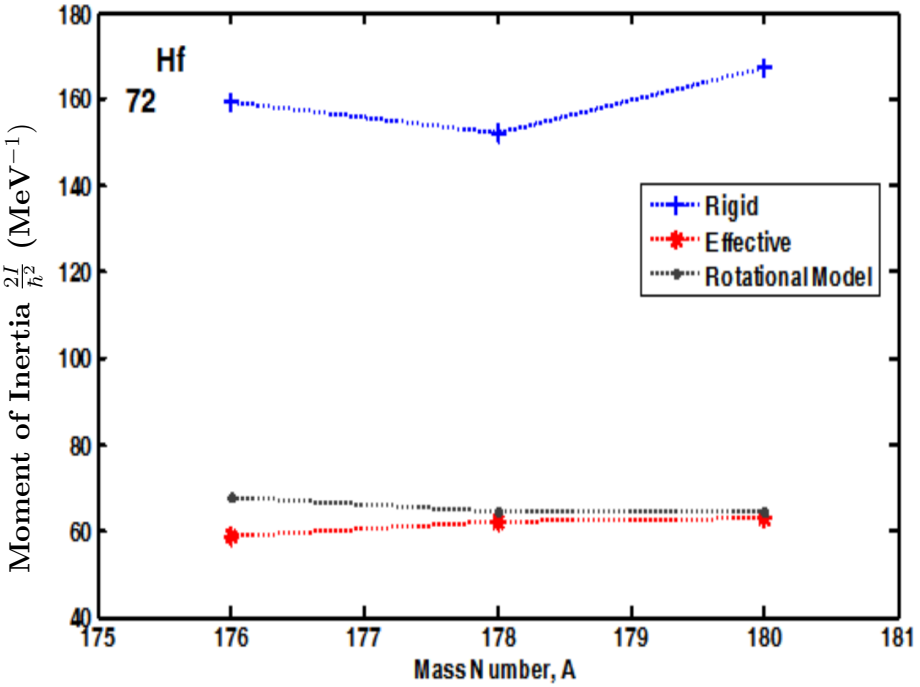


Figure 2.2: A graph showing the result of different moments of inertia against mass number of the isotopes of hafnium from Ref. [19].

The relationship between the moment of inertia of a rigid body and nuclear deformation has been studied [22] and it is now known that the RMI is inversely dependent on nuclear deformation, as shown in Fig.2.2 it is notable that the most deformed isotope ^{178}Hf has the least value of RMI.
To illustrate the relationship of these macroscopic quantities mathematically, consider the case of an axial symmetry, an ellipsoid is given as [22]:

$$\frac{x^2+y^2}{a^2} + \frac{z^2}{c^2} = 1, \tag{2.11}$$

where a and c are the semi-axis of the ellipsoid. Now to calculate the moment of inertia for a rigid ellipsoid with respect to the y- or x-axis the following equation can be used [22]:

$$I_{rigid} = I_0\frac{a^2+c^2}{2R_0^2}, \tag{2.12}$$

where $I_0 = \frac{2}{5}MAR_0^2$ represents the moment of inertia for a rigid sphere with a radius R_0. Representing the semi-axes of the ellipsoid in terms of the deformation parameter ϵ it is given as follows [22]:

$$I_{rigid} = I_0 F(\epsilon), \tag{2.13}$$

where

$$F(\epsilon) = \frac{1 - \frac{1}{3}\epsilon + \frac{5}{18}\epsilon^2}{\left(1 + \frac{1}{3}\epsilon\right)^{2/5}\left(1 - \frac{1}{3}\epsilon\right)^{4/2}}. \tag{2.14}$$

$F(\epsilon)$ is the function of the deformation parameter, where $\epsilon \approx \delta \approx 3/4 \times \sqrt{5/\pi} \times \beta$.

2.1.3 Constant Temperature Model

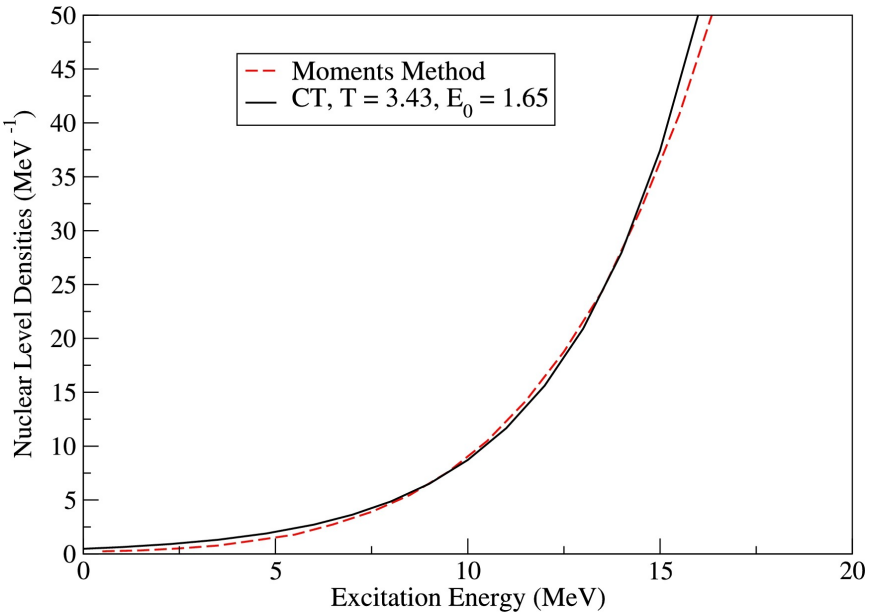


Figure 2.3: Comparison between the Constant Temperature model and another model called the Moments method [23]

The NLD below the neutron separation energy can be described by the Constant Temperature model at energies below 10MeV to be specific [18]. This represents the NLD at all possible angular momenta as follows:

$$\rho(E_x) = \frac{exp\left(\frac{E_x - E_0}{T}\right)}{T}, \tag{2.15}$$

where E_x is excitation energy, E_0 is the energy shift and T is the nuclear temperature parameter which are treated as free parameters.
Mostly when this different models are compared there is always some small negligible difference in the interpolation as we can see in Fig.2.3.

2.2 Gamma-ray strength function

The gamma-ray strength function (γSF) is a characteristic of the average electromagnetic transition properties of excited nuclei. When radiative decay takes place a γ-ray is emitted from the nucleus and a transition connects a high energy state to a low lying energy state. When photo-absorption takes place a photon (γ-ray) is absorbed and a transition connects a low lying energy state to a high energy state [24].
For radiative decay, the γSF is mathematically denoted as follows [24]:

$$f_{XL}(E_\gamma) = \frac{< \Gamma_{\gamma l} >}{E_\gamma^{2L+1} D_l}. \tag{2.16}$$

Here, X is the electric (E) or magnetic (M) character of the emitted radiation, L is the multipolarity and E_γ is the γ-ray energy. $< \Gamma_{\gamma l} >$ is the average radiative width and D_l is the resonance spacing for l-wave resonances.
For photo-absorption the γSF is given as follows [24]:

$$f_{XL}(E_\gamma) = \frac{< \sigma_{XL}(E_\gamma) >}{(2L+1)(\pi\hbar c)^2 E_\gamma^{2L-1}}, \tag{2.17}$$

where $< \sigma_{XL}(E_\gamma) >$ is the average photo-absorption cross section.
The γ-ray attenuation or γ-ray transmission coefficient is the function of a beam of gamma rays emitted or scattered per unit thickness of the detector. The relationship between the γ-ray transmission coefficient $T_{XL}(E_\gamma)$ and the γSF is given as follows [24]:

$$T_{XL}(E_\gamma) = 2\pi E_\gamma^{(2L+1)} f_{XL}(E_\gamma). \tag{2.18}$$

2.3 Nuclear models

There are many models used to describe the nucleus. In this section two models used in this study, which are the shell structure model and the Nilsson diagram, will be discussed. The shell model is similar to the atomic structure as mentioned in Chapter 1. In the case of a nuclear shell structure, for a nucleus to have stable nuclear configurations, the nucleus must have the same number of neutrons as protons ($N = Z$) and this number must correspond to either of the magic numbers. A magic number is a number of nucleons that results to the nucleons being arranged in complete shells inside the nucleus [25], these numbers are 2, 8, 20, 28, 50, 82 and 126 as shown in Fig.2.4. Whenever the number of protons, neutrons or both correspond to a magic number, the nucleus has the following properties:

- It is extremely stable,
- Has many stable isotopes and isotones, and
- A spherical charge distribution.

Examples of such nuclei include helium ($N = 2, Z = 2$), oxygen ($N = 8, Z = 8$) and many more. In fact, the two examples are double magic nuclei, nuclei are called doubly magic if they have both neutron number and proton number equal to magic numbers [25]. Radioactive decay series refers to naturally occurring decay successions, wherein a larger

nucleus undergoes progressive radioactive disintegration and stops decaying when a stable smaller nucleus is reached. The following are examples of radioactive decay series, the uranium decay series, thorium decay series and actinium decay series. Another interesting property linked to magic numbers is known as electric quadrupole moment.

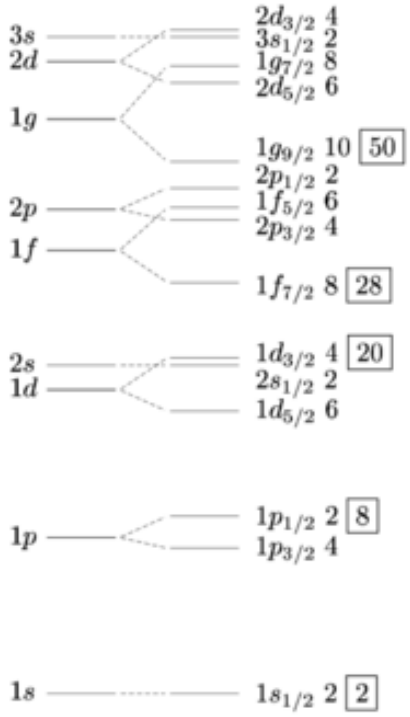


Figure 2.4: This diagram shows an example of the shell model and a few of the magic numbers known [26].

The Nilsson diagram is the first model that was used to describe the nucleus as a deformed sphere, see Fig.2.5.

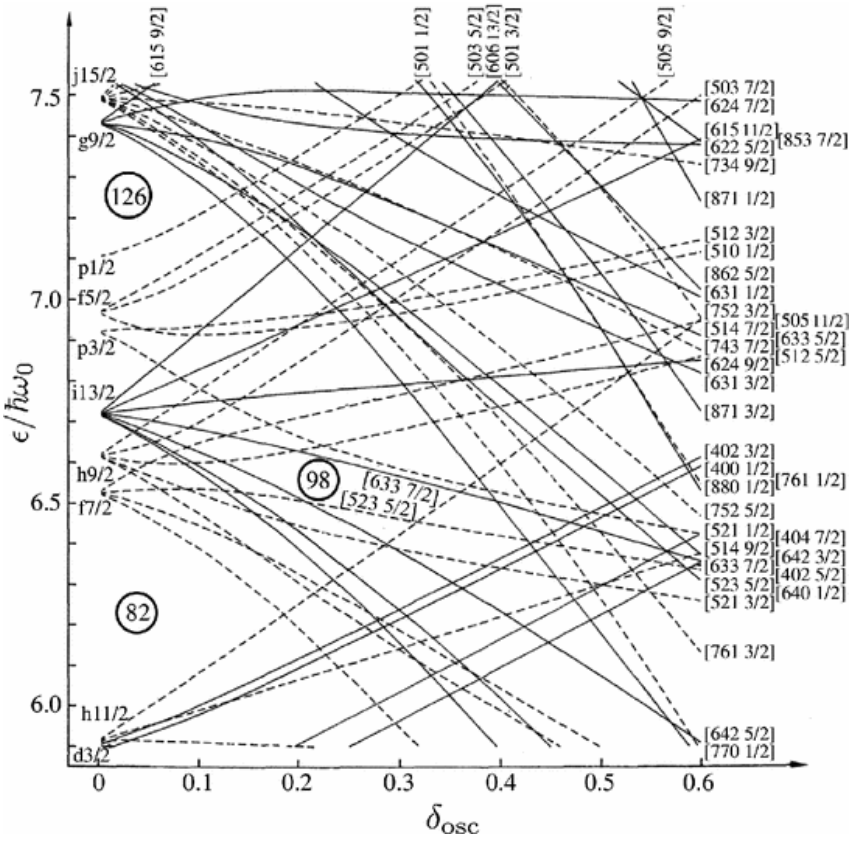


Figure 2.5: The Nilsson diagram showing nuclei from the 82 to 126 shell gaps. The numbers in the square brackets are labels of the states, the first number is the principal quantum number N of the oscillator shell which gives information about the states parity $(-1)^N$, the last number is the component Ω which is the projection of the total angular momentum of the nucleon on the symmetry axis. The solid lines indicate states with even parity and the dotted lines indicate states with odd parity [25].

β is used to represent the eccentricity of ellipsoid deformation [25] where $\epsilon \approx \delta \approx 3/4 \times \sqrt{5/\pi} \times \beta$. Deformed nuclei with $\beta > 0$ are prolate shaped and the ones with $\beta < 0$ are oblate shaped as shown in Fig. 2.6. Mathematically deformation will be described as follows, let $\omega_x\omega_y\omega_z = \omega_0^3$ where the constant ω_0 is related to the mass number, and described as: $\hbar\omega_0 = 41A^{1/3}$. If the nuclear axes are assumed to be related as $\omega_x = \omega_y \neq \omega_z$. So for oblate the equation will be $\omega_x = \omega_y > \omega_z$ meaning the nucleus will be longer along the z-axes and shorter along x and y axes. For prolate shape we have $\omega_x = \omega_y < \omega_z$ meaning the z-axes is shorter than the x and y-axes.

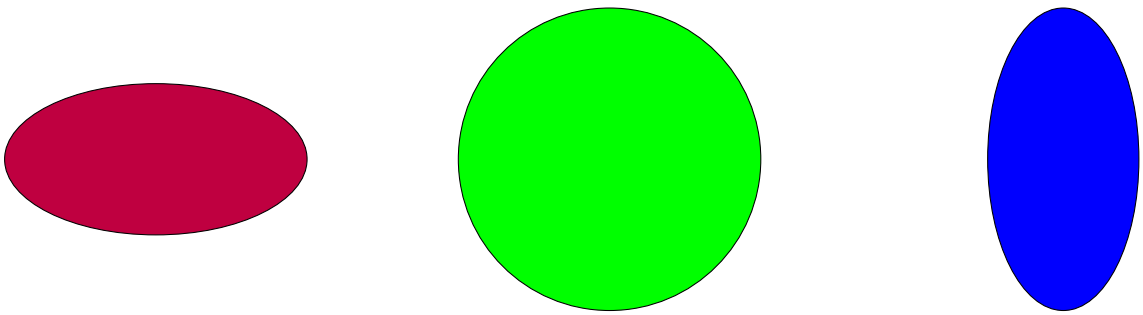


Figure 2.6: Deformations of the nucleus: Prolate where $\beta < 0$ (left, maroon), spherical where $\beta = 0$ (middle, green) and oblate where $\beta > 0$ (right, blue)

Deformed nuclei are often found in the rare-earth region and actinide region. The nuclei in these regions do not have filled proton and neutron shells. Rotations are only observed in deformed nuclei, since rotation can only take place where the x- and y-axis are not equal in length with the z-axis. The nucleus has to rotate around some of the axes which cannot happen in perfectly spherical nuclei. Rotational energy is given as follows [25]:

$$E = \frac{\hbar^2}{2I} J(J+1). \tag{2.19}$$

here I is the moment of inertia and J is the angular momentum.

2.4 Nuclear excitation modes

In this section, different nuclear excitation modes, resonances and their properties will be discussed. Fig.2.7 shows all the nuclear excitation modes to be discussed in this section, and their E_x against γSF.

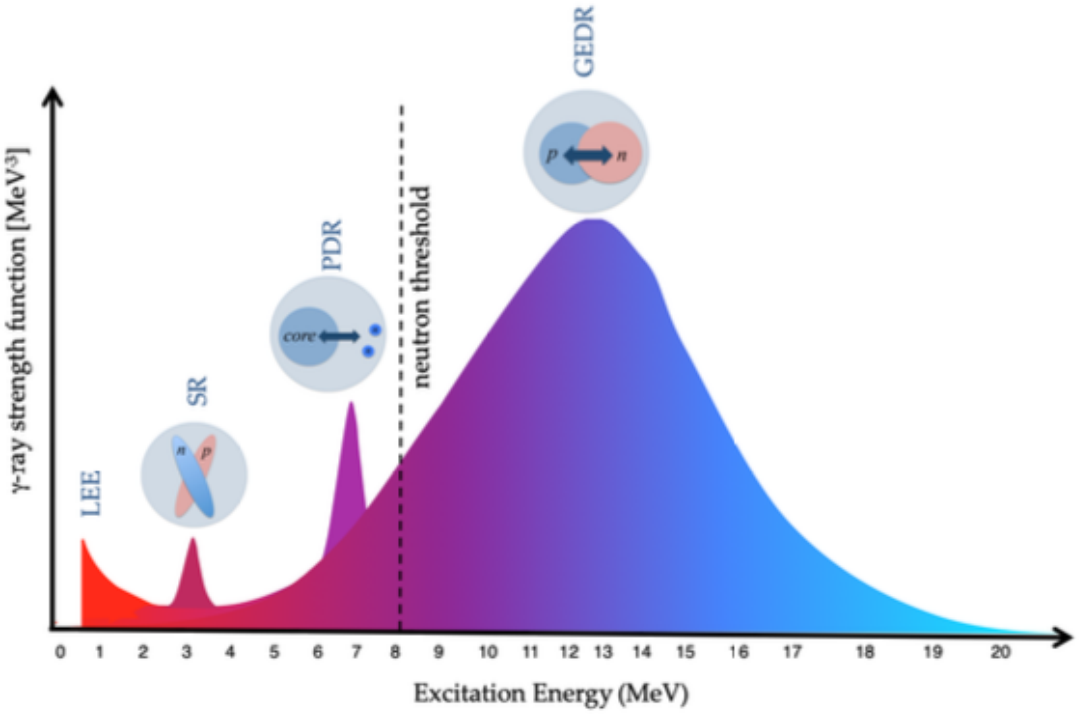


Figure 2.7: Some of the known nuclear response modes which have been observed in the total γSF [27].

2.4.1 Scissors resonance

The scissors resonance (SR) is described by the two-rotor model as a result of the distribution of protons and neutrons oscillating against each other like the blades of a scissor [28, 29]. Fig.2.8 illustrates the SR in this macroscopic view. The microscopic model illustrates transitions in high-j orbitals, represented by quantum number Ω, and deformation parameter represented by ϵ_2 in Fig.2.9 (ϵ_2 is similar to β_2).
The SR is an excitation mode that is mostly dominated by single-particle events [31]. The transitions that gives rise to the SR are found between magnetic substates that differ by one unit of angular momentum. This transition corresponds to $\Omega \pm 1$ in Fig 2.9. In the Nilsson [25] diagram, these are the transitions with similar spherical j components.
The centroid of the scissors resonance is usually found at excitation energies given as follows [31]:

$$E_x \simeq 66\delta A^{-1/3} \text{ MeV}, \tag{2.20}$$

where δ is the ground state quadrupole deformation parameter.
In calculating the axial deformation parameter β_2 [32] the Cogny effective nucleon-nucleon interaction [32] calculations of the axially symmetric Hartree-Fock-Bogoliubov (HFB) is

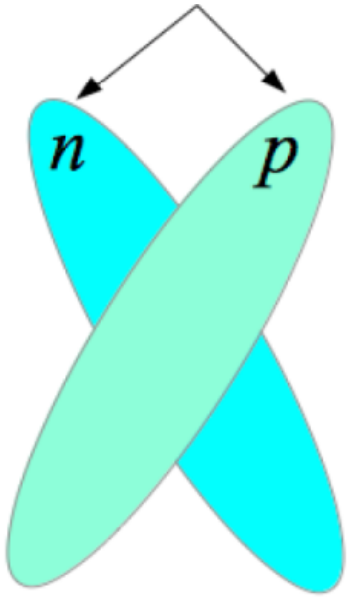


Figure 2.8: The scissors resonance in macroscopic view [30], in which protons and neutrons oscillate against each other like the shears of a scissor.

used in Ref. [33] and references therein. This parameter is also related to δ in the following way [34],

$$\beta_2 = \sqrt{\frac{\pi}{5}}\frac{4}{3}\delta. \tag{2.21}$$

The strength of the scissors resonance "B(M1)" is calculated as follows [35].

$$B(M1) = \frac{9\hbar c}{32\pi^2}\left(\frac{\sigma\Gamma}{\omega}\right). \tag{2.22}$$

Here ω is the resonance centroid energy (MeV), σ is the cross section (mb) and Γ is the radiative width(MeV). The inversely S_{+1} and linearly S_{-1} energy-weighted sum rules where S_j is the product sum of transition strengths by the j power of the corresponding E_x, these sum rules are used to calculate the B(M1) value and energy centroid as follows [35].

$$S_{+1} = \frac{3}{8\pi}\Theta_{rigid}\delta^2\omega_D^2(g_p - g_n)^2 \ \ [\mu_{\mathrm{N}}^2\mathrm{MeV}^{-1}], \tag{2.23}$$

and

$$S_{-1} = \frac{3}{16\pi}\Theta_{IV}(g_p - g_n)^2 \ \ [\mu_{\mathrm{N}}^2\mathrm{MeV}^{-1}], \tag{2.24}$$

where $(g_p - g_n)$ is approximately equal to $\frac{2Z}{A}$, Θ_{rigid} and Θ_{IV} are the rigid moment of inertia and the isovector moment of inertia [35]. Since the SR is measured in the quasicontinuum Θ_{rigid} and Θ_{IV} are taken to be equal, see Ref. [35, 36] for more information.

$$\Theta_{rigid} = \frac{2}{5}m_N r_0^2 A^{5/3}(1 + 0.31\delta), \tag{2.25}$$

here m_N is the mass of the nucleon, r_0 is the radius in (fm) [35]. The isovector giant quadrupole resonance K = 1 component will have a lot of influence on S_{+1} so it must be removed by the use of a reduction factor ξ which is represented as follows [35, 36].

$$\xi = \frac{\omega_Q^2}{\omega_Q^2 + 2\omega_D^2}. \tag{2.26}$$

The reduction factor depends on the energy centroids of the isoscalar giant quadrupole resonance ω_D and the isovector giant dipole resonance ω_Q which are approximated as follows [35]:

$$\omega_D \approx (31.2A^{-1/3} + 20.6A^{-1/6})(1 - 0.61\delta) \text{ MeV}, \tag{2.27}$$

and

$$\omega_Q \approx 64.7A^{-1/3}(1 - 0.3\delta) \text{ MeV}. \tag{2.28}$$

δ is defined as $\delta \approx \epsilon \approx \beta_2 \times \sqrt{45/16\pi}$.
The sum rules given above can be used to calculate the energy centroid of the scissors resonance ω_{SR} and resonance strength which is B_{SR} [35], using the following equations:

$$\omega_{SR} = \sqrt{\frac{S_{+1}}{S_{-1}}} = |\delta|\omega_D\sqrt{2\xi}, \tag{2.29}$$

and

$$B_{SR} = \sqrt{S_{+1}S_{-1}} = \frac{3}{4\pi}\left(\frac{Z}{A}\right)^2 \Theta_{rigid}\omega_{SR}. \tag{2.30}$$

The scissors resonance was firstly discovered in the rare-earth isotopes and a few actinides. The SR is more prominent in more deformed systems than in less deformed systems [35]. This does not mean that the resonance may not exist in less deformed nuclei such as vibrational [37], transitional [38] and γ-soft nuclei [39]. Because of the loss of axial symmetry the decay properties of transitional nuclei and a well deformed nuclei are different. For γ-soft nuclei the M1 strength distribution is reduced [40] due to difference in symmetry of heavy stable nuclei. The strength of the scissors resonance in odd-even nuclei is expected to be similar to that in even-even nuclei [9], but because of the fragmentation of the scissors resonance, a great amount or part of it lies below experimental detection thresholds [8]. When the odd-particle couples with the 1^+ modes in odd-even nuclei it creates a large fragmentation in the M1 strength distribution for some nuclei. In some other nuclei, the M1 strength is localized, but has decreased strength.

2.4.2 Paring and deformation

It is clear that magnetic dipole strength correlates strongly with deformation. The shell model have been used to explain the correlation in the case of less deformed nuclei. For the case of more deformed nuclei, the Nilsson model has been used [41]. The M1 transition strength between Nilsson orbitals differentiated by the orbits Ω in a quadrupole deformed potential is expressed as follows [6]:

$$B(M1) = \frac{3}{4\pi}(u_1v_2 - u_2v_1)^2| < \Omega_1|g_l\hat{l} + g_s\hat{s}|\Omega_2 > |^2, \tag{2.31}$$

where v_1 and v_2 are the occupation probabilities of the Nilsson orbits Ω_1 and Ω_2. Also $u_1 = 1 - v_1$ similarly with u_2. In this equation the paring factor is represented by the first term and the transition matrix element between the orbits is represented by the second term [41]. The orbitals spread out in energy as deformation increases as shown in Fig 2.9. The transition strengths are suppressed by the pair distribution over the orbitals.

The pairing factor increases with an increase in deformation, and the magnetic strength is directly proportional to the orbital strength and the deformation [41].

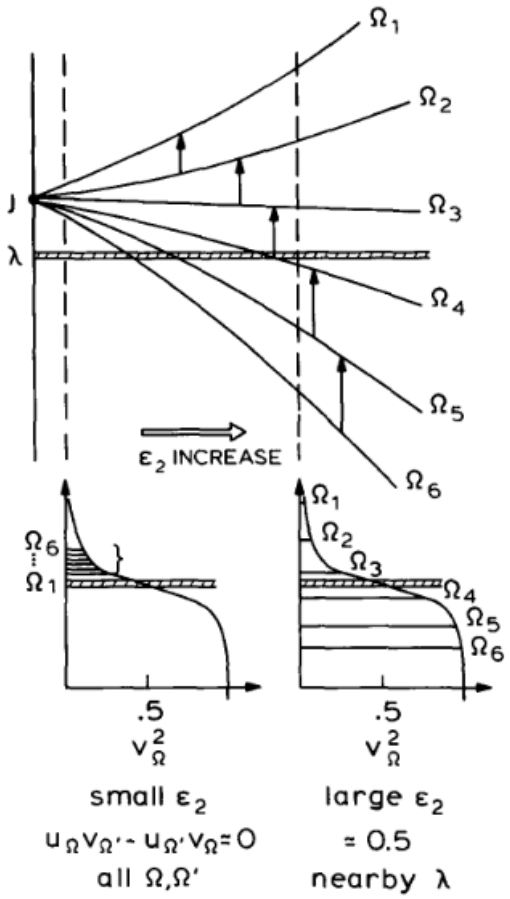


Figure 2.9: A schematic diagram of the effects of deformation on the Ω orbits and the M1 scissors transitions [41].

Methods and codes such as the KSHELL [42] an efficient M-scheme of the shell model are also successfully used in the calculations of the B(M1) [43]. The KSHELL model's space is reduced by limiting proton excitation to the $g_{9/2}$ orbital, this is done to ease computation. Reducing the space works for isotopes of proton number 29 (Cu isotopes) but has not yet been tested for isotopes of $Z > 29$.

2.4.3 Spin-flip resonances

Spin-flip resonances are formed by single particle transitions of the nature (J = l - 1/2) to (J = l + 1/2) governed by the spin orbit interaction. The single-particle model, the QRPA (Qausi-particle Random Phase Approximation) and QTDA (Quasi-particle Tamm-Dancoff Approximation) have been used to study the strength, centroid energy [44] and strength distribution of the spin flip resonances [45, 46].
The spin-flip resonance is shown to be having great contributions to the total M1 strength [31]. Unlike the scissors resonance which appears around 2 to 4 MeV of excitation energy, the centroid of the spin-flip resonance vary over several excitation energies, meaning it does not have a specific range of energies where it is usually found, the centroid of spin flip resonances can be found in different energy regions [31, 47]. The spin-flip resonances

are shifted to higher energies by the residual particle-hole interaction [48] on the spin-isospin channel and it also helps in the fragmentation of the M1 strength [31]. The same interaction is less effective on the scissors resonance hence the scissors resonance does not get shifted to higher energies [46].
The spin-flip strength is localized at the spin-orbit gap energy in closed shells for perfectly spherical nuclei [49,50]. For well deformed nuclei, the spin-flip strength is broaden around the spherical energy centroid because of the splitting of the Nilsson energy levels. The excitation energy centroid of the spin-flip resonance is given as follows [50]:

$$E_x \simeq 41A^{-1/3} \text{ MeV}. \tag{2.32}$$

Isovector and isoscalar modes can be identified independently at the case of an increase in spin-flip strength, with usually the isovector part being at higher energies than the isoscalar part [49,51].

2.4.4 Low Energy Enhancement (LEE)

One recently discovered resonance is the M1 low-energy enhancement. The LEE is suggested to be as a result of E1 transitions because of single-quasiparticle excitation in the continuum [52]. Another theory suggests more stronger M1 transitions at low energies as a result of re-coupling of high-j orbitals for protons and neutron [53,54]. The LEE was discovered in 2004, the resonance was observed (see Fig.2.10) at γ-ray energies which are $\leq$ 3 MeV [55]. The LEE was observed in many studies after that such as in ^{95}Mo [56], ^{43,45}Sc [57,58],^{44,46}Ti [57,59,60] and ^{50,51}V [61].

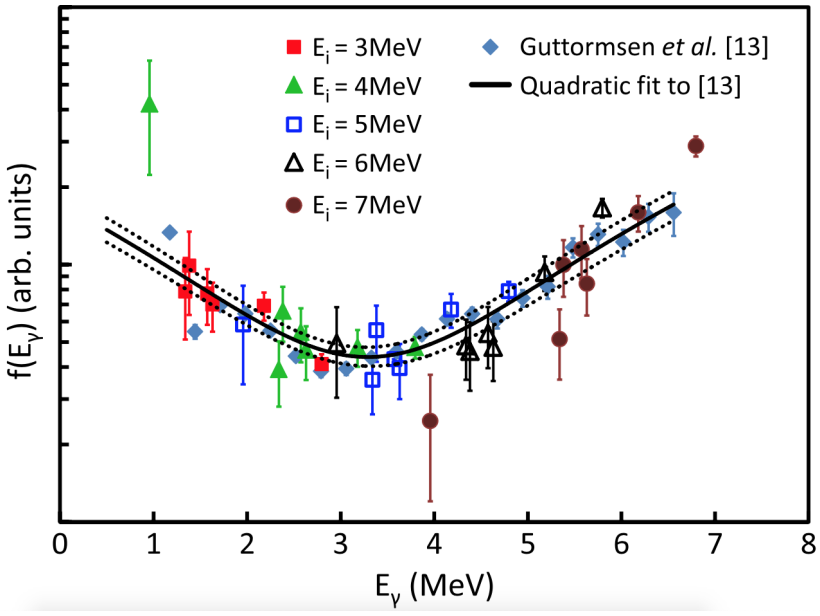


Figure 2.10: An example of the LEE from the work of Wiedeking et al [56] where the LEE was extracted using the X method in comparison with the work of Guttormsen et al [62] where the LEE was extracted using the Y method. Picture taken from [56]

Calculations have been performed since the LEE was discovered to work out the origin of the resonance, some calculations were made to account for an up-bend of the M1 character [63]. Firstly the up bend was only observed in light and medium mass nuclei as research around this area gained momentum the up bend was also observed in nuclei

such as ^{138}La [64] and ^{70}Ni [65]. "A low-energy enhancement in the γSF up to a factor of 30 over common theoretical E1 models is confirmed" [66]. The LEE has been confirmed theoretically and experimentally.

2.4.5 Giant dipole resonance

The Giant dipole resonance (GDR) was first reported to be an excitation mode in which a motion of nucleons in the nucleus, where the protons move in one direction and the neutrons move in the opposite direction [67] as shown in Fig 2.11. The recent article of the GDR by Firestone [68] states "The Giant Dipole Resonance (GDR) is shown to result from an increase in level density at a harmonic oscillator gap excitation energy of $2\hbar\omega$". That is the GDR is affected by an increase in both the NLD and γSF.

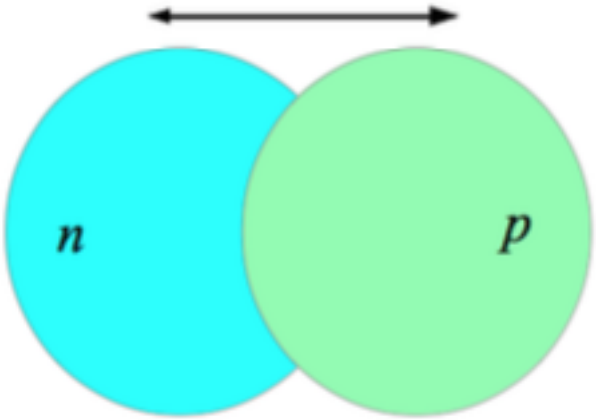


Figure 2.11: The movement of neutrons and protons in the giant electric dipole resonance [30].

The GDR is governed by the following quantum numbers: the spin S, isospin T, angular momentum J and multipole order L. $S = 0$ implies that the resonance is electric and $S = 1$ implies that the resonance is magnetic. $T = 0$ means the isospin is an isoscalar and $T = 1$ means an isovector isospin. $L = 0$ refers to monopoles, $L = 1$ to dipoles, $L = 2$ to quadrupoles and so on.

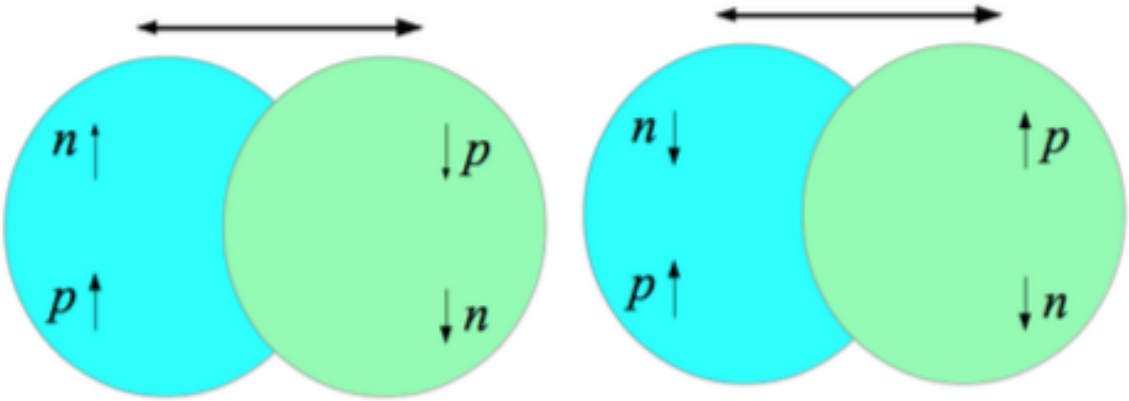


Figure 2.12: An illustration of the motion of protons and neutrons in isoscalar (left) and isovector (right) [30].

In a many-body quantum system, the GDR is an excitation of atomic nuclei that occurs at a high frequency, as an oscillation of all the protons against the neutrons in the nucleus in a macroscopic view. In terms of isocalar resonances the protons and neutrons oscillate in phase and in terms of isovector the protons and neutrons oscillate out of phase as illustrated in Fig. 2.12.
Photo-absorption cross section extracted from most deformed nuclei clearly shows a pronounced asymmetry instead of a distinct double-hump structure as it is expected of K-splitting [69]. Such a behavior is believed to be related to how close these nuclei are from the critical point of the phase shape from vibrators to rotors with a soft quadrupole deformation potential [69]. The isovector GDR (IVGDR) was observed to generally increase as deformation increases.

2.4.6 Pygmy dipole resonance

The pygmy dipole resonance can be described at a macroscopic level as a neutron skin oscillating against an isospin neutron and proton core as shown in Fig 2.13. A microscopic definition explains the resonance as result of single-particle E1 transitions near the neutron separation energy. In the work of Bartholomew *et al.* [24] the results obtained showed a systematic high intensity of γ-rays between 5 and 7 MeV for a number of nuclei measured from (n, γ) and (d,p)-reactions [24]. This structure is associated with excess of neutrons in nuclei.

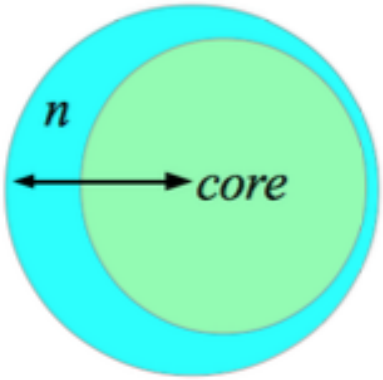


Figure 2.13: A representation of the neutron skin oscillating against an isospin neutron and proton systematic core [30].

2.5 Lorentzian functions

The resonances known thus far can be described using the Lorentzian models and functions. When the giant dipole resonance was first described using the standard Lorentzian (SLO) a width (Γ_0^2) that is temperature and energy independent was used as follows [70]:

$$f_{E1}^{SLO} = 8.68 \times 10^{-8} \frac{\sigma_0 E_\gamma \Gamma_0^2}{(E_\gamma^2 - E_0^2)^2 + E_\gamma^2 \Gamma_0^2} \ \text{MeV}^{-3}. \tag{2.33}$$

Here σ_0 is the peak cross-section (in mb), Γ_0^2 is the width of the giant electric dipole resonance (in MeV) and E_0^2 is the peak centroid (in MeV). Results show that this model

was exaggerating the strength of the resonance at neutron separation energy (S_n) and below. So the model was then confirmed with an energy dependant width $\Gamma(E_\gamma)$ as follows [70]:

$$f_{E1}^{SLO} = 8.68 \times 10^{-8} \frac{\sigma_0 E_\gamma \Gamma_0 \Gamma(E_\gamma)}{(E_\gamma^2 - E_0^2)^2 + E_\gamma^2 \Gamma_0^2} \text{ MeV}^{-3}, \tag{2.34}$$

where $\Gamma(E_\gamma)$ is the energy dependent width. This width can be modified to also include temperature dependence and is given as follows [70].

$$\Gamma(E_\gamma, T) = \Gamma_0 \frac{E_\gamma^2 + 4\pi^2 T^2}{E_0^2}, \tag{2.35}$$

where T is the temperature given as

$$T = \sqrt{\frac{S_n - E_\gamma}{a}}, \tag{2.36}$$

S_n is the neutron separation energy and a is the back shifted Fermi gas level density parameter. This model was also not completely correct because it could not account for the electric operator in the zero limit E_γ. The standard Lorentzian function was then developed to a generalised Lorentzian function given as follows [71]:

$$f_{E1}^{GLO} = 8.68 \times 10^{-8} \sigma_0 \Gamma_0 \left[\frac{E_\gamma \Gamma(E_\gamma, T)}{(E_\gamma^2 - E_0^2)^2 + E_\gamma^2 \Gamma_0^2} + 0.7 \frac{\Gamma(E_\gamma = 0, T)}{E_0^3} \right] \text{ MeV}^{-3}. \tag{2.37}$$

This model works for the mass regions A $\approx$ 55 to 150 and A $\approx$ 175 to 197. At mass region A $\approx$ 150 to 175 the model underestimates $f(E_\gamma)$ for well deformed nuclei. So the following width was adapted for the underestimated mass regions [71]

$$\Gamma(E_\gamma, T) = k_0 + (1 - k_0) \left(\frac{E_\gamma - \epsilon_0}{E_0 - \epsilon_0} \right) \frac{\Gamma(E_\gamma^2 + 4\pi^2 T^2)}{E_0^2}, \tag{2.38}$$

where k_0 is an empirical expression that depends on the mass of the nucleus and the constant ϵ_0 is a set to be 4.5 MeV [72]. When substituting this width in the above equation, the resulting equation is called the enhanced generalised Lorentzian model. The standard Lorentzian usually holds for M1 resonances, even so, any of the above models can be used depending on the mass of the nucleus of interest.

Chapter 3

The Oslo Method

For approximately 28 years now the Oslo method has been introduced and continuously developed for its purpose. This method is a collection of techniques which can simultaneously extract the nuclear level density and γSF. The analytical technique takes the particle-gamma coincidence matrix as an input and follows a step-by-step procedure to extract the statistical properties. The steps are as follows

1. Unfolding of the γ-ray spectra.
2. Extracting the first generation matrix or first generation events.
3. Simultaneously extracting the γSF and NLD.
4. Normalization of the γSF and NLD obtained.

In this chapter each of these steps will be briefly discussed, for detailed explanations see Ref [12, 13].

3.1 Unfolding of the γ-ray spectra

A detector response function takes the energy-dependent flux of incoming source photons that are incident on a detector and converts them into a detector response spectrum corresponding to the one observed in experimental detector measurements [73]. This function is unique for each detector type and setup. In this case the γ spectra of a particle-γ coincidence matrix has to be corrected for the response of the Sodium Iodide (NaI(Tl)) scintillation detector. The response function is determined by the different interactions when a photon hits the detector, it interacts with the detector in different ways [74]. In this section the main three interactions will be discussed which are Compton scattering, pair production and photoelectric absorption.
Compton scattering was first explained by Arthur Holly Compton [75]. This is the inelastic scattering of a photon to a different or new direction with less energy than the incident one, the scattering happens after the photon transfers energy to an electron as illustrated by Fig.3.1. This minimises the chances of the photon to release all its energy into the detector material, this type of interaction is dominant for $E_\gamma \approx 400$ keV to about 10 MeV.
Pair production occurs when a photon interacts with matter and leads to the creation of an electron-positron pair near the nucleus. Energy has to be conserved for pair production

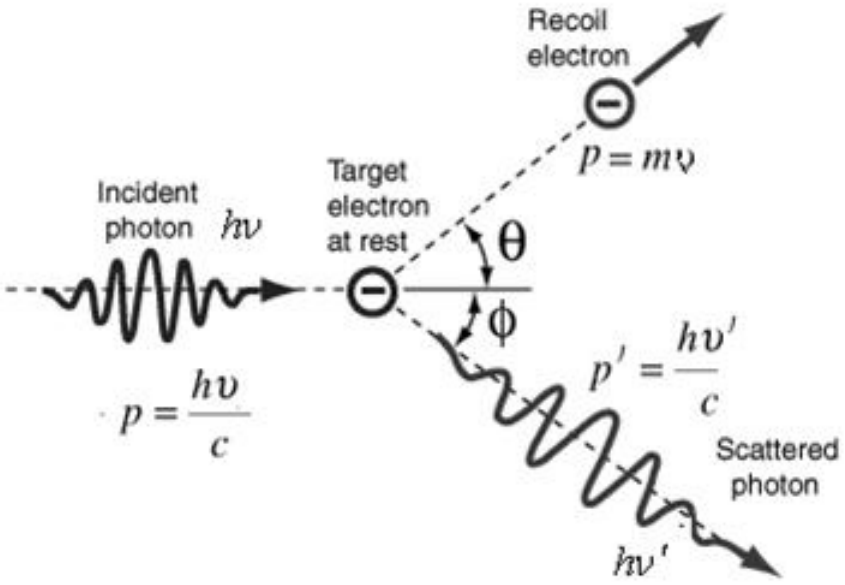


Figure 3.1: A schematic representation of the Compton scattering process where θ is the angle of the recoil electron and ϕ is the angle of the the scattered photon [75].

to occur. The incoming photon's energy should be above a threshold of the total rest-mass energy of both the particle and its antiparticle. Pair production is found in photons with E_γ greater than 1,022 MeV. The electron-positron pair can collide and annihilate to two equal photons of 511 keV energy each see Fig. 3.2.

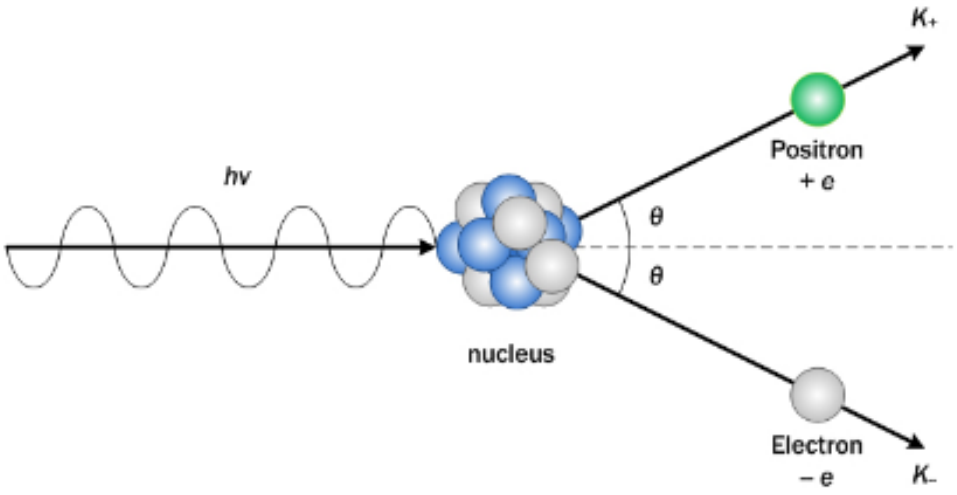


Figure 3.2: The process of pair production, clearly showing how the scattering angle (θ) of the positron and the electron are equal [76].

The energy of the electron involved in the **photo electric effect** called a photo-electron is given by $E_e = E_\gamma - E_{BE}$ where E_{BE} is the electron binding energy and E_γ is the γ-ray energy. At low E_γ the photo electric effect is the most dominant mode of photon interaction with matter E_e. This occurs when the photon interacts with matter and transfers all of its energy to the electron as illustrated in Fig. 3.3. The electron is

discharged from the atom. The outcomes are then recorded by the detector as all the incident energy of the photon and will appear in the full energy peak. Only the full γ-ray energy deposited events are taken into account in this study the rest are removed.

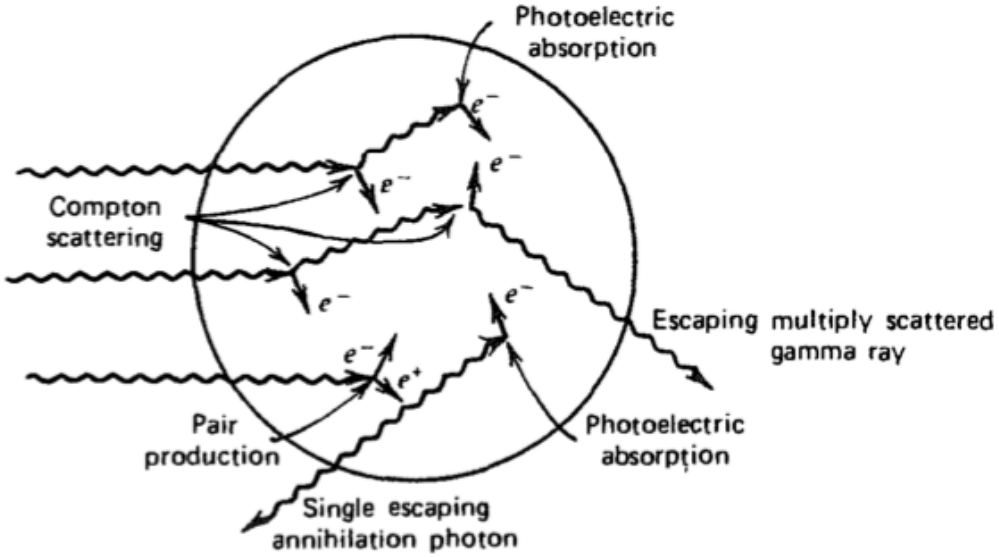


Figure 3.3: An illustrative picture of the energy deposited by the three interaction modes explained above, how photons interact with the detector material, resulting in full or partial γ-ray energy deposition [77].

3.2 The folding iterative procedure

The response function of the detectors can be given by R_{ij}, which indicates the response in channel i when the incident γ-ray has energy corresponding to channel j. Folding can be represented as follows [78]:

$$Ru = f, \tag{3.1}$$

where f is the folded matrix, u is the unfolded matrix and R is the response matrix. The following steps are to show how the folding iterative method is carried out [78].

- The observed or trial function for the unfolded γ-ray spectrum is defined as $u_0 = r$.
- Then $f_0 = Ru_0$ is used to calculate the first folded spectrum.
- To find the next trial function $r - f_0$ is added to the previous trial function u_0 so $u_1 = u_0 + (r - f_0)$.
- The second folded spectrum is calculated as $f_1 = Ru_1$. To find the next trial function $r - f_1$ is added to the previous trial function u_1 so $u_2 = u_1 + (r - f_1)$.

Continue finding $u_1, f_1, u_2, f_2, u_3, f_3 ... u_n, f_n$ where f_n is approximately equal to r, just like in Fig. 3.4 where f_n is equal to Ru^{10}, usually the number of iterations is 10 to 30. For this study 11 iterations were performed, this is because f_n was reached at the 11^{th}

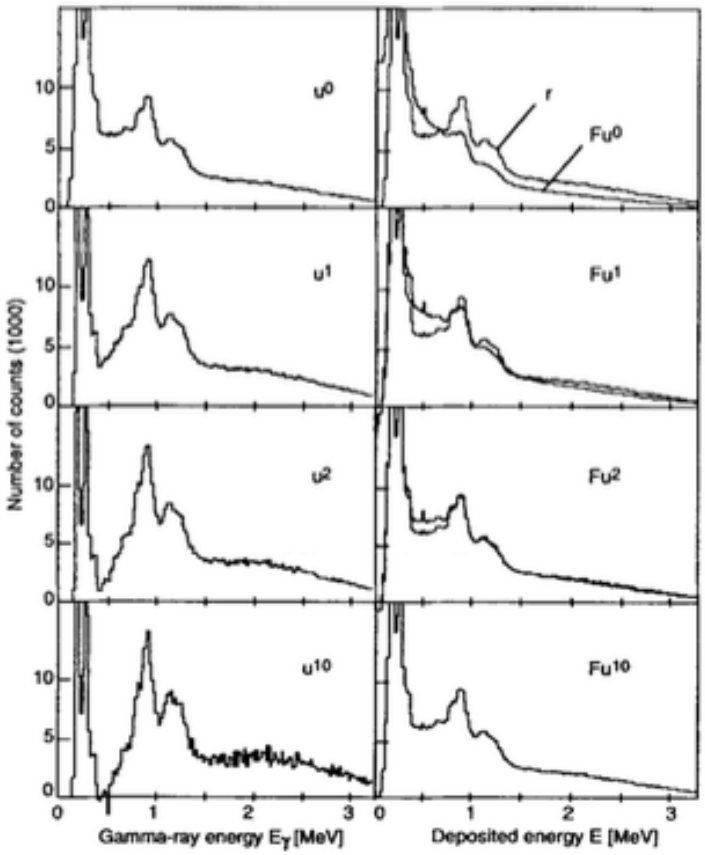


Figure 3.4: The diagram shows how continuously repeating the folding iterative procedure affects the spectrum, F_u is the same as R_u defined above [78].

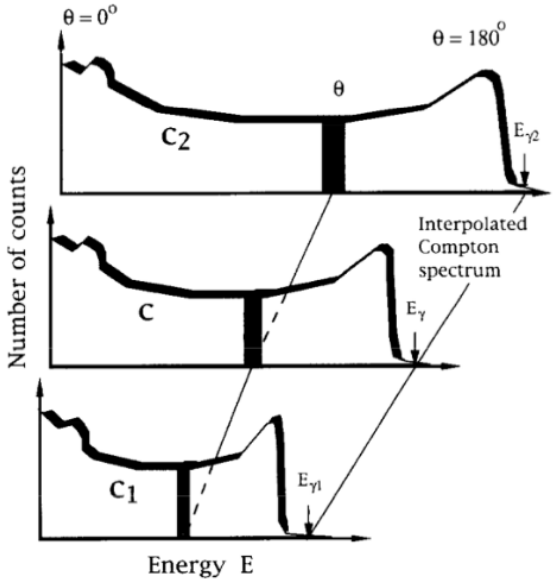


Figure 3.5: Schematic representation of the interpolation of the Compton part from the measured response functions c1 and c2 [78]. θ is scattering angle and it increases with the increase in the energy transferred to the electron.

iteration. The Compton subtraction method is then used to obtain a lesser fluctuating unfolded γ-ray spectrum [78].
Ru is the folded spectrum, r is the observed spectrum and u is the unfolded spectrum.

3.3 Compton Subtraction

The fluctuations found in the spectrum that result from the folding iteration process, can be smoothed out using the Compton subtraction method. This is a method that was developed from the understanding of Compton scattering [78]. This method takes the unfolded γ-ray spectrum let's name it u^0 as its starting point. From this spectrum u^0 we want to produce a spectrum that differentiates between the contributions resulting from photo electric effect (full energy peak), pair production (single and double escape peaks or annihilation peak) and Compton scattering.
This can be done with the help of the following equation from the response function construction:

$$p_{full} + p_{single} + p_{double} + p_{annihilation} + p_{Compton} = 1. \tag{3.2}$$

All contributions, single escape peak u_s, double escape peak u_d and annihilation peak u_a, except Compton contributions are given as

$$v(i) = u_f + u_s + u_d + u_a. \tag{3.3}$$

When both the above equations are combined with u^0 then the product is a spectrum that only consists of Compton contributions, which is a consequence of subtracting all the other contributions from the raw spectrum see Fig.3.5. The Compton spectrum $c(i)$ in channel i is given as:

$$c(i) = r(i) - v(i), \tag{3.4}$$

where $r(i)$ is the raw spectrum and $v(i)$ is defined as follows,

$$v(i) = p_f(i)u^0(i) + w(i), \tag{3.5}$$

and

$$w(i) = p_s(i)u_0(i) + p_d(i)u_0(i) + \Sigma p_a(i)u_d(i). \tag{3.6}$$

p_s, p_d, p_f and p_a are the probabilities of the single escape peak, double escape peak, full energy peak and annihilation peak, respectively, and are obtained from Ref. [78].
A Gaussian peak is properly placed in channels that have corresponding resolution to the experiment. This is done to avoid only having delta functions at $i = i_f - 511\ keV$, $i = i_f - 1022\ keV$ and $i = 511\ keV$. Here the resolution is 1.0 FWHM for the annihilation peak. FWHM is the full width half maximum of the respective peaks. The response matrix and raw matrix have resolutions of 0.1 FWHM and 1.0 FWHM respectively for the other peaks.This result to the resolution being $\sqrt{1.0^2 - 0.1^2} = 0.99$ FWHM.
Now the more accurate representation of the unfolded spectrum will be given as:

$$u(i) = \frac{r(i) - c(i) - w(i)}{p_f(i)}. \tag{3.7}$$

When we take into account the γ-ray detection efficiency, the true γ-ray energy spectrum U(i) produced and represented as follows [78]:

$$U(i) = \frac{u(i)}{\epsilon_{tot}(i)}, \tag{3.8}$$

where $\epsilon_{tot}(i)$ is the γ-ray total detection efficiency which can be taken from but not limited to Ref [78]. Fig 3.6 shows how the spectrum looks throughout and after the Compton subtraction process.

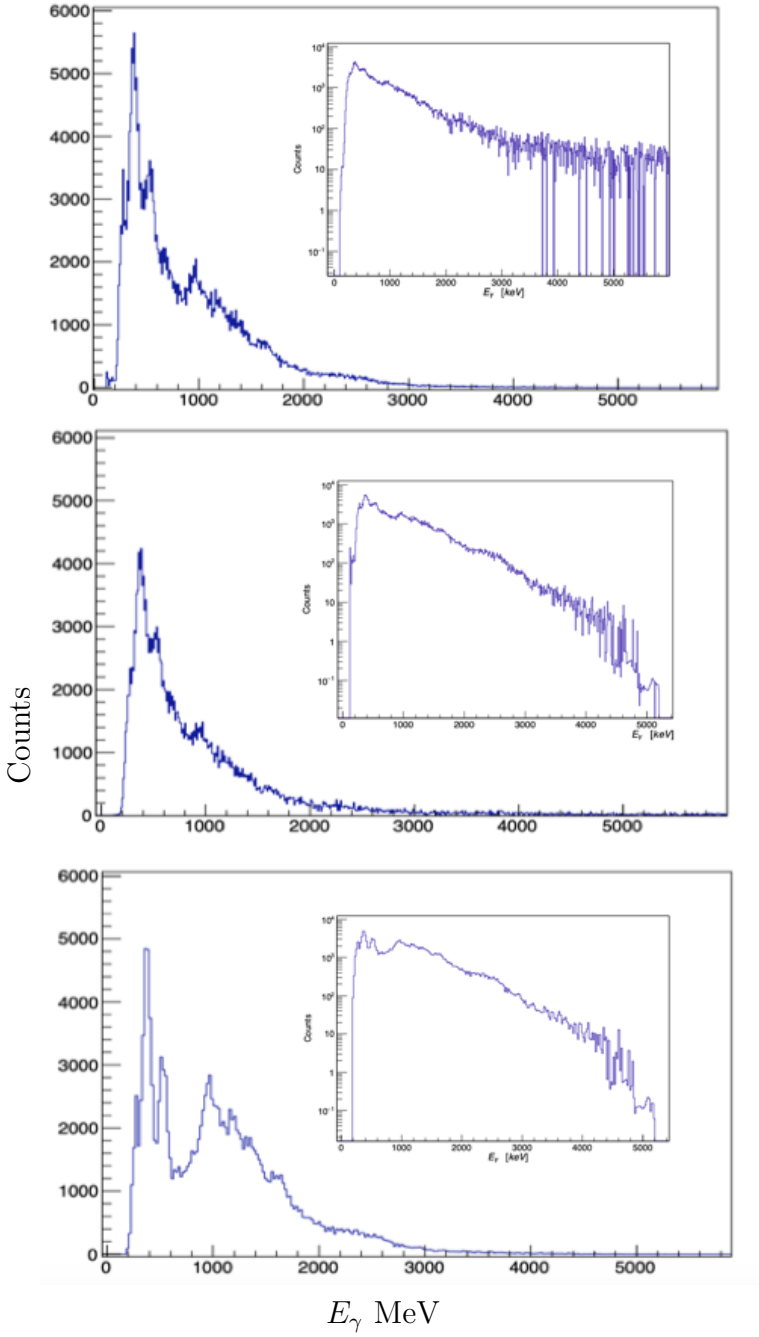


Figure 3.6: The γ-ray spectrum through and after the Compton subtraction process raw matrix (top), Unfolded (middle) and the Primary γ-ray matrix (bottom).

3.4 The first generation γ-ray spectrum

The unfolded matrix remains only with full energy peaks after Compton subtraction. These full energy peaks belong to the γ-rays detected at all the available excitation energies, from the decay cascades. A decay cascade, also known as a "decay chain", is a series of radioactive decays of different radioactive products as a step by step series of transformations. The data needed to calculate the statistical properties which are the NLD and γSF, is contained in the distribution of the primary or first generation γ-rays. Excited states will decay primarily through a cascade of γ-rays. The primary γ-rays are obtained through a method called the "first generation method". It is assumed in this method that there is no difference between the properties of a state when it is populated through a γ-decay and when it is populated directly from a nuclear reaction, in the quasi-continuum before γ-emission [79]. A γ-ray spectrum h_i is extracted from the unfolded spectrum (full peaks), starting from the highest excitation energy region of the unfolded spectrum f_i at the highest excitation energy region is given as follows [80]:

$$h_i = f_i - g_i. \tag{3.9}$$

Here g_i is the weighting sum of all the γ-ray spectra, which is represented as $g_i = \sum_j n_{ij} w_{ij} f_j$ for all $i < j$. The parameter w_{ij} represents the probability of the decay of states from bin i to those in bin j, and the sum $\sum_j w_{ij} = 1$. In other words, w_{ij} can be taken as the branching ratio for primary γ-rays depopulating level i. The populating cross section is different for every level i and j, n_{ij} is the correcting factor that accounts for this. The calculations are such that the area of f_{ij} when multiplied by the correcting factor n_{ij} will have the same number of cascades [13]. The population cross section of different excitation energy bins has to be taken into account. The n_{ij} factor can be calculated in two ways, the singles normalization and multiplicity normalization.

Singles normalization: Particle detection that is caused by singles spectra can be used to obtain the ratios of populations of various excitation energy bins. The n_{ij} normalization factor for every excitation energy bin $j < i$ can be calculated as follows:

$$n_{ij} = \frac{S_i}{S_j}.$$

Here S_i and S_j are the singles particle cross sections for bins i and j, respectively [80].

Multiplicity normalization: Finding the average γ-ray multiplicity (M) is required in this technique. To find the average γ-ray multiplicity, let's assume an N-fold population of an excited level and call it E_x, then this energy bin will output N number of γ cascades. Since the results of decay from this level will be N γ-ray cascades, here the i^{th} cascade consists of M_i γ-rays. The total energy of the γ-rays emitted will be equal to the average γ-ray energy $< E_\gamma >$ [79]

$$< E_\gamma >= \frac{N E_x}{\Sigma_{i=1}^{N} M_i} = \frac{E_x}{\frac{1}{N}\Sigma_{i=1}^{N} M_i} = \frac{E_x}{< M >}. \tag{3.10}$$

The average multiplicity is given as:

$$< M >= \frac{E_x}{< E_\gamma >}, \tag{3.11}$$

where E_x is the excitation energy at bin i. The average multiplicity $< M_i >$ can be calculated for E_x. The area in spectrum f_i can be given by $A(f_i)$. The singles particle

cross sections for bin i S_i is proportional to $A(f_i) < M_i >$. There for n_{ij} applied to n_i when subtracting bin j is given as follows [80]:

$$n_{ij} = \frac{A(f_i)/ < M_i >}{A(f_j)/ < M_j >} = \frac{< M_j > A(f_i)}{< M_i > A(f_j)}. \tag{3.12}$$

In a case where multiplicity is regarded to be well defined, an area consistency check can be used on $h_i = f_i - g_i$ above. Introducing a correction by letting $g = \alpha g$, here α is very small close to 1. Then the area of the first generation γ spectrum is represented as follows [80]:

$$A(h_i) = A(f_i) - \alpha A(g). \tag{3.13}$$

This matches the γ-ray multiplicity of one unit and it can also be given as:

$$A(h_i) = A(f_i)/ < M_i > . \tag{3.14}$$

Combining equations 3.13 and 3.14 or equating these equations and solve for α we get

$$\alpha = \frac{\big(1 - \frac{1}{< M_i >}\big) A(f_i)}{A_{(g)}}. \tag{3.15}$$

The above correction is always useful in case an improper weighting function w_{ij} is used [80]. The weighting coefficient w_{ij} is the same or directly composed of h_i, so they can be determined through a fast converging iterative technique [80], that consist of the steps below:

- Apply a trial function w_{ij}.
- Compute h_i using $h_i = f_i - g_i$.
- Set h_i to have the same energy calibration as w_{ij}, no normalize the area of h_i to 1.
- If w_{ij} is approximately equal to the initial w_{ij} then the procedure has converged. If not, repeat from the second step until w_{ij} (new) is approximately equal w_{ij} (old).

In Fig.3.7 by subtracting the γ -ray spectra from excitation states E1 and E2, the primary γ-rays from excitation energy state E3 are obtained, g.s. represents ground state.

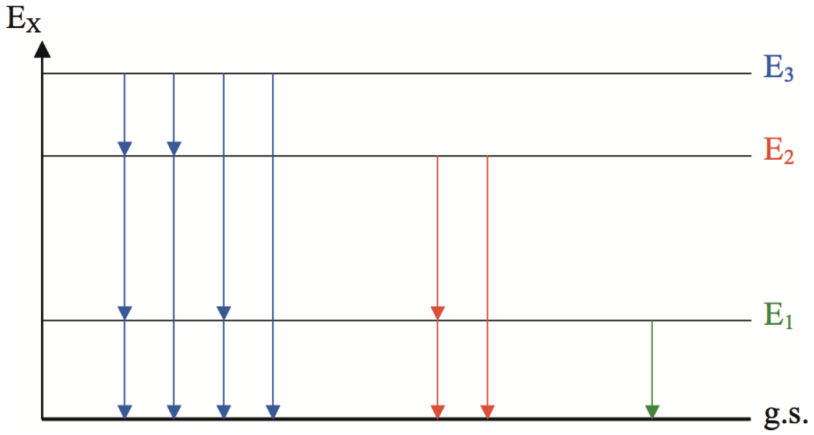


Figure 3.7: A schematic representation of a decay cascade between excitation energies. The arrows shows γ -rays decaying from one excited state to another [72].

3.5 Extracting the nuclear level density (NLD) and the gamma strength function γSF

A proven and valid assumption for compound reactions states that the relative probability of decay into a set of final states does not depend on the way the compound nucleus was formed, implying that the compound nucleus can lose track of the way of formation based on the sharing of its kinetic energy with a large number of nucleons [25]. Therefore following the decay of the compound will mainly depend on statistical rules. The decay probability $P(E_x, E_\gamma)$ of a γ-ray with energy E_γ which decays from a certain excitation E_x is proportional to the level density $\rho(E_f)$ and the transmission coefficient $T(E_\gamma)$. E_f is the final excitation energy and is given by $E_f = E_x - E_\gamma$ [81, 82].
So we have

$$P(E_x, E_\gamma) \propto \rho(E_f)T(E_\gamma). \tag{3.16}$$

Equation 3.16 can be compared with Fermi's golden rule of decay rates given as follows [12]:

$$\lambda_{if} = \frac{2\pi}{\hbar}| < f|\hat{H}_{int}|i > |^2\rho(E_f). \tag{3.17}$$

where λ_{if} is the rate at which the original state i decays to the final state f. $\hat{H}_{int}$ is the transmission operator and $\rho(E_f)$ is the level density at the final energy. The generalized Brink-Axel hypothesis [83, 84] states that the strength function does not depend on the structure of the initial or final states. Implying that the transmission coefficient depends only on the γ-ray energy E_γ [83]. The extraction method on Fermi's golden rule depends on the initial and final states, while the Brink-Axel hypothesis depends only on the γ-ray energy (E_γ).
In case of a properly normalised first generation matrix, the total probability for decay is equal to 1 [12] given by:

$$P(E_f, E_\gamma) = 1, \tag{3.18}$$

and can be represented as follows:

$$\sum_{E_\gamma = E_\gamma^{min}}^{E_x} P(E_x, E_\gamma) = 1.$$

Leading to a theoretical approximation of the first generation γ-ray matrix, represented as

$$P_{th}(E_x, E_\gamma) = \frac{T(E_\gamma)\rho(E_x - E_\gamma)}{\Sigma_{E_\gamma = E_\gamma^{min}}^{E_x} T(E_\gamma)\rho(E_x - E_\gamma)}. \tag{3.19}$$

The theoretical matrix $P_{th}(E_x, E_\gamma)$ validates the assumption set by the experimental input matrix $P(E_x, E_\gamma)$. We can estimate the first order T^0 without variables by letting the $\rho^{(0)} = 1$ [12] resulting to:

$$T^{(0)}(E_\gamma) = \sum_{E_x = max(E_i^{min}, E_\gamma)}^{E_i^{max}} P(E_x, E_\gamma). \tag{3.20}$$

A χ^2 method is used to find the highest estimated orders of ρ and T. This is done by fitting $P(E_x, E_\gamma)$ which is deduced from experimental to theoretical $P_{th}(E_x, E_\gamma)$. Mathematically it is given as:

$$\chi^2 = \frac{1}{N_{free}} \sum_{E_x=E_i^{min}}^{E_i^{max}} \sum_{E_\gamma=E_\gamma^{min}}^{E_x} \left(\frac{P_{th}(E_x, E_\gamma) - P(E_x, E_\gamma)}{\Delta P(E_x, E_\gamma)} \right)^2. \tag{3.21}$$

Here N_{free} are of the degrees of freedom, $\Delta P(E_x, E_\gamma)$ is the uncertainty of the first generation matrix and E_γ^{min} is the minimum γ-ray energy. All possible solutions can be constructed by minimizing χ^2 and the infinite solutions are given as [12]:

$$\tilde{\rho}(E_x - E_\gamma) = \rho(E_x - E_\gamma) A \; exp \; [\alpha(E_x - E_\gamma)], \tag{3.22}$$

and

$$\tilde{T}(E_\gamma) = T(E_\gamma) B \; exp \; \big[(\alpha E_\gamma)\big]. \tag{3.23}$$

Here α is the transformation parameter of the slope of the NLD and γSF while A and B are normalization constants. A, B and α are the free parameters. There are an infinite number of solutions that can be computed using equations 3.22 and 3.23, therefore the actual solutions must be determined.
In case of limited data points the procedure might not converge properly, hence it might need to be enhanced and generalised. The procedure can be generalized by regulating the maximum change of data points in $\tilde{T}$ and $\tilde{\rho}$ inside a single iteration to a specific percentage N. To generalize the method it should be checked whether the interval of the new iteration is set on by the old iteration as follows [12]:

$$\frac{old}{1 + \frac{N}{100}} \leq new \leq \big(1 + \frac{N}{100}\big) \times old. \tag{3.24}$$

A simulation is used to calculate the possible errors that might have occurred on $\rho(E_f)$ and $T(E_f)$ during the processes of unfolding and extraction [12]. The simulation is done 100 times, in order to get reasonable statistics. The statistics are given by:

$$\Delta\rho(E_f) = \frac{1}{\sqrt{100}} \sqrt{\sum_{i=1}^{100} [\rho_i^{(s)}(E_f) - \rho(E_f)]^2}, \tag{3.25}$$

$$\Delta T(E_f) = \frac{1}{\sqrt{100}} \sqrt{\sum_{i=1}^{100} [T_i^{(s)}(E_f) - T(E_f)]^2}, \tag{3.26}$$

for NLD and γ transmission coefficient, respectively.

3.6 Normalization of the NLD and γSF

From the methods shown above we can realise that there are infinite solutions of $T(E_\gamma)$ and $\rho(E_f)$ see Fig. 3.9 and 3.8. To obtain the actual values the data must be normalised.

3.6.1 Normalization of the NLD

To determine the slope parameter α of the NLD and γ-ray transmission coefficient, also to determine the absolute value A of the NLD in Eq.3.22, the operation ρ is modified to suit the number of the well known discrete states at low excitation energy below 2 MeV, and the neutron resonance spacing data at high excitation energy [12]. This data at high excitation energies can be determined using the Back Shifted Fermi Gas Eq.2.2 as a starting point. The adopted level density formula at a given excitation energy E_x and angular momentum is [18]:

$$\rho(U,J) = \frac{\sqrt{\pi}}{12}\frac{exp(2\sqrt{aU})}{a^{1/4}U^{5/4}}\frac{(2J+1)exp[-(J+1/2)^2/2\sigma^2]}{2\sqrt{2\pi}\sigma^3}, \tag{3.27}$$

and

$$\rho(U) = \frac{\sqrt{\pi}}{12}\frac{exp(2\sqrt{aU})}{a^{1/4}U^{5/4}}\frac{1}{\sqrt{2\pi}\sigma'}, \tag{3.28}$$

where $\rho(U,J)$ and $\rho(U)$ are level densities for a given spin J and all spins, respectively σ is the spin cut off parameter, and a is the level density parameter [85]. I is the ground state spin of the target nucleus in (n, γ) reactions. The average s-wave neutron resonance spacing D_0 is represented as follows:

$$\frac{1}{D_0} = \frac{1}{2}[\rho(S_n, J = I + 1/2) + \rho(S_n, J = I - 1/2)]. \tag{3.29}$$

The assumption is that $+\frac{1}{2}$ and $-\frac{1}{2}$ parities have equal contributions to the level density at the neutron separation energy S_n. To find the level density at S_n combine equations 3.27 and 3.29, let $U = S_n$ therefore $\rho(S_n)$ is given as:

$$\rho(S_n) = \frac{2\sigma^2}{D_0}\frac{1}{(I+1)exp[-(I+1)^2/2\sigma^2] + exp[-I^2/2\sigma^2]}. \tag{3.30}$$

σ is calculated at S_n using the following equation:

$$\sigma^2 = 0.0146A^{5/3}\frac{1+\sqrt{1+4a(E-E_1)}}{2a}, \tag{3.31}$$

where the energy shift E_1 is treated as a free parameter. The free adjustable parameter E_1 for most nuclei is determined by fitting to experimental data.
An interpolation is made from where the data ends at high energies to the $\rho(S_n)$. This is because the experimental data ends before the excitation energy reaches S_n, the experiment not being maximised for the reaction studied can lead to less events hence the data ends before S_n. The interpolation is performed using the rigid moment of inertia (RMI) model [85].

3.6.2 Normalizing the γ-ray strength function

As the level density is normalised, the correct slope (α) of the γ-ray transmission coefficient is also determined, Figs. 3.8 and 3.9 shows examples of a well normalised NLD and γ-ray transmission coefficient, respectively. The constant parameter B is computed from the experimental average total radiative width $< \Gamma_\gamma(S_n, I_T \pm \frac{1}{2}, \pi_T) >$ where I_T is

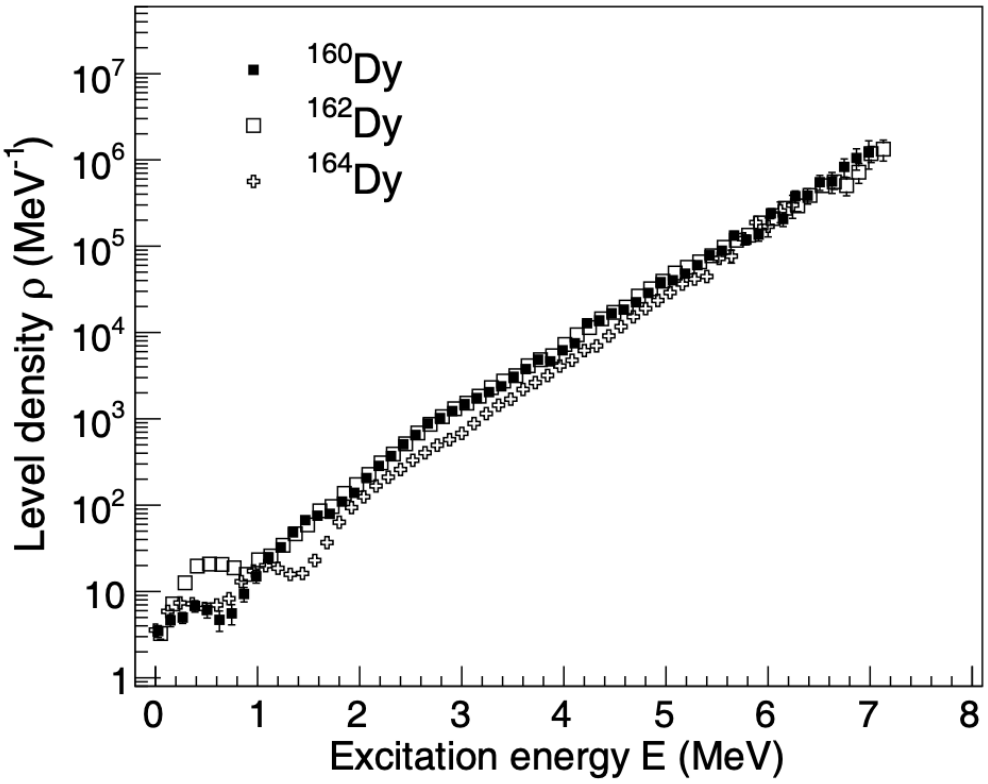


Figure 3.8: An example of normalised NLD of neighbouring Dy isotopes, exhibiting little mass dependence at high energies [4].

the spin and π_T is the parity of the target nucleus in (n,γ) reactions at constant temperature [13, 70].
The parameter $< \Gamma_\gamma >$ is determined as follows [70]:

$$< \Gamma_\gamma(S_n, I_T \pm \frac{1}{2}, \pi_T) >= \frac{D_0}{4\pi} \int_0^{S_n} dE_\gamma T(E_\gamma) \rho(S_n - E_\gamma) \cdot \sum_{I=-1}^{1} g(S_n - E_\gamma, I_T \pm \frac{1}{2} + I), \quad (3.32)$$

where g is the spin distribution and is given as [18]:

$$g(E, I) \simeq \frac{2I+1}{2\sigma^2} exp[-(I + \frac{1}{2})^2 / 2\sigma^2]. \quad (3.33)$$

Where $\rho(S_n - E_\gamma)$ is the experimental level density. The spin distribution is normalized so that g is equal to 1 [10]. Assuming that the main contribution to the statistical decay is dominated by dipole radiation (L = 1) therefore

$$BT(E_\gamma) = B(T_{E1}(E_\gamma) + T_{M1}(E_\gamma)). \quad (3.34)$$

The correlation between the γ-ray transmission coefficient and the γSF is represented as [86]:

$$T(E_\gamma) = 2\pi \sum_{XL} E_\gamma^{2l+1} f_{XL}(E_\gamma), \quad (3.35)$$

where X is the electromagnetic character and L is the multipolarity of the γ ray. The γSF can be calculated as follows [86]:

$$f(E_\gamma) = \frac{1}{2\pi E_\gamma^3} BT(E_\gamma). \tag{3.36}$$

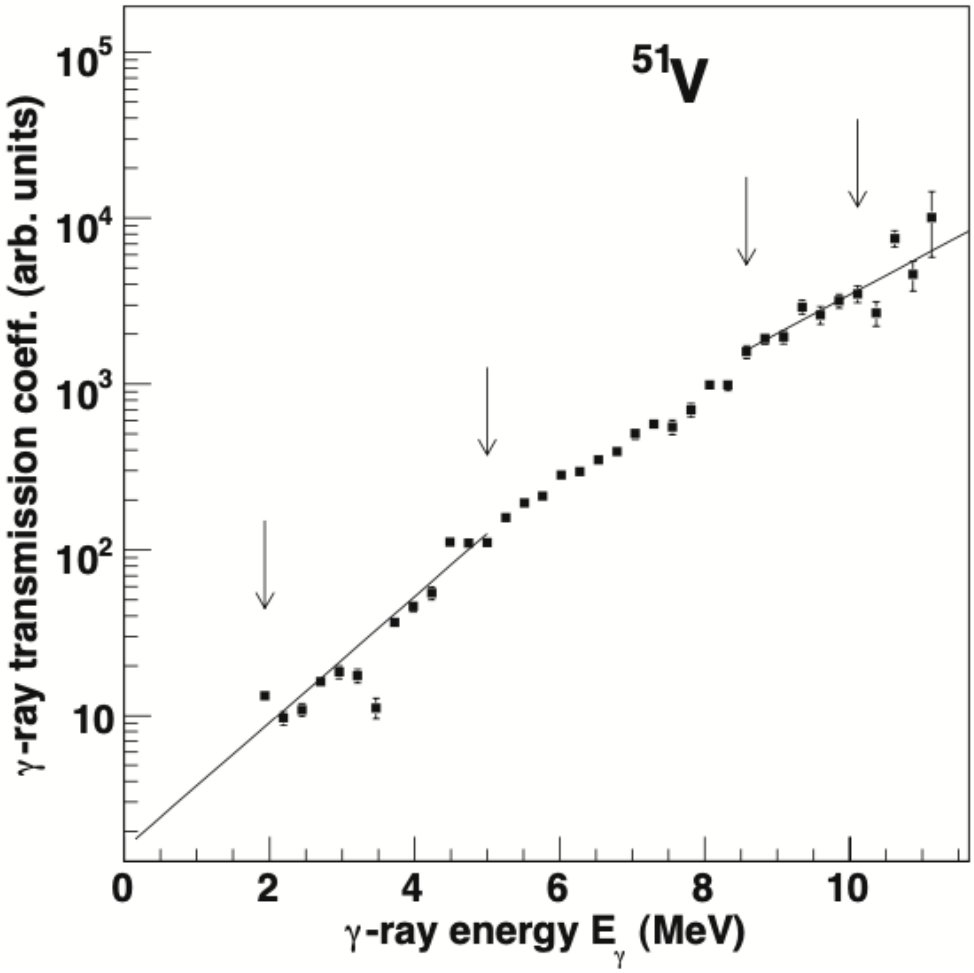


Figure 3.9: Diagram showing the γ-ray transmission coefficient of ^{51}V, The data points between the arrows are used to fit the exponential function to the experimental data [72].

3.7 The possible uncertainties of the Oslo method

In this section the precision and shortcomings of the analysis technique observed in this study and other related studies will be discussed.

3.7.1 Spin and Parity distribution

When normalizing the γ-ray transmission coefficient and the nuclear level density it is usually assumed for the number of levels with positive and negative parity to be equal.

This assumption holds for heavier nuclei but may not be completely true for lighter nuclei [13]. Mathematically this assumption can be described as follows:

$$\alpha = \frac{\rho_+ - \rho_-}{\rho_+ + \rho_-}, \tag{3.37}$$

where α is the parity asymmetry, ρ_+ is the level density with positive parity levels and ρ_- is the level density with negative parity levels. If α = -1 we have negative parity and if $\alpha = +1$ the parity is positive, both parities are equally represented if $\alpha = 0$ [87].

If the parity asymmetry is big it will change the value of the level density at neutron separation energy. A change in the value of the level density at the neutron separation energy $\rho(S_n)$ leads to a change in the slope of the NLD and the γ-ray transmission coefficient hence also in the slope of the γSF [13]. For $A > 80$ nuclei the parity asymmetry does affect the $\rho(S_n)$ and the γSF [13]. For $A < 56$ nuclei the parity asymmetry is less hence the minimal to no change in $\rho(S_n)$. The absolute normalization of the γSF and the NLD error lies in the range of 30% and 50% [13].

Some ways in which uncertainty in the spin distribution can cause errors to the analysis technique are as follows: The way in which the first-generation γ rays are extracted can have a huge effect on the resulting NLD and γSF. How correctly the $\rho(S_n)$ is estimated, also determines how much error has to be accounted for by the method. The third way in which spin distribution uncertainty can lead to errors in the method is how the spin range is accessed experimentally compared to the actual total spin distribution [13].

We notice that spin distribution is one of the biggest uncertainty contributors in the reaction so it must be calculated and accounted for correctly. The slope of the NLD and γSF is determined using the intensity of the populated spin at S_n. The enhancement of the γSF at low γ-ray energies of light nuclei is caused by higher spin on the initial levels [13].

In the investigation to test how spin distribution contributes to uncertainties by Larsen *et al.* in their outstanding work the following spin ranges were used: $\frac{1}{2} \leq \mathrm{J} \leq \frac{7}{2}$, $\frac{1}{2} \leq \mathrm{J} \leq \frac{13}{2}$ and $\frac{7}{2} \leq \mathrm{J} \leq \frac{13}{2}$ see Fig. 3.10. Implying that the highest possible spin reached will be $\frac{9}{2}$ or $\frac{15}{2}$ based on the maximum initial spin allowed. The results showed that the NLD remained fairly unchanged while the γSF had increased strength at low γ-ray energies [13].

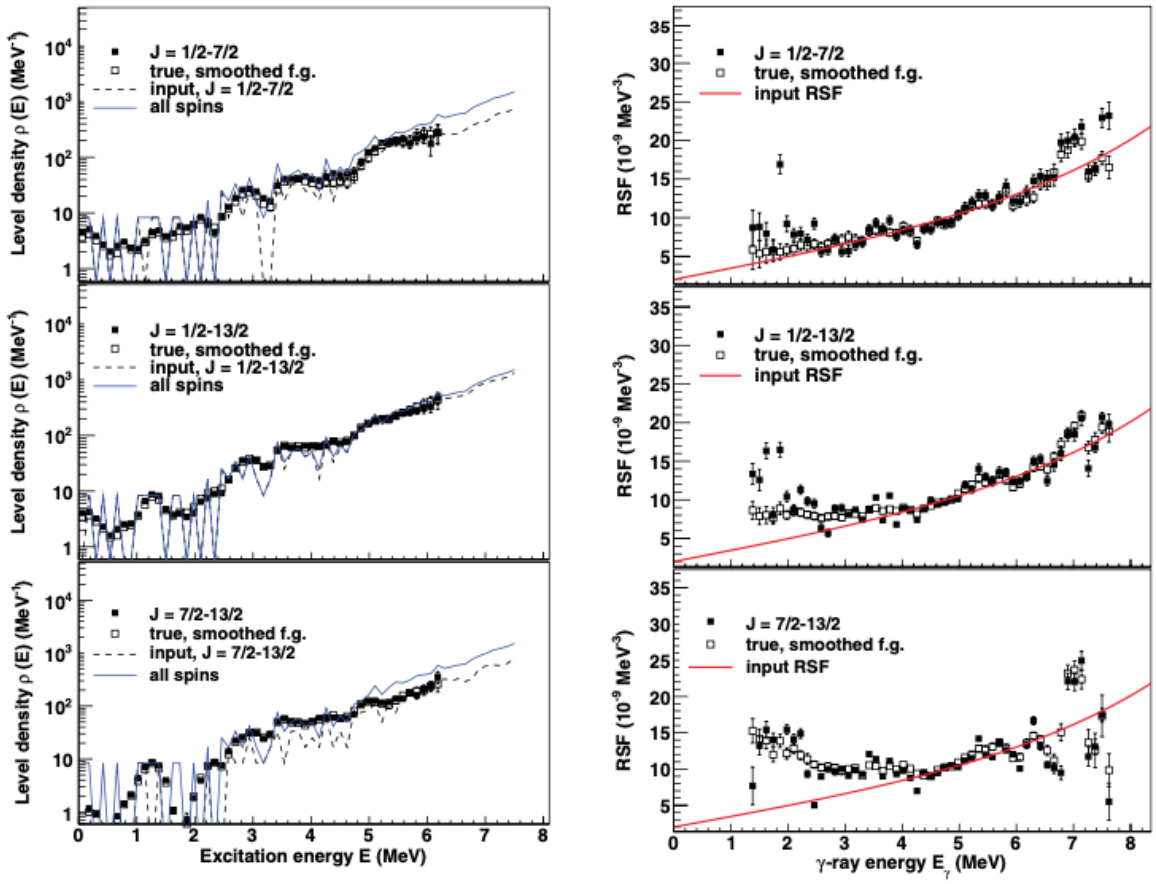


Figure 3.10: The three initial spin ranges used and their effects on NLD (left) and γSF (right). The spin ranges are $1/2 \leq J \leq 7/2$ (top), $1/2 \leq J \leq 13/2$ (middle) and $7/2 \leq J \leq 13/2$ (bottom). On the left the blue solid line represents the NLD over all the spin ranges, the dotted line is the input data for specific spin ranges. On the right the solid red line represents the input γSF. The open squares shows the smoothed first-generation data the closed squares shows the data on the specific spin range. The data displayed is for the ^{57}Fe isotope [13].

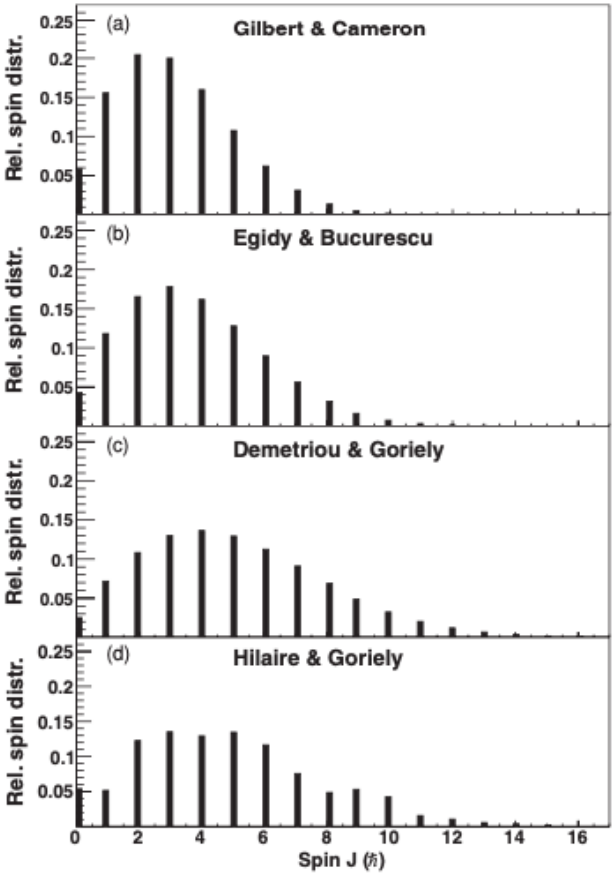


Figure 3.11: Relative spin distributions for ^{44}Sc at $E_\gamma = 8.0$ MeV which are used in calculating level density at S_n [13].

3.7.2 The Unfolding method

The unfolding method has already been explained in section 3.1 and also in great detail in Ref [78]. It is a method where consecutive subtractions of the Compton background are performed. The reliability and accuracy of the method has been proven and tested in earlier work [61,88,89] and it was found to be reliable. In this method the γ-ray spectrum is corrected for the total absorption efficiency of the NaI(Tl) crystal for specific E_γ [13]. The level density extracted through this method doesn't show any responsiveness to the total efficiency, whereas the slope of the γSF increases when the efficiency is too small for high energy γ-rays which result in a very big correction in the unfolding method. The overall shape of the γSF, is maintained [13].

3.7.3 The first-generation method

The first-generation method is based on the assumption that the γ decay from any excitation energy state does not depend on how the nucleus was excited to that particular state. Thus the decay routes in which the γ decays are the same whether the γ-ray was excited by the reaction or it is a result of γ decay from a higher energy state. The assumption is proven to be true when states have the same cross section while they have been populated trough the two different processes, because γ branching ratios are properties of the levels on their own [13]. Testing the assumption can be performed by studying the same compound nucleus that has been populated using different reactions [13].

It is safe to assume that before γ-ray emission the nucleus is in a compound state. Because the time taken to create an absolute compound state is $\approx 10^{-18}s$ [13], whereas the average lifetime of states in the quasi-continuum is $\approx 10^{-15}s$. So the nucleus is thermalized before γ-ray emission.

The assumption was supported by calculations showing that two different nuclei under going two different reactions both had small pre-equilibrium contributions for γ energies below 10 MeV. These nuclei and reactions are ^{160} Dy(^{3}He, $\alpha\gamma$) with 45 MeV [90] and ^{46} Ti(p,p' γ) with 15 MeV. When it comes to excitation energies exceeding 10 MeV the assumption does not properly hold, its not entirely true in this range. All experiments that are analyzed using the Oslo method work specifically with excitation energies at 10 MeV and below.

The low-energy part of the γSF is affected by nuclei that have large energy gaps between energy levels called "empty valleys" these are the areas that have very few events, which should be excluded in order to prevent over or under subtraction [13].
The results of the study are not influenced by the errors in the weighting functions, such as the imperfections of the particle telescopes or CACTUS array, which are finite in their resolution [13].

3.7.4 The Brink hypothesis and the extraction of the NLD and γSF

According to the generalized Brink-Axel hypothesis, the γSF is not dependent on conditions of the initial or final state, such as excitation energy [13]. This hypothesis fails

when the nuclear reaction takes place at high temperatures and high spins. The type of reactions analysed by the Oslo method have low temperatures and low populated spins, so this allows for the assumption of the generalized Brink-Axel hypothesis with no disturbance in the relatively low excitation energy region studied. Based on simulations done in Ref. [13], it is clear that the overall shape of the γSF is similar when the strength function is temperature dependent, but the low γ-ray energy region changes. Experimental searches and analyses have been performed several times with different reactions to support the assumption of temperature dependence of γSF. More information can be taken from the following Refs [55, 62, 88, 91]. The Oslo experiments do not show any strong evidence of temperature dependence in the strength function around the excitation energy region, therefore the Brink-Axel hypothesis holds for such experiments.

Chapter 4

Experimental setup

The ^{152}Sm$(d,t)^{151}$Sm experiment was performed and the data collected at the Oslo Cyclotron Laboratory, a nuclear physics laboratory at the University of Oslo, known to be one of its kind in Norway. The layout of the facility is shown in the schematic diagram in Fig 4.1. The diagram shows the entire layout from the MC-35 Scanditronix cyclotron, beam pipes up to the experimental station which are SiRi [60] and CACTUS [92] arrays. The MC-35 Scanditronix cyclotron provides pulsed beam from an ion source. The beam of approximately 15 MHz frequency is directed and focused by collimator slits and auxiliary magnets along the beam pipes. The quadrupole magnet Q1 and the slit D1 are used to focus the beam and to make it accurately parallel, respectively. The beam is further bent 90° towards the target chamber by the analyzing magnet. The quadrapole magnets Q2 and Q3 also focus the beam further as slits D2, D3 and D4 are responsible for further collimation of the beam towards the target chamber. When the beam reaches the target it has a diameter of approximately 1-2 mm.

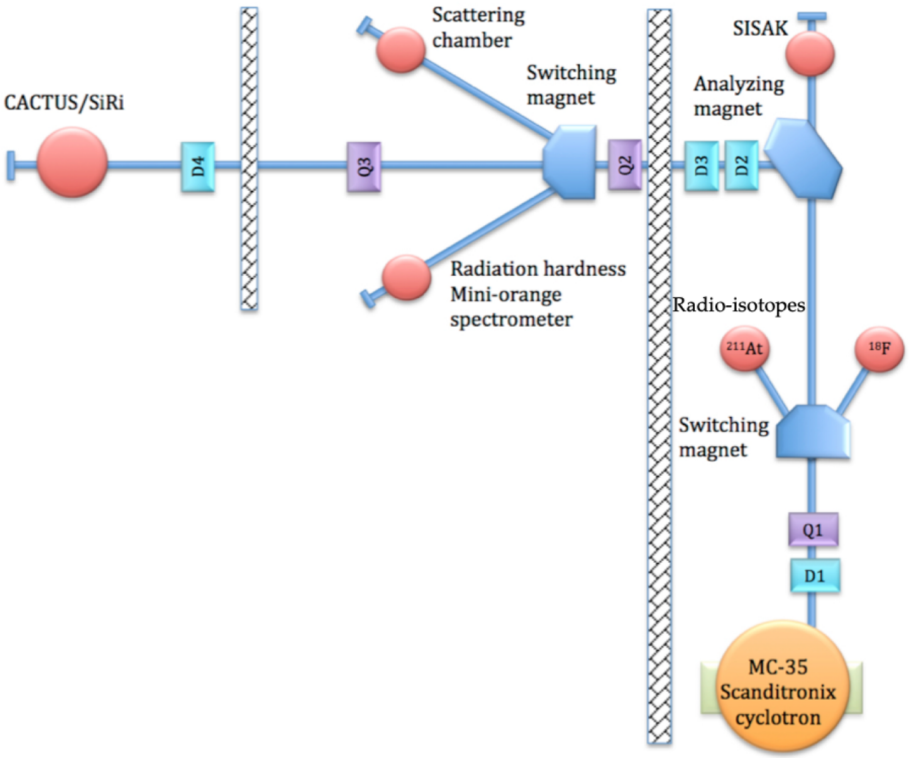


Figure 4.1: The facility layout at the Oslo cyclotron laboratory figure taken from [93].

4.1 Detector systems

The two detector systems that are at the core of this measurement are the CACTUS and SiRi arrays. CACTUS is set around the target chamber and SiRi is set inside the target chamber.

4.1.1 The CACTUS detector array

The sodium iodide NaI(Tl) scintillator detectors arranged in an array called the CACTUS because of its shape that resembles a cactus plant. This detector array is responsible for the detection of the γ-rays. It is made up of 26 $5in \times 5in$ NaI(Tl) detectors mounted around the target chamber as shown in Fig 4.2.
The NaI(Tl) detectors are positioned 22 cm away from the target. Each NaI(Tl) is covered on the front surface by a lead collimator of 10 cm thickness and 7 cm diameter. So the array covers a solid angle of 16 - 17% of 4π.
CACTUS has a total efficiency of approximately 14.1% and an energy resolution of approximately 7% FWHM for a 1332 keV γ-ray transition.
Furthermore, each NaI(Tl) detector has a fixed 2mm thick copper absorber in front that is used to suppress X-rays. A 3mm thick lead shield surrounds each NaI(Tl) detector to avoid crosstalk between detectors close to each other.

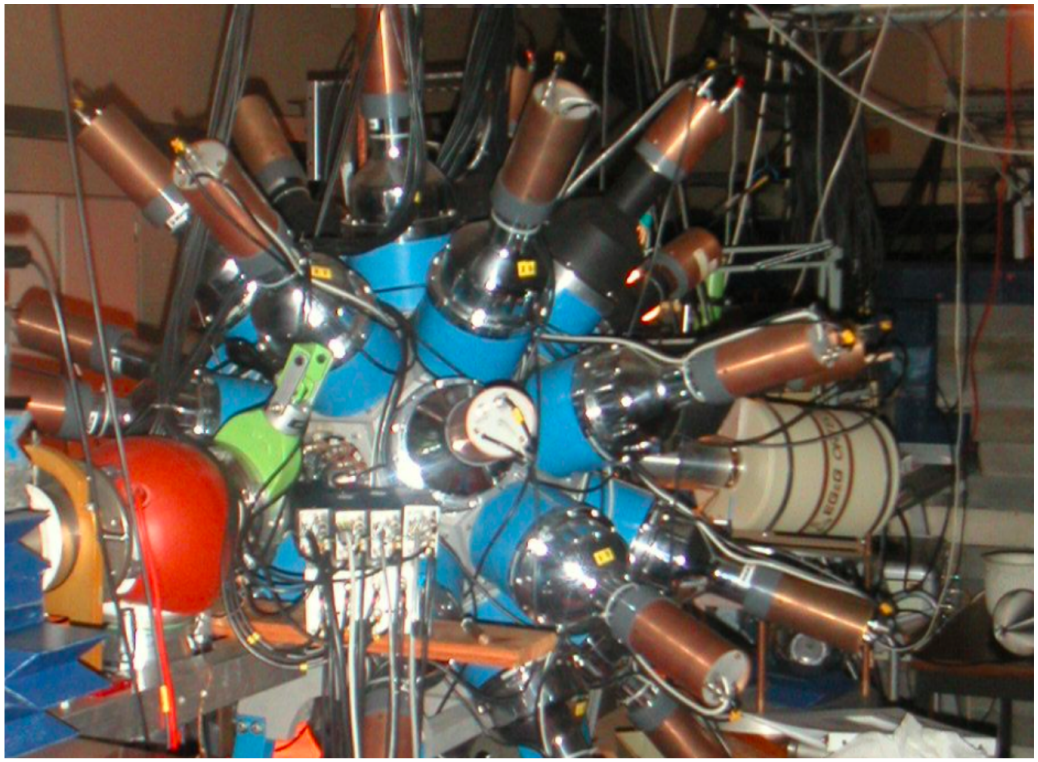


Figure 4.2: The NaI(Tl) multi-detector array CACTUS [72].

4.1.2 SiRi particle telescope

The SiRi array is a ring that consists of 8 silicon detector chips each of which is divided into 8 strips. The strips are further divided into a thin front detector of approximately

130 μm and a thick back detector of approximately 1550 μm (see Fig.4.3). This gives a total of 64 silicon detectors.
The array detects charged particles from the nuclear reactions and it is mounted inside the target chamber inside the CACTUS detector frame.

The relative energy resolution for SiRi usually doesn't go above 350 keV for the current work it was 120 keV with a solid angle coverage of approximately 6%. The strips on the detectors cover scattering angles between 126° to 140° as illustrated on Fig. 4.3.
The SiRi particle telescope for this experiment was placed at 133° backwards angles at a distance of 5 cm away from the target. An aluminium foil of 10 μm thickness was also placed in front of the detector to prevent electrons emitted by the target atoms during the reaction from reaching the detector.

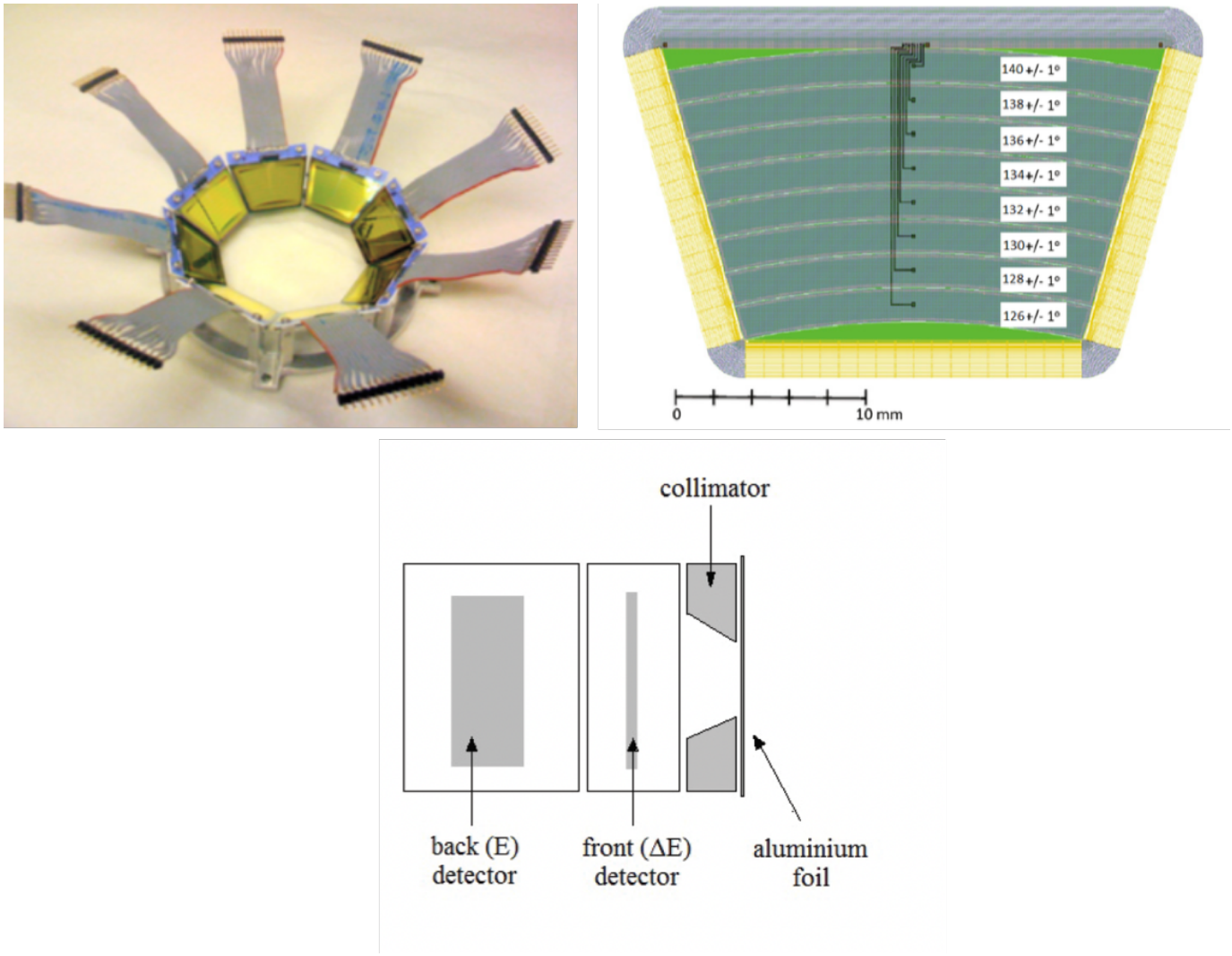


Figure 4.3: The SiRi particle telescope (top right). Layout of the front ΔE detector (top left) and a schematic presentation of each detector strip divided into a thick back detector and a thin front detector(bottom) [94].

4.1.3 Electronics

Figure 4.4 illustrates how the electronics are set up and function. The photo-multiplier tubes of the scintillation detectors are powered by the Caen SY2527 Universal Multichannel Power Supply System at the OCL. The photo-multiplier tubes were biased with high voltage of 700-800 V. The particle detectors were biased to 30 V for the ΔE detectors and to 350 V for the E detectors, using the Mesytec MHV-4 modules.
Signals from ΔE and E particle detectors are divided into two part. One part moves to a spectroscopy amplifier and an Analog-to-Digital Converter (ADC) where it is temporarily stored until it receives an energy signal to be stored on a disk from Mesytec (MADC-32).

The other part moves through time filter amplification (TFA) and leading edge discriminator (LED) modules to a coincidence module as shown in Fig. 4.4. In the coincidence module a $200ns$ window is set to determine if true charged particle events are identified by the signal. The charged particle signal is then sent to another coincidence module where particle-γ coincidences are determined.
The signals from the NaI(Tl) scintillation detectors are also divided into two parts, one part moves to a spectroscopy amplifier and the ADC where it is temporarily stored until it receives an energy signal to be stored on a disk. The other part moves through the TFA and the LED modules where it is further divided. One part is sent to a Time to Digital Converter (TDC) where it is temporarily stored until it receives an energy signal to be stored, the other signal connects to a coincidence module see Fig. 4.4.

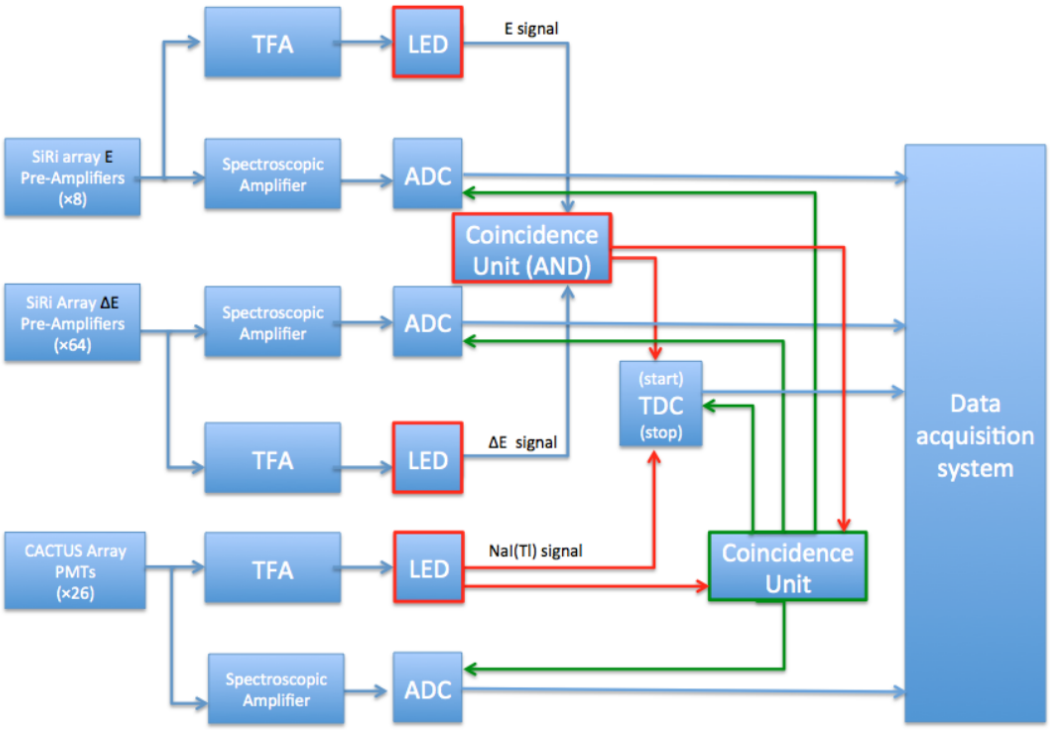


Figure 4.4: The schematic diagram of the electronics used at the Oslo Cyclotron laboratory [95].

The NaI(Tl) scintillators are inherently faster than charged particle semi-conductor detectors such as SiRi, so the NaI(Tl) detector signals are delayed by 400 ns. The delay is a consequence of the peak in the γ-ray spectrum at the coincidence time having a certain width, the width is to make sure that the full distribution is included. The delay is also

important to guarantee that charged particles and γ-rays overlap. Hence the charged particle signal is used as a start signal to open the gate in the TDC module and the NaI(Tl) signal as stop signal.
When a signal reaches the threshold in the discriminator of an E detector it opens a master gate for the ADCs for 2 μm and with TDCs for 1.2 μm. This is done so to start the acquisition of an event.
The particle-γ events are used as trigger signals in the ADC and TDC as shown in Fig 4.4.

4.2 Target and Reaction

The ^{152}Sm$(d, t\gamma)^{151}$Sm reaction was investigated. A pulsed deuteron beam of 13.5 MeV with approximately 0.2 nA of intensity was provided. The provided beam bombarded the self-supporting samarium (^{152}Sm) target for the experiment. The ^{152}Sm target was 98.27% enriched. To reach the desired $2,9$ mg/cm^2 thickness the target was rolled using mechanical rolling because of Sm's ductility it can be easily deformed. The experiment was run for 5 days and data was collected throughout.

The ^{28}Si$(d, p\gamma)^{29}$Si reaction was used for calibration. This was chosen because ^{29}Si has well defined γ-transitions that made it easy to calibrate the detectors, since it provided clear and enough calibration points. The self-supporting ^{28}Si target was placed in the target chamber for some time, under the same conditions as the ^{152}Sm target.

Chapter 5

Data analysis

5.1 Calibration

5.1.1 The SiRi array

The detectors need to be calibrated before the actual analysis. Calibrating the SiRi array, the peaks produced from the experiment were fitted to compare with calculated peaks. The kinematics calculator called Qkinz [96] was used to determine the expected data outcome. This calculator operates using the Bethe Bloch formula [97, 98]. The formula accounts for the energy loss of a particle moving into a material. It puts into consideration the following parameters: the atomic number of incident particle, the atomic number of the material, atomic mass of the material and maximum energy transfer in a single collision. When a particle hits the SiRi array, it passes through the aluminium into the thin front detector (ΔE) where it releases some of its energy, the particle then proceeds to release the rest of its remaining energy in the thick back detector E.

The charged particles can be easily differentiated by their number of protons and masses, which allows for separation of the different reaction channels as shown in Figs. 5.1 and 5.2. In Figures 5.1 and 5.2 the first peak from the top represents tritons detected by the set of detectors, the middle one represents the deuterons and the last one represents the protons. Fig. 5.3 is a projection of Fig. 5.2 showing the $\Delta E - E$ detectors with peaks representing different particles as indicated. In this study we are focusing on the tritons detected making our reaction of interest ^{152}Sm(d, tγ)^{151}Sm. The triton peak was gated to reduce background when performing the calibrations.

The black lines on Fig. 5.4 are showing the energy values expected from the reactions when a deuteron beam of 13.5 MeV interacts with the detector at backwards angles of $\theta = 133°$, notice that each curve corresponds with the ones from SiRi kinematic calculator (black lines) Qkinz [96]. The y-axis represent energy lost by the particle in the thin front detector and the x-axis represents the energy lost by the particle in the thick back detector.

To calibrate the experimental data, any two or more of the experimental peaks that are a few MeV apart on the E and ΔE axis, are measured and then fitted to their corresponding computed peaks. A 3.5 mg/cm^2 ^{28}Si target was also exposed to the same experimental conditions for calibration purposes, this target was chosen because it dis-

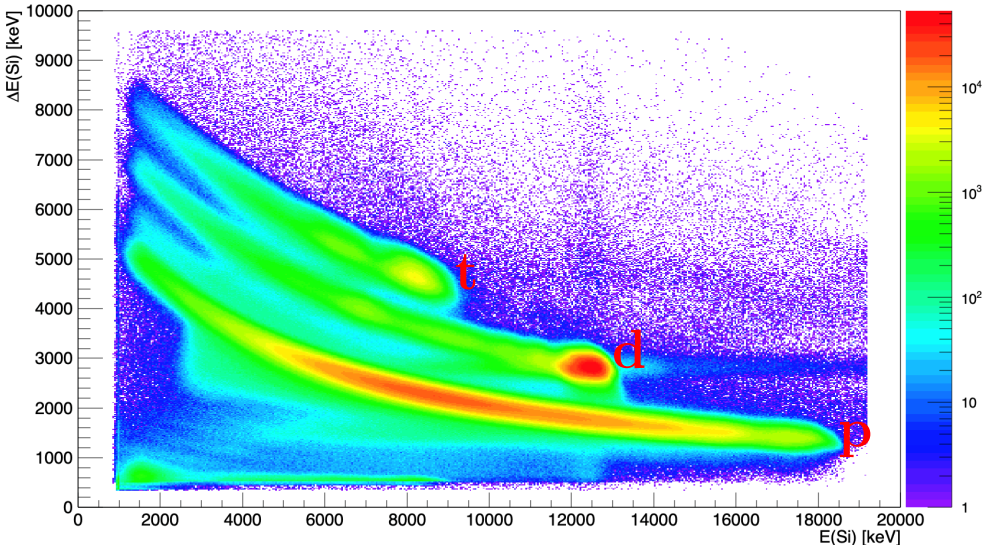


Figure 5.1: Energy signals detected in $\Delta E - E$ detectors, showing the reaction channels before calibration, this plot is known as the banana plot for ^{152}Sm(d,X) where X = pγ, dγ, and tγ.

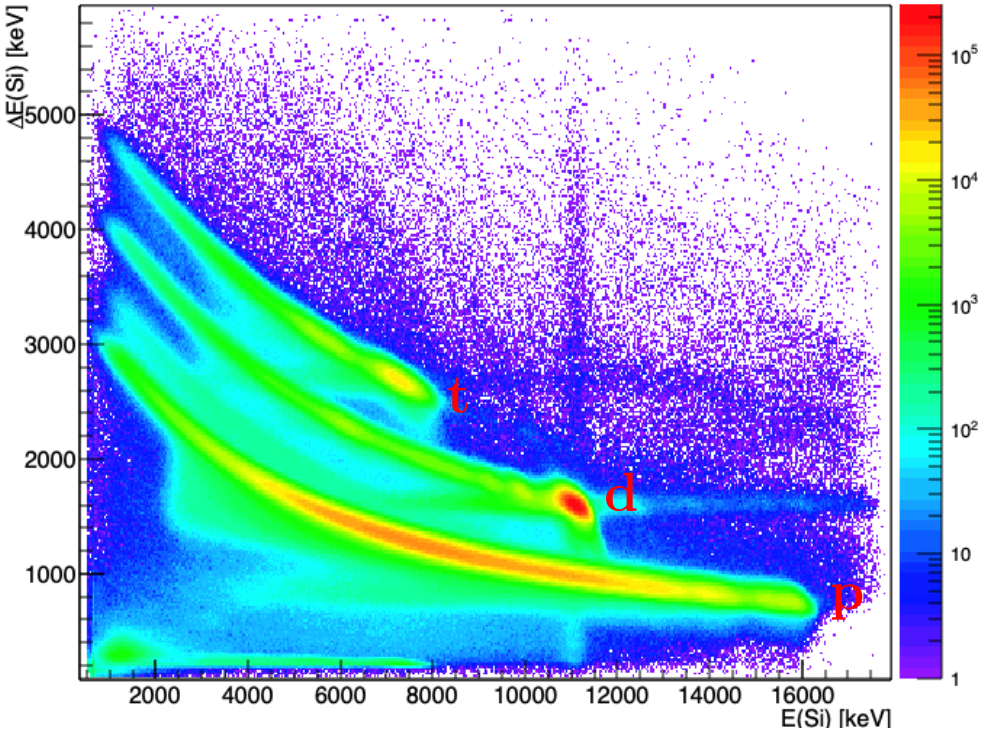


Figure 5.2: The energy detected in $\Delta E - E$ detectors, calibrated reaction channels.

plays well separated peaks making calibration easy (see Fig. 5.5). To calibrate the Sm data the samarium triton peak [^{152}Sm(d, tγ)^{151}Sm] and the silicon deuteron peak [^{28}Si(d, pγ)^{29}Si] were used and for the Si calibration ^{28}Si(d, pγ)^{29}Si the deuteron peak was used.

Most of the random events in the uncalibrated figures are removed by a time gate. A time gate is set on the apparent thickness for the particle of interest using its curve, apparent thickness refers to the distance the particles travels through the E detector. The proton and triton gates shown in Fig. 5.6 and 5.7, respectively, are good for getting rid of random events. By setting these gates background events are removed and so are events

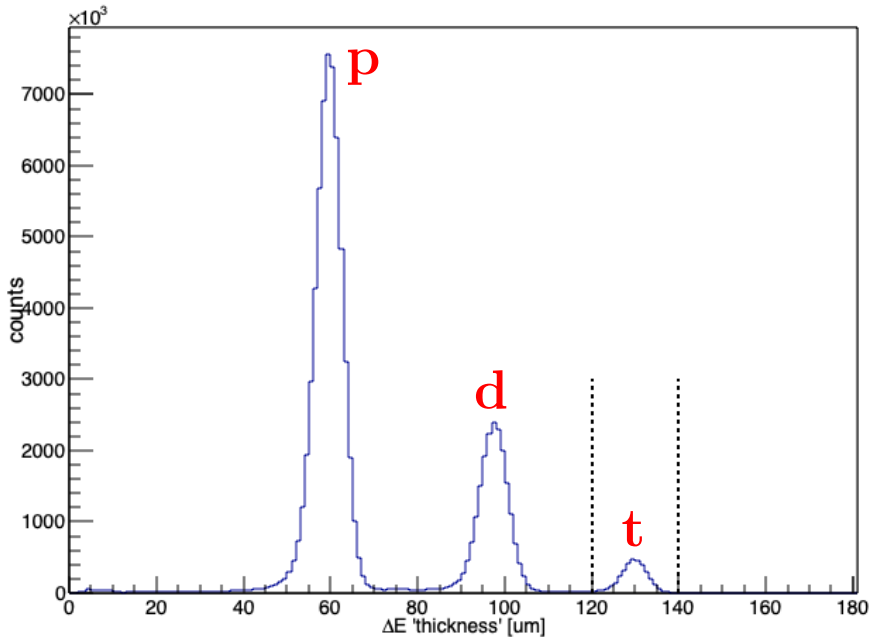


Figure 5.3: The range spectrum showing the depth at which each particle traveled inside the E detector, note the dotted lines are representing the particle gates for the ^{152}Sm(d, tγ)^{151}Sm reaction.

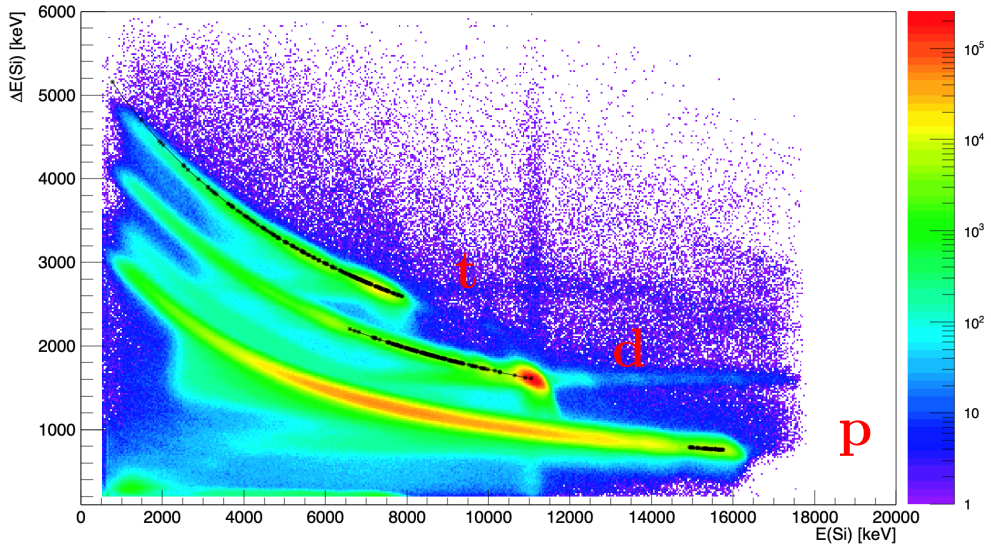


Figure 5.4: The energy detected in ΔE– E detectors, calibrated reaction channels plotted together with the calculated values from the kinematic calculator.

from other charged particle, making it easy to focus on the particle of interest. Now that the SiRi array has been calibrated, we can extract the excitation energy spectrum. The triton energy measured for the ^{151}Sm data was converted into excitation energy using total kinetic energy and Q-values of the reactions through the following equation:

$$E_x = KE_{beam} - KE_{ejectile} - KE_{recoil} - E_{loss} + Q_{value}, \tag{5.1}$$

where KE_{beam} is the beam energy, $KE_{ejectile}$ is the kinetic energy of the ejected particle, E_{loss} is the energy lost by the ejectile through the aluminum foil in front of the SiRi

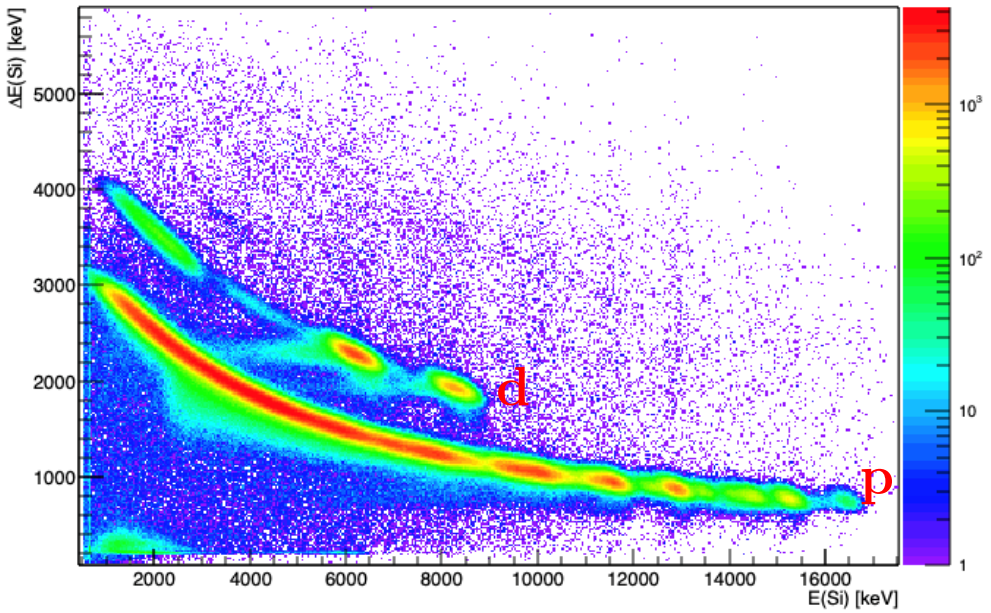


Figure 5.5: The energy detected in ΔE– E detectors, calibrated for the ^{28}Si(d,X)^{29}Si reactions, this was used to calibrate the particle detector.

detector and through the target, KE_{recoil} is the recoil energy of the target nucleus and finally the Q_{value} of the nuclear reaction. The Q value of the ^{152}Sm (d,tγ)^{151}Sm reaction is Q_{value} = 2000.4 keV.

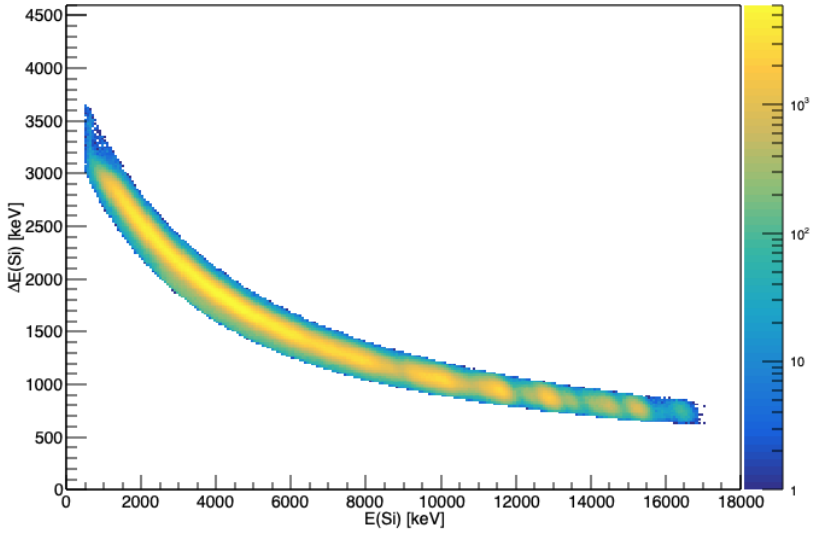


Figure 5.6: The calibrated peak plot for the ^{28}Si(d,pγ)^{29}Si reaction, gated on the ejected protons.

5.2 CACTUS array

In a gamma detector if the incident photon energy is larger than twice the rest mass of the electron which is 1.022 MeV, pair production can occur which results in the production of two 511 keV annihilation γ-rays, it is possible that after the annihilation one of the two

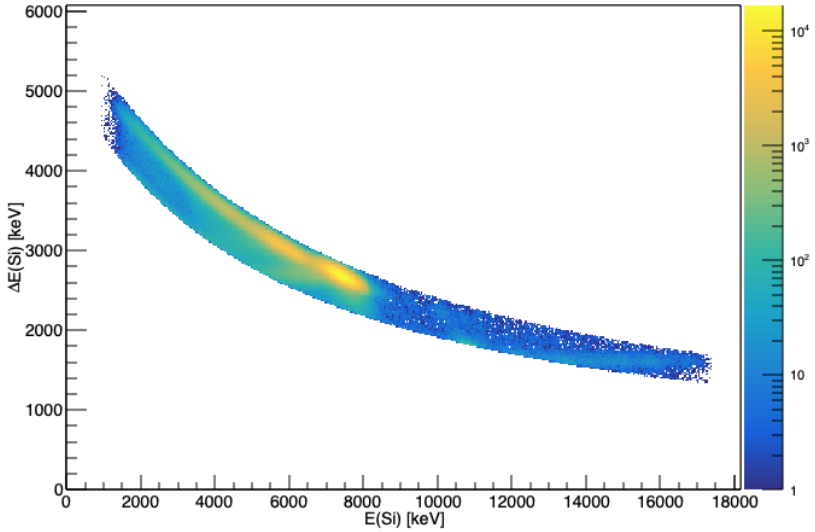


Figure 5.7: The calibrated banana plot for the ^{152}Sm (d,tγ)^{151}Sm reaction, gated at the ejected tritons.

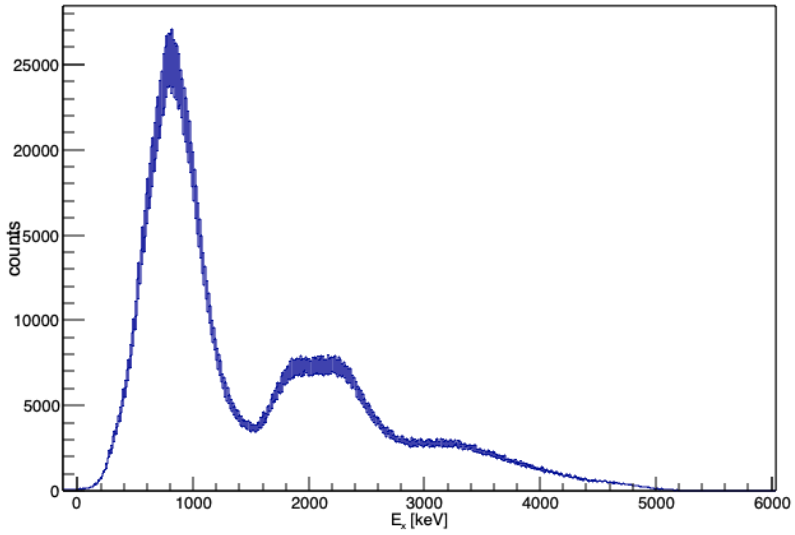


Figure 5.8: The calibrated excitation energy spectrum of the ^{152}Sm(d,tγ)^{151}Sm reaction.

γ-rays escapes the detector and only one of the γ-rays deposits its energy in the detector, giving a peak with E - 511 keV, this is known the single escape peak. This is how we end up having the peak just before the E_x = 4933 keV state. The γ-spectrum in Fig. 5.10 is a result of gating on the E_x = 4933 keV state from Fig. 5.9 on the proton excitation spectra of ^{29}Si. To calibrate the γ-spectrum in Fig. 5.10 the peaks at 1793 keV and 4933 keV were used to align the NaI(Tl) detectors. ^{29}Si was used to calibrate the CACTUS array because it has many well-defined γ-transitions making available clear calibration points which are also available on online National Nuclear Data Center (NNDC) for confirmation [99].
To check if the calibration of the ^{151}Sm E_x is accurate several states were gated on to

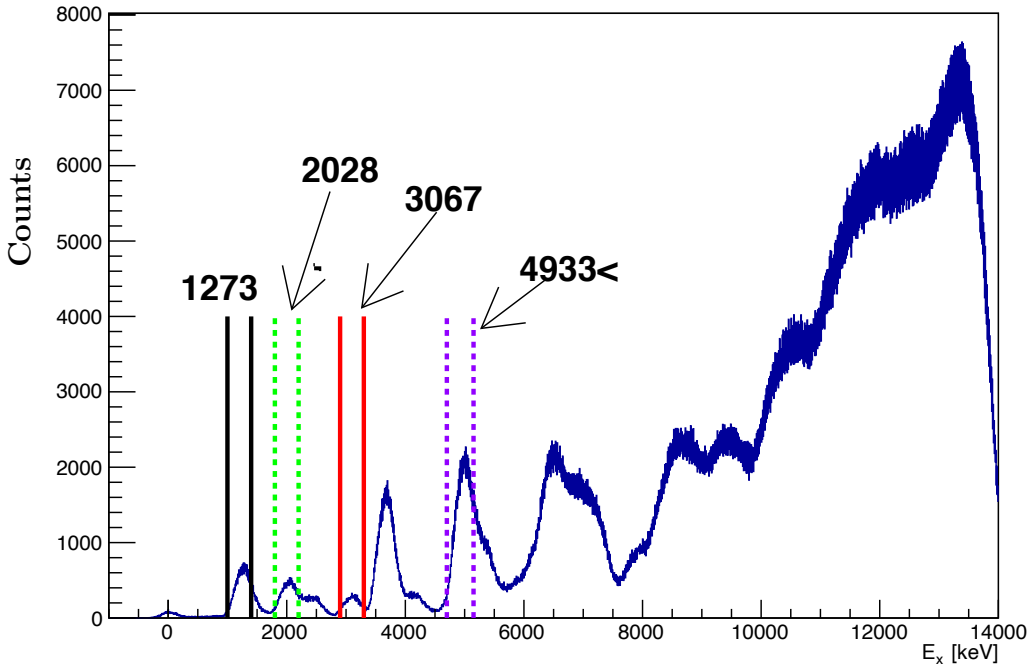


Figure 5.9: The calibrated excitation energy spectrum of the ^{28}Si(d,pγ)^{29}Si reaction.

Table 5.1: γ - ray photo peaks on each gated state used while calibrating the γ -ray detector array CACTUS, the information on the γ -rays and states studied was taken from [99]

State(keV)	γ - ray photo peaks (keV)
1273	1273
2028	1273 , 2028
3067	1273 , 1793
3623	1595 , 2028
4079	1273 , 2806
4741	1273 , 2028
4895	1273 , 3621
4933	1273 , 3621, 1793, 4933

ensure that the γ-rays decaying from each state have the expected corresponding E_x. These gates were set on the ^{29}Si spectrum since ^{29}Si has clear states compared to ^{151}Sm, the calibration coefficients obtained were then used in calibrating the ^{151}Sm data. The calibration was thought to be reliable because gating on a less populated state would still produce a clear γ-ray spectrum with visible known energy peaks, as gating on a more populated energy state. In Fig 5.11 it can be seen that the γ-ray spectrum that results from the gate on the 2028 keV state only shows γ-rays decaying from that state, and the 4933 keV gate only shows γ-rays decaying from the 4933 state. The NaI(Tl) detectors were calibrated based on a linear calibration between expected energy deposit and the corresponding recorded spectrum channel number.

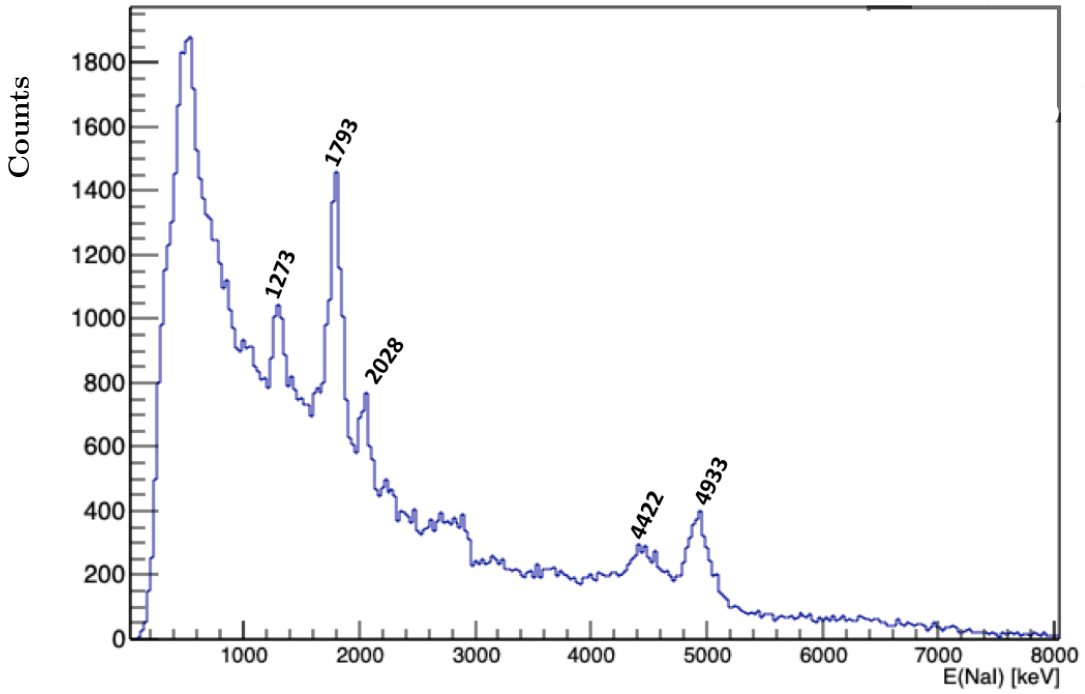


Figure 5.10: The calibrated gamma ray energy spectrum of ^{29}Si.

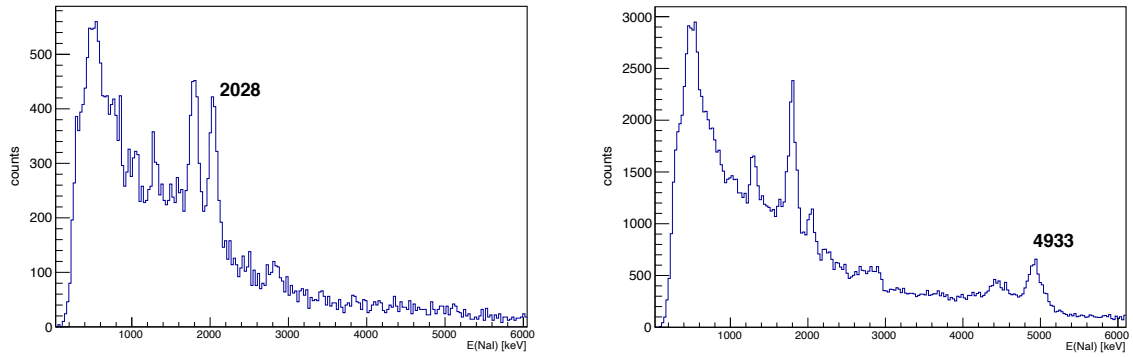


Figure 5.11: The γ-ray spectra gated at the 2028 and 4933 states as labeled, these shows how when a gate is placed on a certain excitation energy the spectrum will only retain γ-rays decaying from the gated excitation energy.

5.3 Time Calibration

The particle-γ events are recorded using the time-to-digital converters. The gamma (open signal from CACTUS) passes first to open the gate of the LED and the particle (close signal from SiRi) passes last to close the gate. NaI(Tl) detectors have a delayed response in time signal, the leading edge discriminator (LED) is used to align the time signals. The LED collects information from both sets of detectors. The different signals pass the threshold of the LED at different times. Because high energy events have high signal amplitudes and low energy events have low signal amplitudes, so high energy signals will pass the LED before the low energy signals even if they occurred at the same time see Fig. 5.12 the events are not aligned yet, then in Fig. 5.13 the events are properly aligned.

This results from what is called the "walk effect". This walk effect makes it hard to obtain precise time information. To correct for the delayed signals and display properly low and high energy signals that occurred at the same time but detected at different times.
To correct for this effect the following equation [92] was used,

$$t(E) = t_0 + \frac{\alpha}{E + \beta} + \gamma(E), \tag{5.2}$$

where t_0 is the time of detection measured and α, β and γ are constants which are found by fitting the energy-time matrix (Fig 5.12). The use of this equation helps to align all the respective channels, Fig 5.13 shows the ^{152}Sm(d,tγ)^{151}Sm time signal after the walk effect has been corrected for, and Fig. 5.14 shows the corrected one dimensional time spectrum.

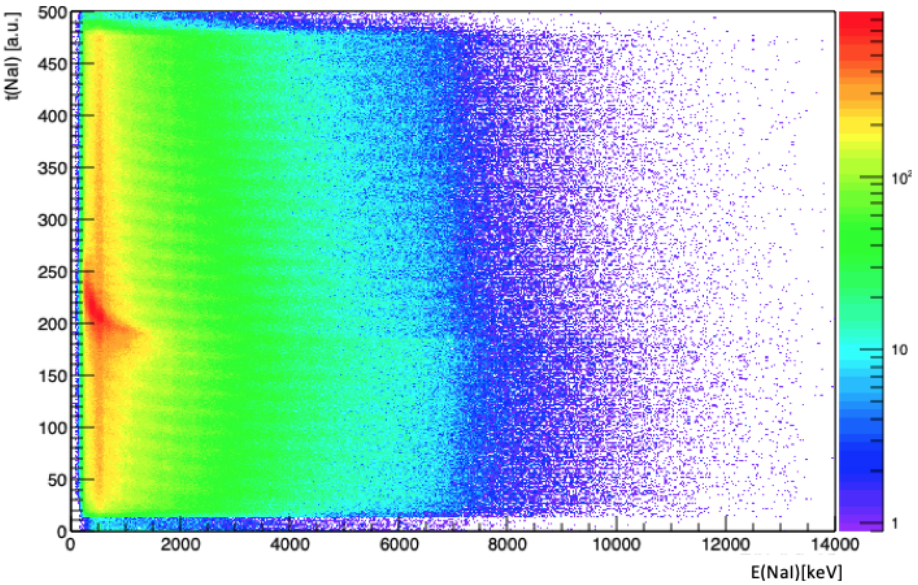


Figure 5.12: The ^{152}Sm(d,tγ) energy vs time matrix for the NaI(Tl) detectors before walk effect correction.

5.4 Particle-γ coincidence Matrix

The excitation energy E_x of the residual nucleus is extracted by gating on the particle of interest, in this case tritons. In addition, by gating on the prompt peak, the γ-rays that were detected at the same time with these particles were identified, leading to the coincidence matrix. Now the excitation energy can be associated with the γ rays detected to produce the coincidence matrix. The coincidence matrix represents the measured γ rays energy spectrum per excitation energy bin. Fig. 5.15 shows the particle-γ matrix for ^{151}Sm.

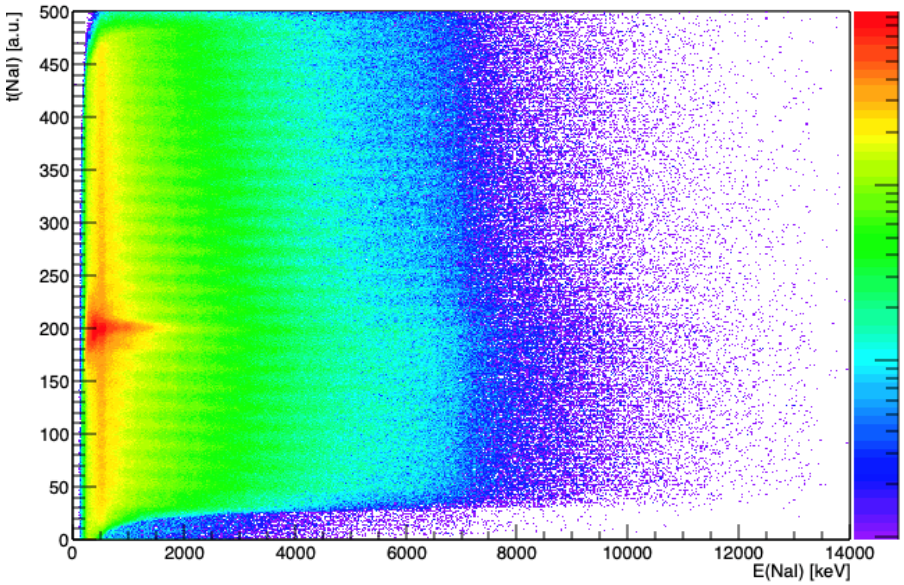


Figure 5.13: The ^{152}Sm(d,tγ) energy vs time matrix for the NaI(Tl) detectors after being corrected for the time walk effect.

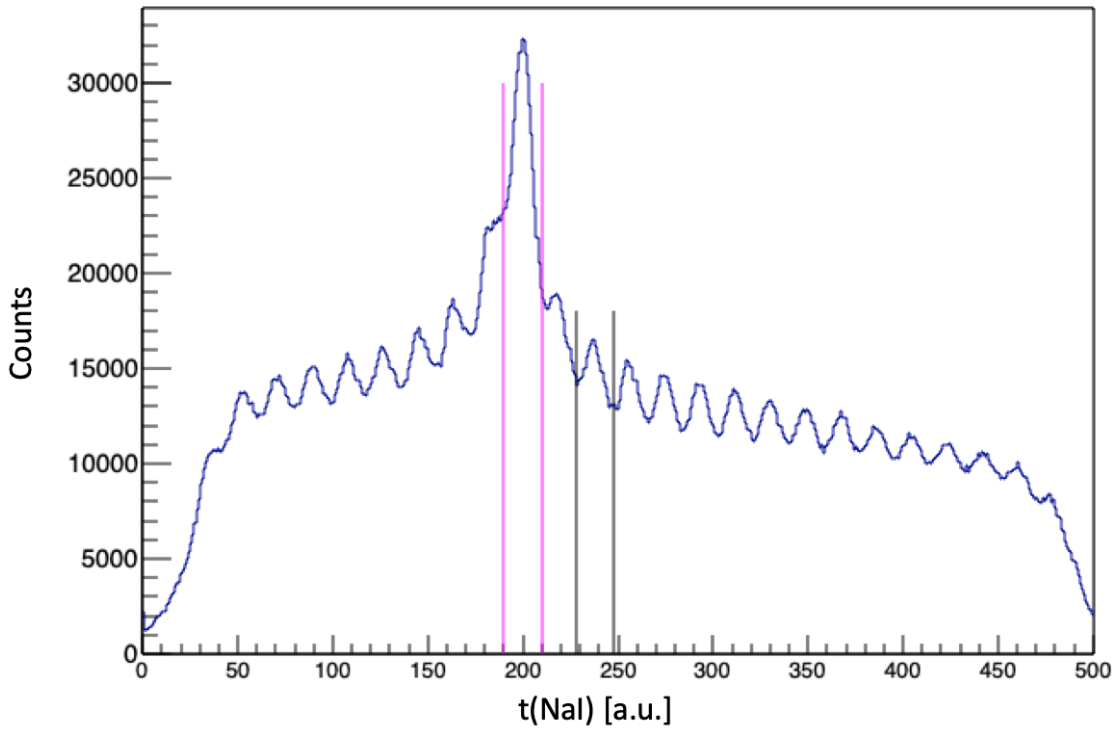


Figure 5.14: The projection of the time matrix from figure 5.13, the pink lines represent the gate on the prompt peak and the black lines represent the gate on the random events which are used to reduce the background.

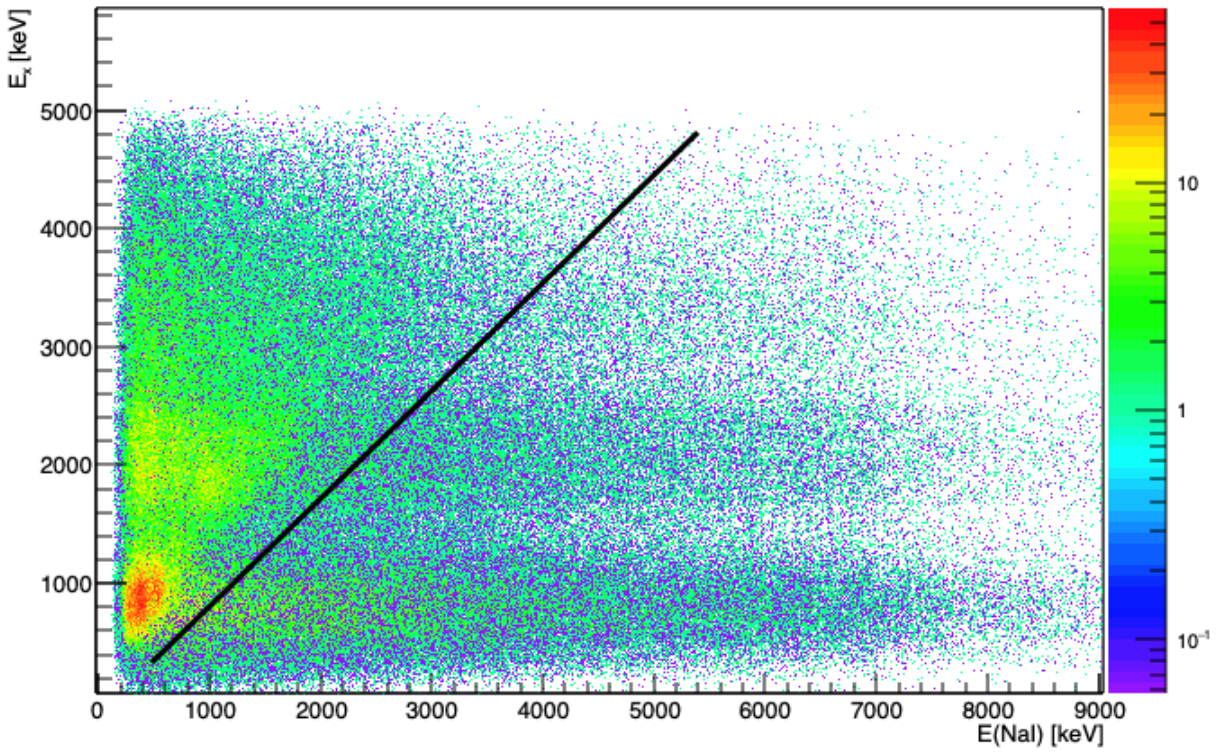


Figure 5.15: The excitation energy-γ ray energy matrix of ^{151}Sm before the application of the Oslo Method, the black diagonal line represents decays to ground state where $E_x = E_\gamma$.

Chapter 6

Results

6.1 Full energy deposits

The raw particle-γ coincidence matrix shown in Fig. 5.15 is then unfolded following the procedure discussed in Sec. 3.1. From the unfolded matrix the full energy deposit γ-rays of the decaying nucleus are extracted. The next step is to extract the NLD and the γSF. It can be observed from Fig. 6.1 that there are no counts towards the neutron separation energy (S_n) of ^{151}Sm which is at 5596 keV [99] and indicated by the dotted line. The less counts maybe caused by the fact that the experiment was not optimised for the population of the (d,t) channel. The S_n is the excitation energy where the nucleus has enough energy to either release a neutron or a γ-ray.
Once a neutron is emitted, the nucleus changes to a lighter isotope of the same element (A-1).

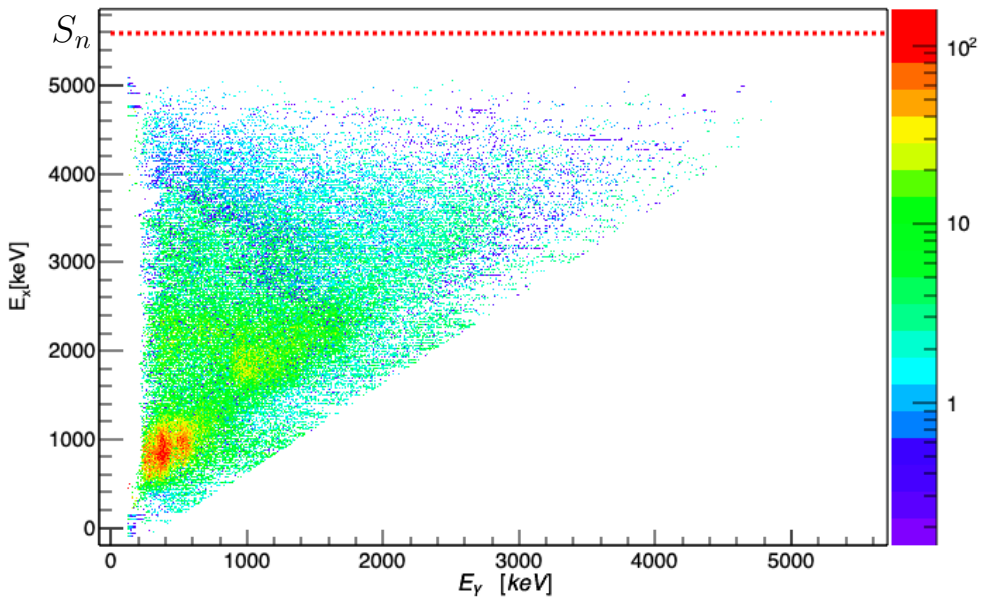


Figure 6.1: The unfolded coincidence matrix for ^{151}Sm and the dotted line represents the S_n. It is observed that the number of counts decreases as E_x increases hence there are no counts towards and at the S_n.

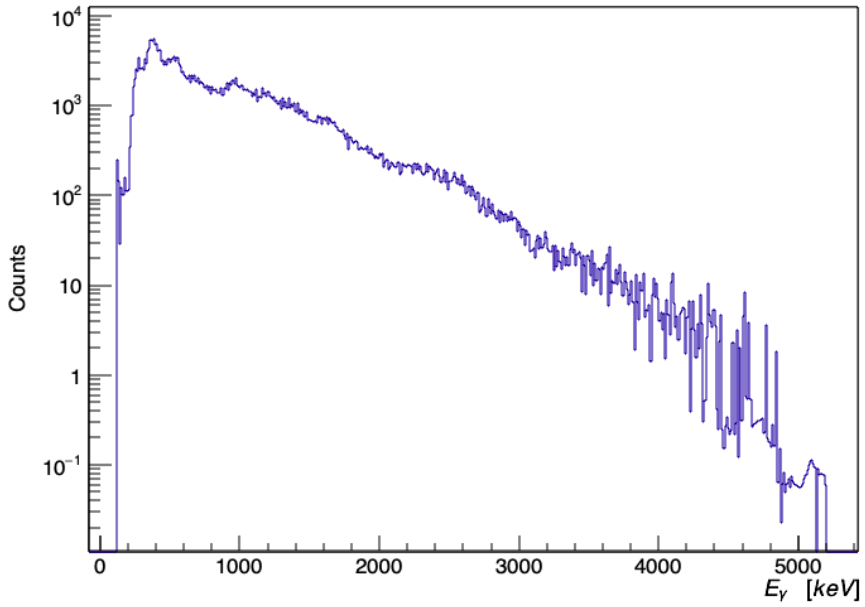


Figure 6.2: The unfolded γ-ray spectrum for ^{151}Sm.

The diagonal line where $E_x = E_\gamma$ observed in Fig. 6.1, shows all the decays to ground state of the decaying nucleus (^{151}Sm). Fig. 6.2 shows the unfolded spectrum projected over the excitation energy levels. The unfolding procedure is performed as discussed in Sec. 3.1.
The low counts observed on high E_γ energies are due to the fact that the experiment was not optimised for the population of (d,t) reaction channel.

6.2 Over subtraction

The first-generation (primary) γ-ray spectrum Fig. 6.4 is extracted from the unfolded matrix using the first-generation method discussed in Sec. 3.4. As illustrated in Fig. 3.7, to obtain the first-generation γ-rays in each bin, the γ- ray spectrum from the lower energy bin must be subtracted from the higher energy bin. Those subtractions are the reason for the gaps observed in Fig. 6.3 at E_x = 0-1 MeV and E_γ = 1.2 - 4.2 MeV. The lower energy states have more counts due to strong γ-ray transitioning compared to higher lying states which leads to over subtraction.

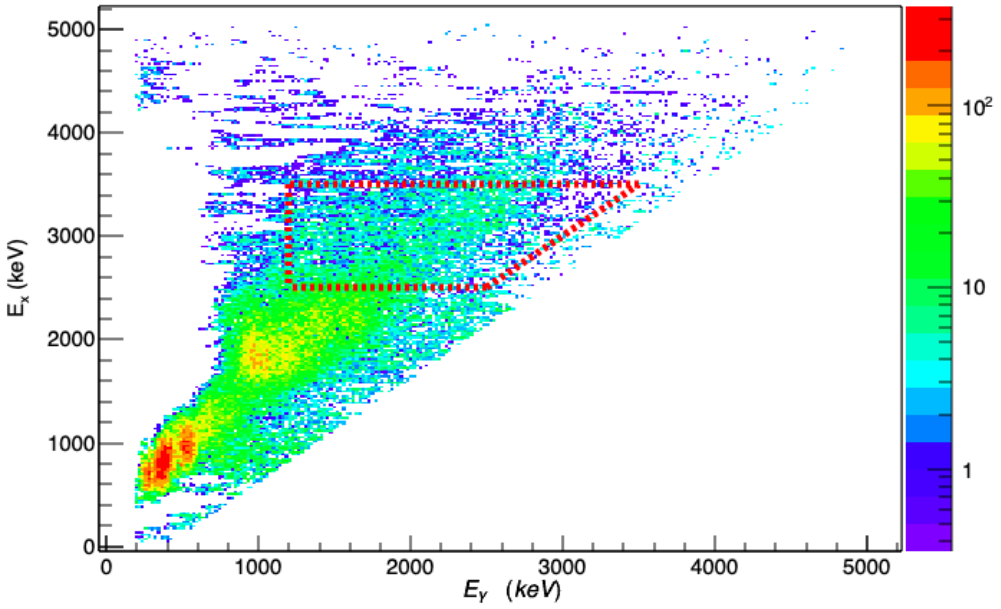


Figure 6.3: The first generation matrix of ^{151}Sm, populated through the ^{152}Sm(d,tγ) reaction. The area marked with red dots represents the energy region used to extract the NLD and γSF.

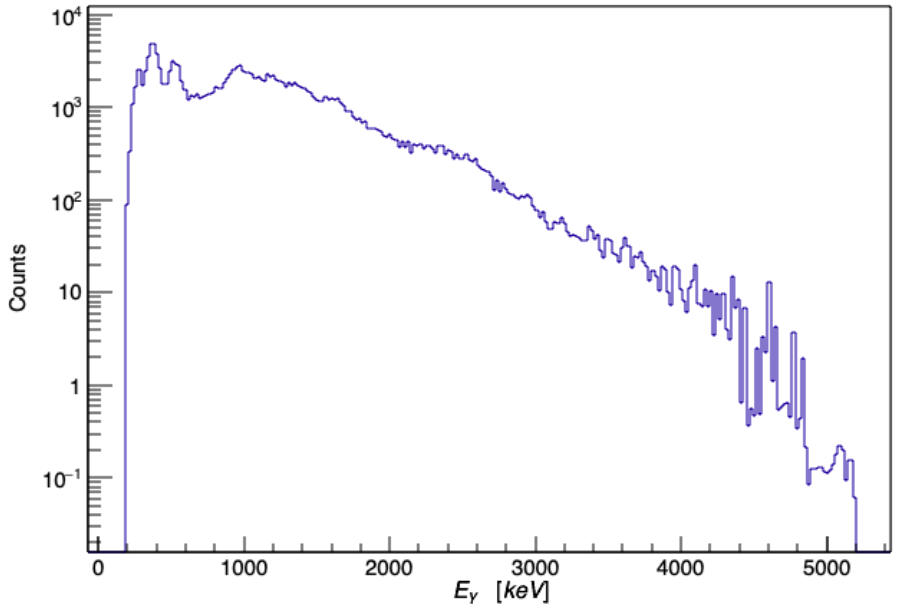


Figure 6.4: The first generation γ-rays spectrum of ^{151}Sm projected on the γ-ray energies E_γ.

The dotted lines in Fig. 6.3 indicate of the area that was used for the extraction of the NLD and γSF.

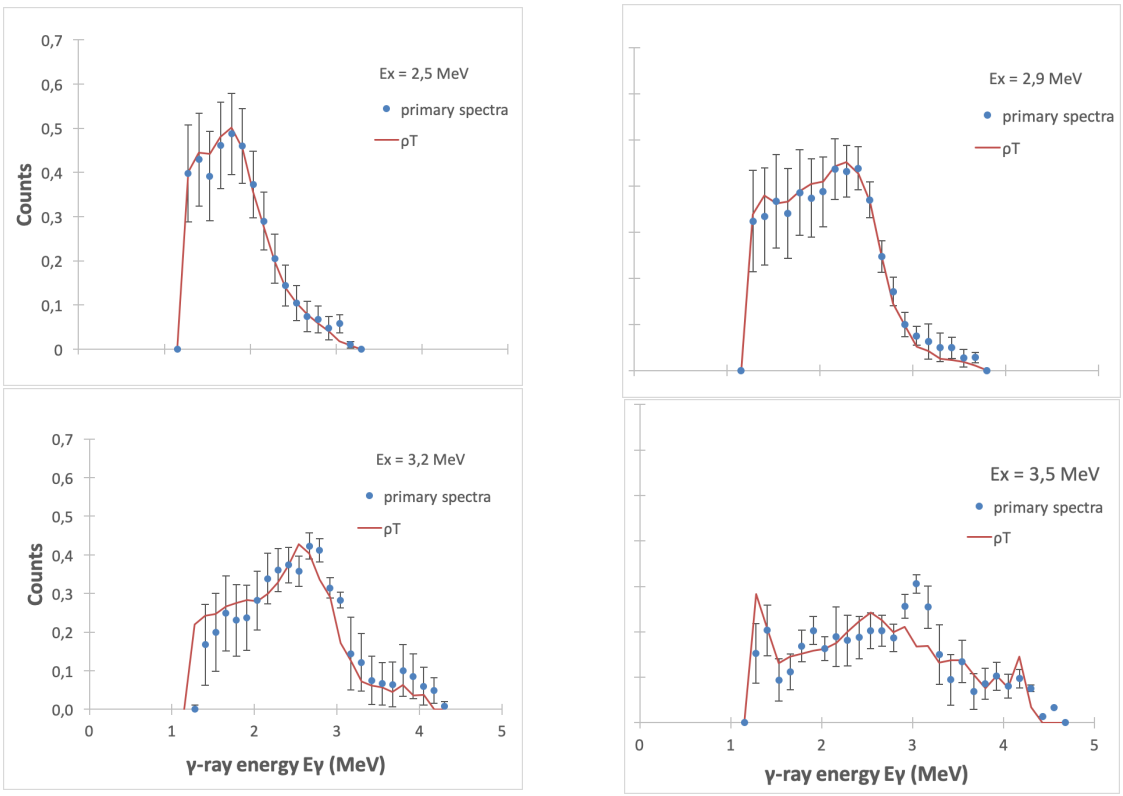


Figure 6.5: Comparing the experimental first generation γ-ray spectra (blue circles) of ^{151}Sm from gated initial excitation energies E_x, to the $\rho(E_x - E_\gamma) \times T(E_\gamma)$ product (maroon solid curve).

Fig. 6.5 shows a comparison between the experimental first generation γ-ray spectra and the product of the NLD and γ-transmission coefficient, which is the theoretical simulation of the spectra. A good agreement is seen throughout, with few discrepancies around 3 MeV of the Ex = 3,5 plot.

6.3 Extraction and normalization of the NLD and γSF

For the extraction of the NLD and γSF, higher ($E_x$max) and lower ($E_x$min) excitation energy limits were set. The higher limit $E_x = 3545$ keV is set to exclude low statistics in the higher energies up to the neutron separation energy. The lower limit was set to $E_x = 2537$ keV to exclude discrete states still observed below 2500 keV.
The NLD and γSF are simultaneously extracted from the first-generation γ-ray matrix. After extraction, these statistical properties must be normalized. For normalizing the NLD and γSF, the normalization parameters which are the s-wave resonance spacing (D_0) and the average radiative width (Γ_γ) were taken from Ref. [100] see Tab. 6.1. The extracted NLD for ^{151}Sm is shown in Fig. 6.6.

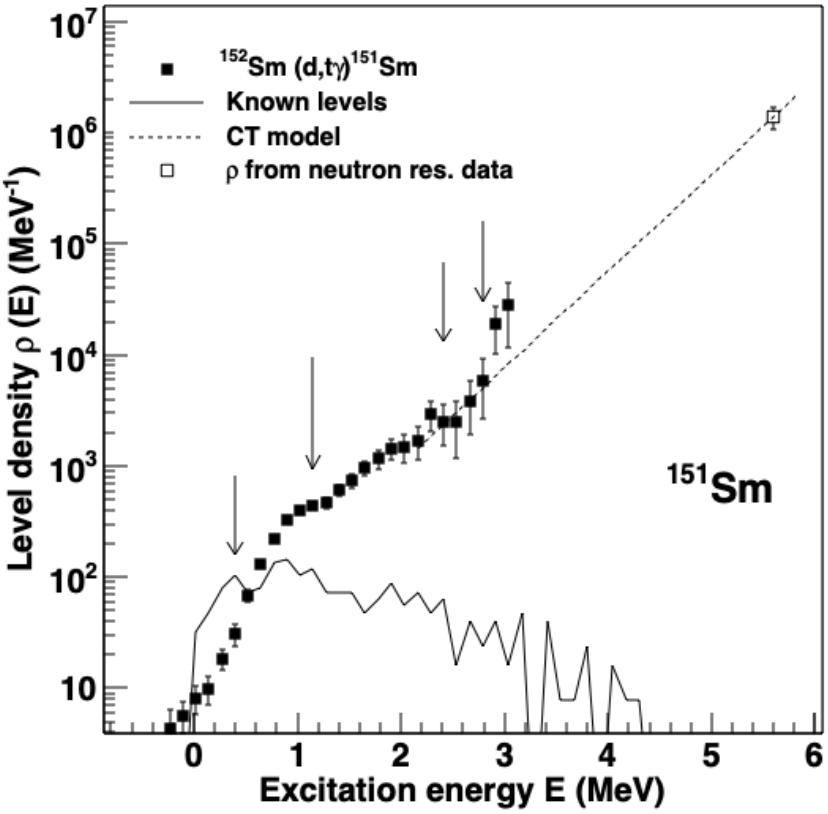


Figure 6.6: The NLD of ^{151}Sm, the black full squares are the experimental NLD extracted using the Oslo method, the open square is the NLD at S_n denoted as ($\rho(S_n)$), the dotted line is the constant temperature model interpolated NLD, and the arrows indicate the normalization points used, the normalization points at low energies are chosen such that the data fits well on the known discrete states and the ones on higher energies is a pair that best align the interpolation to agree with most data points.

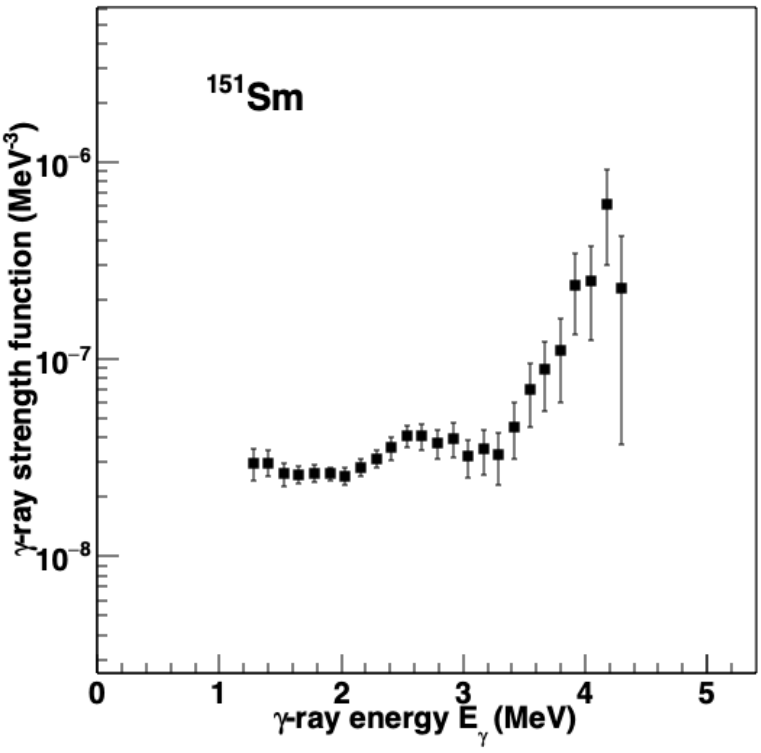


Figure 6.7: The normalized γSF of ^{151}Sm, extracted from the ^{152}Sm(d,t γ) reaction.

The nucleus decays from higher lying energy states to lower lying energy states or to the ground state. The reason why the NLD in Fig. 6.6 appears to have negative excitation energy is to account for the resolution of the SiRi detector. The NLD Fig. 6.6 and γSF Fig. 6.7 are normalized using the following parameters, the resonance spacing D_0, the radiative width Γ_γ, the spin cut off parameter σ, level density at neutron separation $\rho(S_n)$ and the reduction factor η. For the ^{151}Sm nucleus the information is given in Tab. 6.1. σ and η are modelled using the RMI [19], the model was chosen because it does not under or over estimate at different energy regions compared to the other models. For example the other models such as the Fermi gas model underestimates these parameters at high excitation energies.

Table 6.1: The normalization parameters for ^{151}Sm used in this work, with D_0 and $< \Gamma_\gamma(S_n) >$ taken from Ref. [100]. σ and $\rho(S_n)$ are calculated as shown by Eq. 3.30.

Isotope	D_0 (eV)	$< \Gamma_\gamma(S_n) >$ (meV)	σ	$\rho(S_n)$ (MeV^{-1})	η
^{151}Sm	50.00 $\pm$ 5.00	66.90$\pm$ 1.40	5.83 $\pm$ 0.58	1.38 $\pm$ 0.31 $\times 10^6$	0.90 $\pm$ 0.10

The uncertainties for both NLD and γSF in Fig. 6.9 and Fig. 6.10 are obtained by combining the parameters discussed in the Eqs. 3.27, 3.28, 3.29, 3.30 and 3.32. The upper error estimation was obtained by replacing D_0 with D_0 - ΔD_0, $< \Gamma_\gamma(S_n) >$ with $< \Gamma_\gamma(S_n) > + \Delta < \Gamma_\gamma(S_n) >$, σ with $\sigma + \Delta\sigma$ and η with $\eta + \Delta\eta$ the appropriate value of η for RMI at S_n is typically 0.8 for lower limits and 1.0 for upper limits. The lower error

estimation was obtained by replacing D_0 with $D_0 + \Delta D_0$, $< \Gamma_\gamma(S_n) >$ with $< \Gamma_\gamma(S_n) >$ - $\Delta < \Gamma_\gamma(S_n) >$, σ with σ - $\Delta\sigma$ and η with η - $\Delta\eta$. These fluctuations are important because they include the effect contributed by the uncertainties of the D_0, $< \Gamma_\gamma(S_n) >$, σ and η parameters, while the error bars acquired through the Oslo method are mainly statistical, meaning that they are mostly affected by data availability, for example high statistics will lead to smaller errors whereas low statistics will lead to larger errors. All combinations of $D_0 \pm \Delta D_0$ and $< \Gamma_\gamma(S_n) > \pm \Delta < \Gamma_\gamma(S_n) >$ were checked, table 6.2 shows the best combinations that were chosen and used to obtain low and upper limits. In addition the lower and upper limits will be used to extract the uncertainties of the SR.

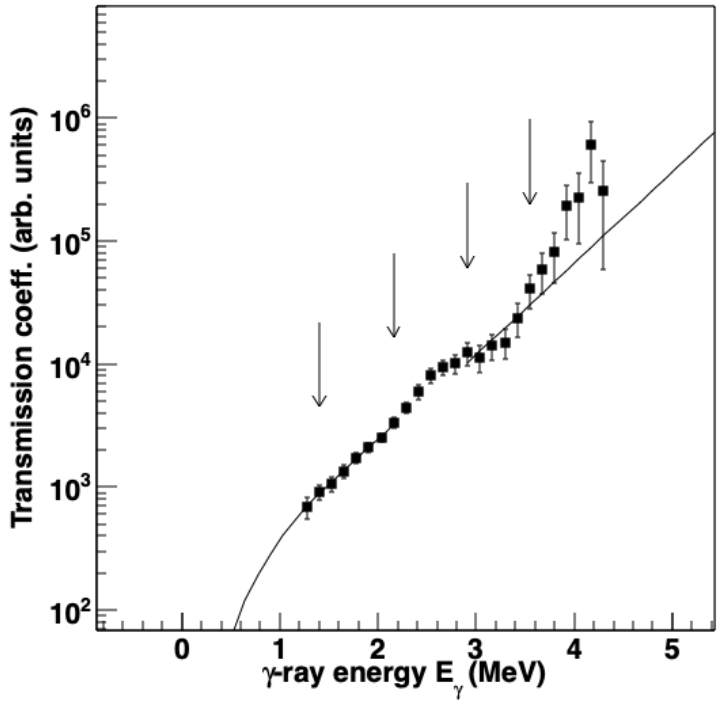


Figure 6.8: The observed γ-ray transmission coefficient of ^{151}Sm with some of the uncertainties mentioned in Tab. 6.2. The arrows indicate the normalisation points used, see text.

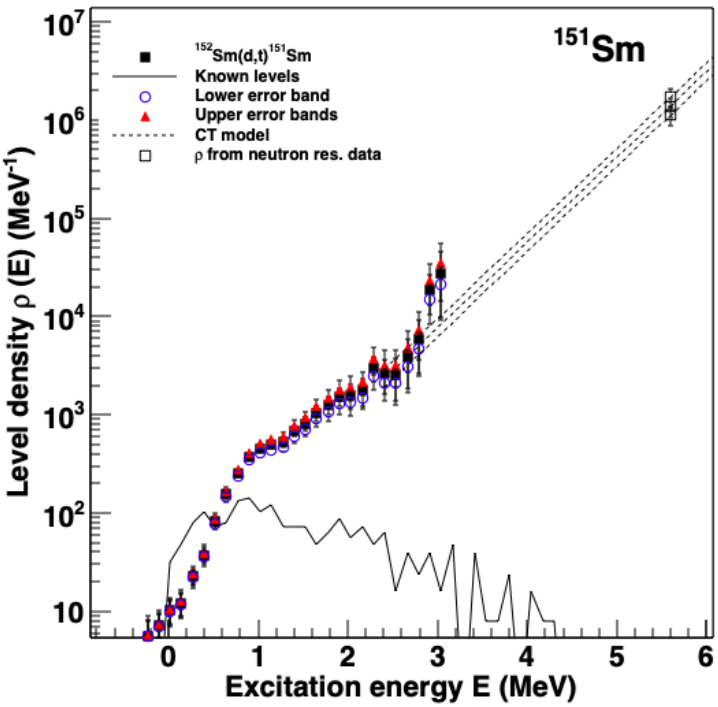


Figure 6.9: The NLD of ^{151}Sm plotted with its lower error band and upper error band, a discrepancy is observed at lower energies around 0.1 to 0.6 MeV between the current data and the known levels, see text.

Different reaction channels populate different transition states, in case of the current data transitions at low E_x are not populated by the (d,t) reaction. This explains the discrepancy observed in Fig. 6.9 at low E_x between the current experimental data and the known levels from NNDC [99].

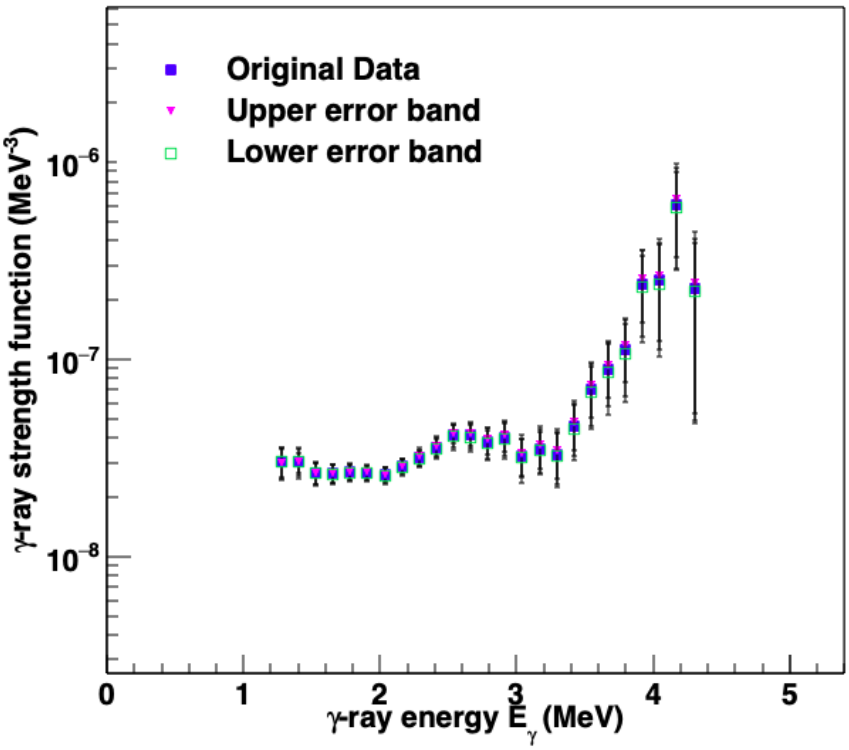


Figure 6.10: The extracted γSF of ^{151}Sm, including the lower and upper error bands from the uncertainties that are mentioned in Tab. 6.2. These show the possible location of each data point on account of all the possible uncertainties contributing to the data.

The γSF of ^{151}Sm shows the scissors resonance which was investigated between 2 and 3 MeV.
The γSF shown in Fig. 6.7, is determined through the γ-ray transmission coefficient Fig. 6.8, this relationship is given by Eqs 3.34 and 3.35.
The parameter α as indicated in Eqs 3.22 and 3.23 relates the slope of the NLD to that of the γ-ray transmission coefficient. Once the correct normalisation points for the NLD are determined, the same normalisation points are used for the γ-ray transmission coefficient which is then translated to the γSF shown in Fig.6.11.

Table 6.2: The parameters used to obtain the error bands for the NLD and γSF of ^{151}Sm.

Upper error band	
D_0 - ΔD_0(eV)	45.00
$< \Gamma_\gamma(S_n) > + \Delta < \Gamma_\gamma(S_n) >$(meV)	68.30
$\sigma + \Delta\sigma$	5.11
$\eta + \Delta\eta$	1.00
Lower error band	
$D_0 + \Delta D_0$(eV)	55.00
$< \Gamma_\gamma(S_n) >$ - $\Delta < \Gamma_\gamma(S_n) >$(meV)	65.50
σ - $\Delta\sigma$	6.89
η - $\Delta\eta$	0.80

A discontinuity of about 2 MeV is observed in Fig. 6.11 in the vicinity of the PDR, to

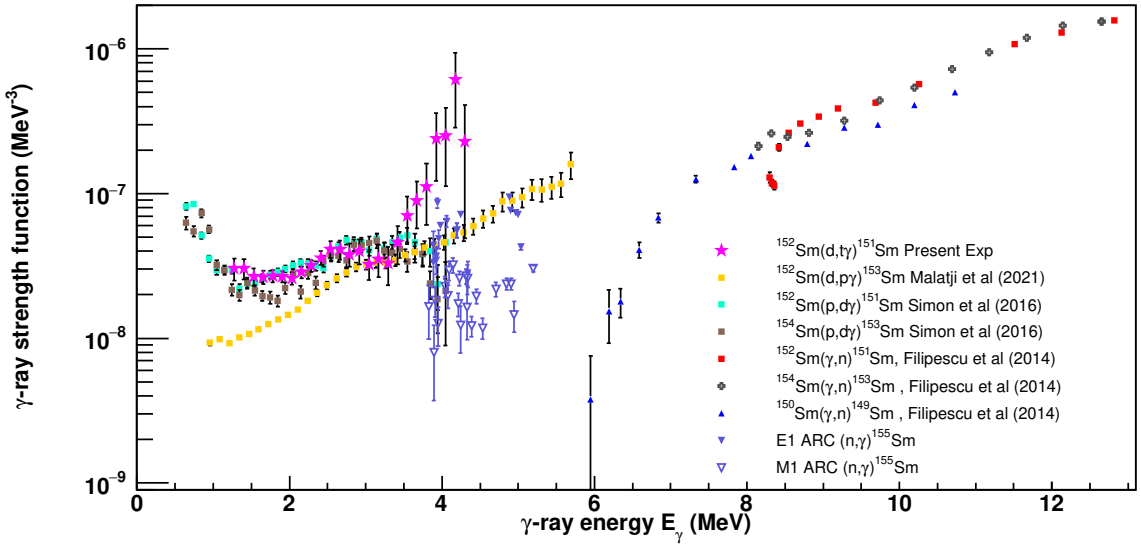


Figure 6.11: Comparison of the (d,tγ)^{151}Sm exponential γSF from the current study, with measurements of the other isotopes in the samarium isotopic chain. The data are also compared with the average resonance capture (ARC) [101] and further plotted with the Giant Electric Dipole Resonance (GEDR) [102] from the given references.

the GEDR data. This discontinuity is due to data statistics since there is no data around this energy region hence it cannot be accounted for.

6.4 Extracting the scissors resonance

The experiments analysed using the Oslo method are only capable of extracting the SR that is built on excited states in the quasi-continuum [103]. For this work the $B(M1)_{SR}$ was extracted using Eq. 2.30. The value of the integrated reduced transition strength $B(M1)_{SR}$ of magnetic dipole type was calculated and the value was found to be 2.13 μ_N^2 when determined numerically. The analysis method to extract the $B(M1)_{SR}$ uses a Standard Lorentzian function to fit the shape in the range of SR and integrate over the distribution analytically and numerically. The fit is reliable as evident in Fig. 6.12. It fits most of the SR points, that gives a reasonable estimation of the $B(M1)_{SR}$ strength. The background method used was selected because although it is less complex it produces best results, as shown in Fig. 6.12 the background was approximated using an exponential function that fitted two points in the experimental γSF, in the area of the SR. The strength of the scissors resonance can be extracted from the total strength using the resonance parameters obtained.

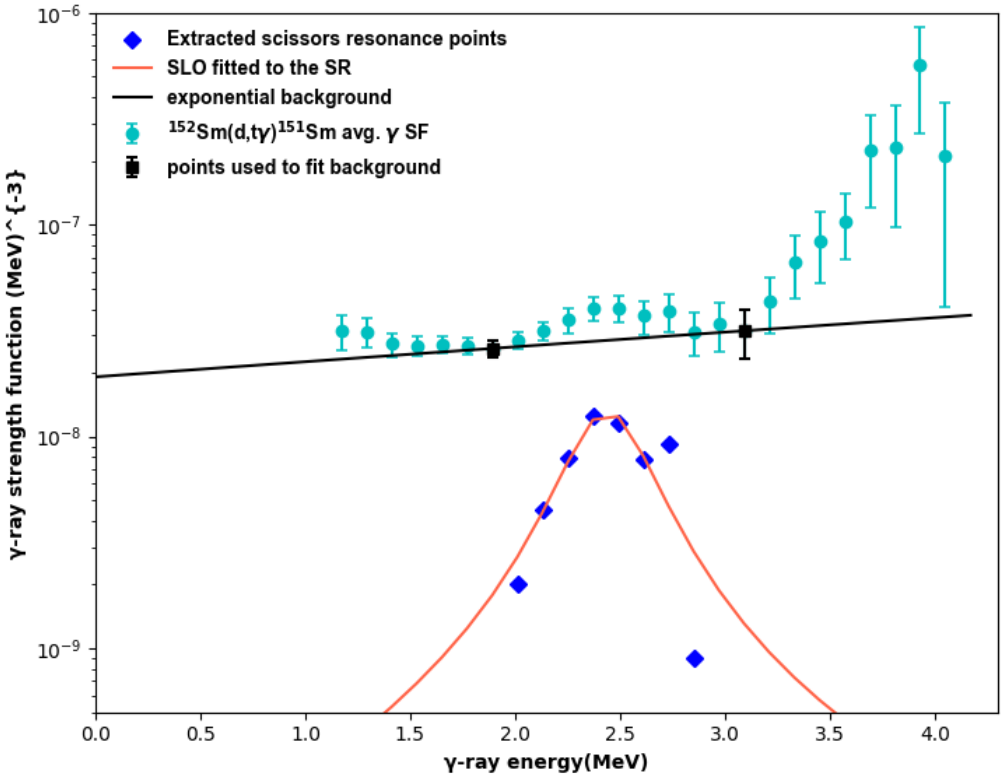


Figure 6.12: The extracted SR of ^{151}Sm, the teal circles represent the present experimental γSF, the black squares are used for background subtraction connected by the black solid line, the blue diamonds show the extracted SR and the orange line is the fit by the Standard Lorentzian function (SLO).

Chapter 7

Discussion

To obtain a reliable γ-ray strength function (γSF), it must be noted that the nuclear level density (NLD) needs to be correctly normalized. It has been noticed in all analysis using the Oslo method that the NLDs of neighboring isotopes have similar slopes [104]. The same is observed for the γSF. To make sure that the NLD is correctly normalized, the NLD from the present experiment is compared to those of previous experiments (p,dγ)^{151,153}Sm form Ref. [105], (d,pγ)^{153,155}Sm from Ref. [103], extracted using the Oslo method, as shown in Fig. 7.1. The differences noticed in Fig. 7.1, may be as a result of the different experimental setups, and different energy regions from which the various data sets were extracted.

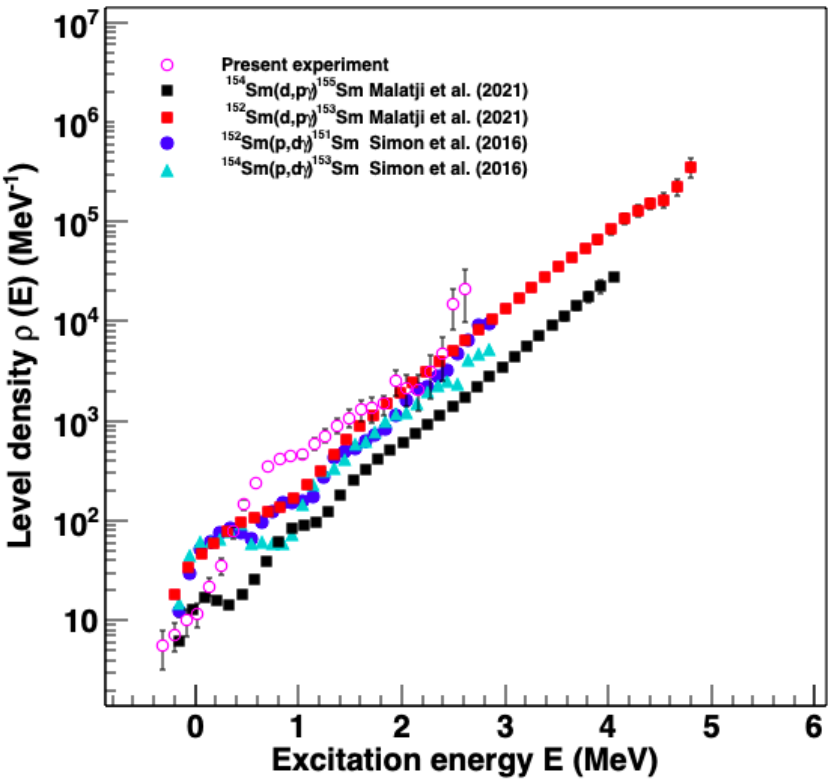


Figure 7.1: A comparison of the NLD of ^{152}Sm(d,tγ)^{151}Sm with measurements of (p,dγ)^{151,153}Sm [105] and (d,pγ)^{153,155}Sm [103].

Looking at Fig. 7.1, we see a good agreement in the slopes of the NLDs of Refs. [103,105] and present work, the NLDs are parallel. Since the NLDs compared in Fig. 7.1 are of odd-even nuclei it is an interesting fact to observe that the NLDs of ^{153}Sm and ^{151}Sm are higher than the NLD of ^{155}Sm. In general most isotopic chains studied in literature show that a more deformed nucleus will have a NLD higher than the less deformed ones, but this is not the case with the samarium isotopic chain, in particular for ^{155}Sm. This is believed to be a consequence of stronger shell and pairing effects in ^{155}Sm compared to the lighter neighboring isotopes ^{153}Sm and ^{151}Sm, which leads to the single-particle level density of ^{155}Sm at Fermi energy being smaller [103].

Around 600 keV in Fig. 7.1 there is an unexpected immediate increase on the NLD of the ^{152}Sm(d,tγ) reaction, this increase goes up to 1.1 MeV. Looking at the other NLDs slopes, since it is expected for neighboring isotopes of the same element to have similar NLDs slopes, it can be noticed that this increase is not observed.

The data compared to this work were collected using slightly different techniques and under different conditions. The maximum E_x of the data from Ref. [105] and present work goes up to approximately 3 MeV, not enough states were populated. The data from [103] has maximum E_x that goes up to 4.1 MeV for ^{155}Sm and 5 MeV for ^{153}Sm meaning the reactions populated enough energy states.

The targets were exposed to a 25MeV proton beam with 1.2 nA of intensity, the targets were both approximately 1mg/cm^2 [105]. For the ^{154}Sm(d,pγ)^{155}Sm and ^{152}Sm(d,pγ)^{153}Sm reactions from Ref. [103] the data were collected almost similarly to the one of the present experiment, as explained in Chapter 4. The data were collected at the Oslo Cyclotron Laboratory at the University of Oslo where the ^{154}Sm and ^{152}Sm targets were exposed to a 13.5 and 13 MeV beam with thickness of 2.9 and 3.2 mg/cm^2, respectively, and at a beam intensity of approximately 0.2 nA. The array of 26 NaI(Tl) detectors for γ-ray detection and the SiRi array for charged particle detection were used.

Comparing the energy and intensity of the reactions from Ref. [105] to the ones in Ref. [103] and in the present experiment, the reactions in Ref. [105] had the potential of populating a larger energy range than those in [103] and in present study. The maximum E_x reached by the data from Ref. [105] and present work is relatively small compared to the data from [103] as already mentioned in value above. Furthermore the D_0 and Γ_γ used in Ref. [105] is slightly different from the ones used in the present study. For Ref. [105] the parameters were taken from Ref. [10] and for the current study and Ref. [103] the D_0 and Γ_γ parameters were taken from Ref [100]. The use of different normalisation parameters may account for the differences noticed in the various results being compared.

In Ref. [105], the spin cut-off parameter at S_n that was used is constant with no reduction factor used at all values of E_x. The spin-cut off parameter used in the current study and Ref. [103] was reduced with a reduction factor of 0.9 at all values of E_x. The reduction factor is used to find the lower and upper limits of the spin cut-off parameter by setting it to 0.8 for lower and 1.0 for upper limits. While comparing the reaction of the present work with previous studies, it must be taken into account that the ^{152}Sm(d,tγ)^{151}Sm reaction has some limitations such as few statistics and a longer extrapolation to S_n as it is seen in Fig. 6.6. The main cause of the limitations being the fact that the experiment

was primarily not optimized to favor the ^{152}Sm(d,tγ)^{151}Sm reaction. Particularly the beam energy used was not high enough for the population of the (d,t) reaction.

Fig. 6.11 shows a comparison of the γSF of the ^{151}Sm [105], ^{153}Sm [103] and ^{155}Sm isotopes plotted with giant electric dipole resonance (GEDR) [102] and the average resonance capture (ARC) [101] data. The slopes of the γSF of ^{151,153}Sm from Ref. [105] and ^{151}Sm from this work shows good agreement at low energies and a drastic difference above 3.8 MeV, but the data from Ref. [105] has good agreement with the ARC [101] data above 3.8 MeV. The differences between the data from Ref. [105] and present work are interesting and opens research questions in the field.

The protruding area around 2.5 to 3.5 MeV is the area where the SR was extracted. Ref. [105] reports an observation of low lying energy enhancement (LEE) at low energies (1.5 MeV and below), in the present data we do observe a slight upbend at low energies in the data but because of few statistics it cannot be concluded on the existence and non existence of the LEE. The ^{153}Sm data from Ref. [103] does not show any upbend at low energies. This can be a consequence of the fact that there is no data below 1.5 MeV. In most cases [56, 105] the upbend is seen at 1.5 MeV and below. There is a contradiction between the result of Ref. [103] and Ref. [105] on the γSF of ^{153}Sm from 2 MeV and below Fig. 7.2. In Ref. [105] there is a sudden and sharp upbend whereas in Ref. [103] the data becomes more flat and does not show any potential upbend.

In Fig. 6.11 a discontinuity is noticed in the energy range 6 - 8 MeV at the tail of GEDR. This is due to no data that was collected around that energy region. Looking at the ^{153}Sm [103] data there is a clear enhancement from 4.2 MeV toward higher energies towards the PDR region. This enhancement can also be seen immediately at 3.8 MeV and higher in the present work. Since there is not enough data above 4.2 MeV and the data has big uncertainties in that energy region (between 3.8 and 4.2 MeV), claims on the availability of the PDR cannot be made. The presence of the PDR cannot be concluded on using the current experimental data.

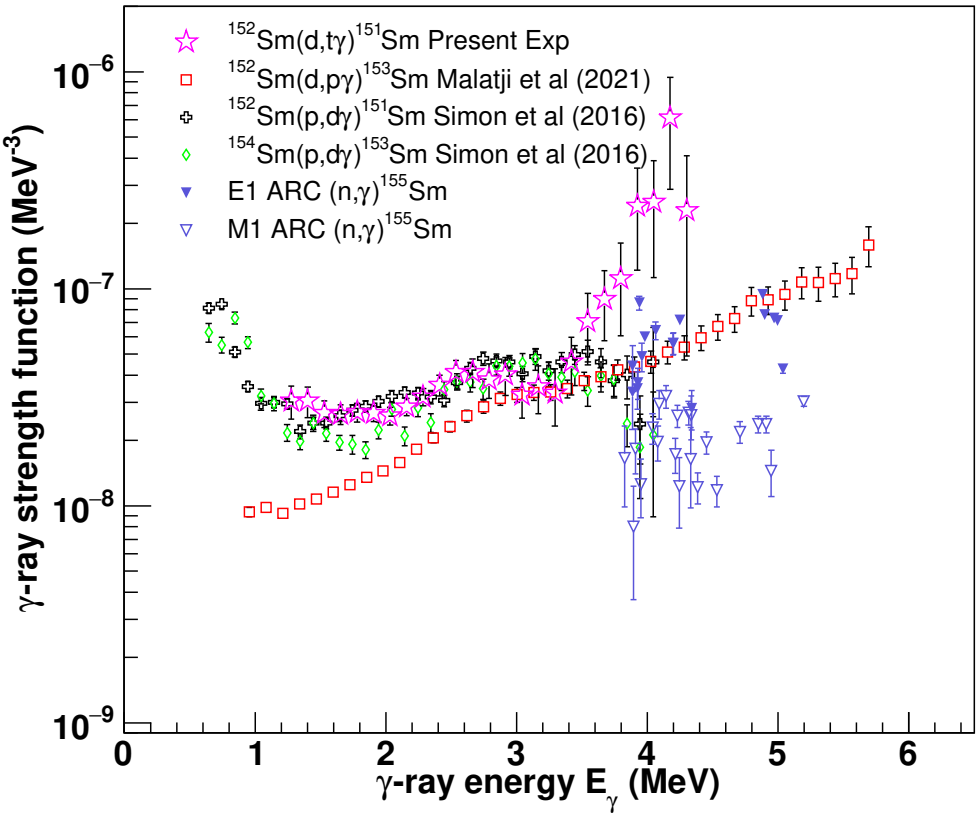


Figure 7.2: The experimental γSF from current ^{152}Sm(d,tγ)^{151}Sm reaction, plotted data from previously studied γSF as referenced on diagram

The findings of the B(M1)$_{SR}$ strength for ^{151}Sm in this work were compared with results from other studies by plotting the data on the same set of axis, see Fig. 7.3. That includes ^{144,148,150,152,154}Sm data by Ziegler *et al.* [7], and ^{153,155}Sm Oslo (CACTUS) data by Malatji *et al.* [103].
Figure 7.3 shows the B(M1) strength of neighboring samarium isotopes. It can be seen looking at the teal data from Ref. [103] that the B(M1) strength of ^{155}Sm is higher than the one of ^{153}Sm. The same is seen looking at the red data from Ref. [7] the more deformed the isotope the stronger the B(M1) value. Fig. 7.3 shows an increase in B(M1) strength increases as the A increases.

An interesting behaviour to observe is that the value of B(M1) for ^{151}Sm from this work and ^{152}Sm from Ref. [103] are larger than the B(M1) value of ^{153}Sm [103], whereas it is expected that a more deformed nucleus must have a bigger B(M1) compared to a less deformed nucleus [6, 107]. The observation between ^{152}Sm and ^{153}Sm can be explained by the fact that ^{152}Sm is even-even and ^{153}Sm is odd-even [6, 107]. This is believed to be a result of pairing. The B(M1)$_SR$ will split in odd-even nuclei such that it can be hardly detected. The splitting is caused by the unpaired particle which prompts a significant fragmentation on the M1 strength distributions [9].

The data from Ref. [7] show an increase in B(M1) with increase in deformation. In comparison with the data from [103] and present work this trend is maintained.

Table 7.1: Table showing the extracted B(M1)$_{SR}$ strength for different samarium isotopes and their respective deformation parameters β_2 taken from Ref. [106] (where $\beta_2 \approx \delta^2$), the centroid energy ω_{SR} and data references. This information is compared in Fig. 7.3

Sm Isotope	Deformation (β_2)	B_{SR}(M1) (μ_N^2)	ω_{SR} (MeV)	source of data
^{151}Sm	0.22	2.13±0.60	2.48 ± 0.25	present work
^{144}Sm	0.08	0.28±0.00	3.97± 0.4	Ziegler(1990) *et al.* [7]
^{148}Sm	0.18	0.51±0.01	3.07± 0.3	Ziegler(1990) *et al.* [7]
^{150}Sm	0.21	0.97±0.10	3.13± 0.3	Ziegler(1990) *et al.* [7]
^{152}Sm	0.24	2.35±0.20	3.00± 0.2	Ziegler(1990) *et al.* [7]
^{153}Sm	0.26	1.70±0.43	2.89± 0.0	Malatji(2021) *et al.* [103]
^{154}Sm	0.27	2.65±0.30	3.20± 0.3	Ziegler(1990) *et al.* [7]
^{155}Sm	0.27	5.42±1.00	2.98± 0.8	Malatji(2021) *et al.* [103]

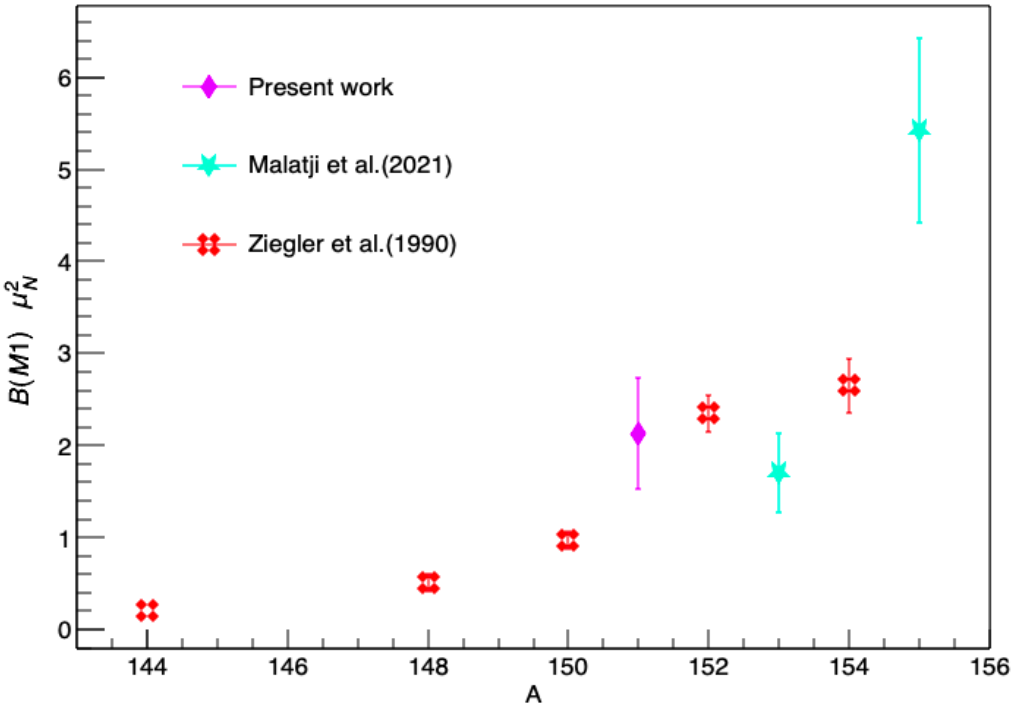


Figure 7.3: The comparison of the $B(M1)_{SR}$ strength against atomic mass number A obtained from this work (purple diamond) to teal stars [103], and red crossed squares [7]. This figure displays the trend of the B(M1) as deformation increases in the samarium isotopic chain.

Tab. 7.1 shows also the centroid energy of the SR of each isotope denoted by ω_{SR}. It is known that the SR is found at excitation energies approximated at $E_x = 66 \times \delta \times A^{-1/3}$ which is approximately at $E_x = 2 - 4$MeV for rare-earth isotopes. The centroid energy of the extracted SR from this work is 2.48 MeV which is lower than most of the centroids in the table, but this value still lies in the expected range. The theoretical value of the ^{151}Sm centroid energy, using $E_x = 66 \times \delta \times A^{-1/3}$ was found to be 2.73 MeV. This is 0.25 MeV higher than the experimental value found in this study and the theoretical value

lies within the uncertainties of the experimental value.

Chapter 8

Summary and Conclusion

8.1 Summary

The samarium (Sm) isotopic chain is one of the isotopic chains that poses good qualities such as having a fairly large number of stable isotopes, which are experimentally accessible. An experiment was performed to study the scissors resonance (SR) in the ^{151}Sm isotope.

The experiment was performed at the Oslo cyclotron laboratory (OCL) using the SiRi particle telescope and the CACTUS detector array to detect charged particles and γ-rays in coincidence, using the ^{152}Sm(d,tγ)^{151}Sm reaction. Data were collected and analysed using the Oslo method. The ^{152}Sm(d,tγ)^{151}Sm reaction was studied with the aim of extracting the statistical properties which are the nuclear level density (NLD) and γ-ray strength function (γSF) below the neutron separation energy S_n. The γSF was analysed further to extract the SR. The results of this study were then compared to results of previous studies to track the evolution of the SR in the Sm isotopic chain and the resonance's dependence on deformation of the nuclei along the chain of samarium isotopes.

The statistical properties of the ^{151}Sm nucleus were studied for the first time through the (d,tγ) reaction. The experiments were not optimised for the (d,tγ) reaction, and as a result not enough data were collected for higher excitation energies. Nevertheless the data obtained were compared to previous measurement of other Sm isotopes studied with different reactions, beam energy and analytical techniques.

The SR was successfully extracted and its strength calculated in this study and was found to be 2.13 $\pm$ 0.6 μ_N^2 and its centroid energy 2.48 MeV. Even though the SR has been studied and given a number of accepted microscopic and macroscopic descriptions, there is still a large number of interesting factors to study about the resonance, like what influences the strength of the resonance and the energies in which it is found. It is thought that the SR originates from M1 transitions in high-j orbitals of deformed nuclei [35].

8.2 Conclusion

In conclusion the aim and objectives of this work were successfully met. The SR for ^{151}Sm was extracted around excitation energy region E_x = 2.5 to 3.5 MeV and was

compared with that of other isotopes of samarium. The B(M1) is thought to increase with deformation squared, this work is in agreement with this claim. Looking at Fig. 7.3, the trend shows that the B(M1) is directly proportional to deformation squared. Few ideas to be considered for future studies are:

- Figure out the physics behind the abrupt increase in the NLD of the ^{152}Sm(d,tγ)^{151}Sm reaction at $\approx$ 600 keV.
- Studying the LEE of ^{151}Sm and its evolution along the Sm isotopic chain, by comparing it to that of the samarium isotopes already studied.
- Perform an experiment that is optimised for the population of ^{151}Sm by the ^{152}Sm(d,tγ)^{151}Sm reaction. This should be done in order to increase statistics and extend the range of the NLD and γSF to higher energies.
- Develop a rigorous technique to estimate the B(M1) uncertainties.
- Improve on the normalisation, by using different normalisation techniques and comparing the outputs to get the best results.

Bibliography

[1] Davide Castelvecchi. Proton-size puzzle leaps closer to resolution. *Nature*, 575(7782):269–270, Nov 2019.

[2] Pei-Lin You. Atoms can be divided into three categories: polar, non-polar and hydrogen atom. *arXiv preprint arXiv:1010.2425*, Oct 2010.

[3] C Jarlskog. Lord Rutherford of Nelson, his 1908 nobel prize in chemistry, and why he didn't get a second prize. In *Journal of Physics: Conference Series*, volume 136, page 012001. IOP Publishing, Nov 2008.

[4] M. Guttormsen, M. Aiche, F. L. Bello Garrote, L. A. Bernstein, D. L. Bleuel, Y. Byun, Q. Ducasse, T. K. Eriksen, F. Giacoppo, A. Görgen, F. Gunsing, T. W. Hagen, B. Jurado, M. Klintefjord, A. C. Larsen, L. Lebois, B. Leniau, H. T. Nyhus, T. Renstrøm, S. J. Rose, E. Sahin, S. Siem, T. G. Tornyi, G. M. Tveten, A. Voinov, M. Wiedeking, and J. Wilson. Experimental level densities of atomic nuclei. *The European Physical Journal A*, 51(12), Dec 2015.

[5] D. Bohle, A. Richter, W. Steffen, A. E. L. Dieperink, N. Lo Iudice, F. Palumbo, and O. Scholten. New magnetic dipole excitation mode studied in the heavy deformed nucleus ^{156}Gd by inelastic electron scattering. *Physics Letters B*, 137(1-2):27–31, Mar 1984.

[6] K. Heyde, P. von Neumann-Cosel, and A. Richter. Magnetic dipole excitations in nuclei: Elementary modes of nucleonic motion. *Reviews of Modern Physics*, 82(3):2365–2419, Sep 2010.

[7] W. Ziegler, C. Rangacharyulu, A. Richter, and C. Spieler. Orbital magnetic dipole strength in ^{148,150,152,154}Sm and nuclear deformation. *Physical Review Letters*, 65(20):2515–2518, Nov 1990.

[8] A. Wolpert, O. Beck, D. Belic, J. Besserer, P. von Brentano, T. Eckert, C. Fransen, R.-D. Herzberg, U. Kneissl, J. Margraf, H. Maser, A. Nord, N. Pietralla, and H. H. Pitz. Low-lying dipole excitations in the heavy, odd-mass nucleus ^{181}Ta. *Phys. Rev. C*, 58:765–770, Aug 1998.

[9] J. Enders, N. Huxel, P. von Neumann-Cosel, and A. Richter. Where is the Scissors Mode Strength in Odd-Mass Nuclei? *Physical Review Letters*, 79(11):2010–2013, Sep 1997.

[10] R. Capote, M. Herman, P. Obložinský, P. G. Young, S. Goriely, T. Belgya, A. V. Ignatyuk, A. J. Koning, S. Hilaire, V. A. Plujko, M. Avrigeanu, O. Bersillon, M. B. Chadwick, T. Fukahori, Z. Ge, Y. Han, S. Kailas, J. Kopecky, V. M. Maslov,

G. Reffo, M. Sin, E. Sh. Soukhovitskii, and P. Talou. RIPL – Reference Input Parameter Library for Calculation of Nuclear Reactions and Nuclear Data Evaluations. *Nuclear Data Sheets*, 110(12):3107–3214, Dec 2009, URL hhtp://www-nds.iaea.org/RIPL-3/.

[11] S. Raman, C. W. Nestor, and P. Tikkanen. Transition probability from the ground to the first-excited 2^+ state of even-even nuclides. *Atomic Data and Nuclear Data Tables*, 78(1):1–128, May 2001.

[12] A. Schiller, L. Bergholt, M. Guttormsen, E. Melby, J. Rekstad, and S. Siem. Extraction of level density and γ strength function from primary γ spectra. *Nuclear Instruments and Methods in Physics Research Section A: Accelerators, Spectrometers, Detectors and Associated Equipment*, 447(3):498–511, Jun 2000.

[13] A. C. Larsen, M. Guttormsen, M. Krtička, E. Běták, A. Bürger, A. Görgen, H. T. Nyhus, J. Rekstad, A. Schiller, S. Siem, H. K. Toft, G. M. Tveten, A. V. Voinov, and K. Wikan. Analysis of possible systematic errors in the Oslo method. *Physical Review C*, 83(3), Mar 2011.

[14] L N. Cooper. Bound electron pairs in a degenerate fermi gas. *Physical Review*, 104(4), Sep 1956.

[15] K. Kaneko, M. Hasegawa, U. Agvaanluvsan, E. Algin, R. Chankova, M. Guttormsen, A. C. Larsen, G. E. Mitchell, J. Rekstad, A. Schiller, S. Siem, and A. Voinov. Breaking of nucleon cooper pairs at finite temperature in $^{93-98}$Mo. Sep 2006.

[16] T. von Egidy and D. Bucurescu. Experimental energy-dependent nuclear spin distributions. *Physical Review C*, 80(5), Nov 2009.

[17] H. A. Bethe. An attempt to calculate the number of energy levels of a heavy nucleus. *Physical Review*, 50(4):332, Aug 1936.

[18] A. Gilbert and A. G. W. Cameron. A composite nuclear-level density formula with shell corrections. *Canadian Journal of Physics*, 43(8):1446–1496, Aug 1965.

[19] R. Razavi, N. Sharifzadeh, and M. R. Farahmand. Effective moments of inertia and spin cut off parameters in Hf isotopes. 56:282, Dec 2011.

[20] A. J. Koning, S. Hilaire, and S. Goriely. Global and local level density models. *Nuclear Physics A*, 810(1-4):13–76, Sep 2008.

[21] Arjan J Koning, Stephane Hilaire, and Marieke C Duijvestijn. Talys-1.0. In *International Conference on Nuclear Data for Science and Technology*, pages 211–214. EDP Sciences, 2007.

[22] A. Sobiczewski, S. Bjørnholm, and K. Pomorski. The moment of inertia and the energy gap of fission isomers. *Nuclear Physics A*, 202(2):274–288, Feb 1973.

[23] A. Berlaga V. Zelevinsky, S. Karampagia. Constant temperature model for nuclear level density. *Physics Letters B*, 783, Aug 2018.

[24] G. A. Bartholomew, E. D. Earle, A. J. Ferguson, J. W. Knowles, and M. A. Lone. Gamma-Ray Strength Functions. In *Advances in Nuclear Physics*, pages 229–324. Springer US, Dec 1973.

[25] K.S. Krane. *Introductory Nuclear Physics*. Wiley, 1987.

[26] Bakken. Nuclear shell model. *Wikipedia*, 2016.

[27] K. L. Malatji. *Statistical properties of deformed Samarium isotopes and constraining the nucleosynthesis of* ^{180}*Ta*. PhD thesis, Stellenbosch University, Dec 2019.

[28] N. Lo Iudice and F. Palumbo. New Isovector Collective Modes in Deformed Nuclei. *Physical Review Letters*, 41(22):1532–1534, Nov 1978.

[29] E. B. Balbutsev, I. V. Molodtsova, and P. Schuck. Experimental status of the nuclear spin scissors mode. *Physical Review C*, 97(4), Apr 2018.

[30] B. V. Kheswa. *Impact of the* ^{138,139}*La radiative strength functions and nuclear level densities on the galactic production of* ^{138}*La*. PhD thesis, Stellenbosch University, Dec 2014.

[31] A. Richter. Probing the nuclear magnetic dipole response with electrons, photons and hadrons. *Progress in Particle and Nuclear Physics*, 34:261–284, Jan 1995.

[32] S Hilaire and M Girod. The amedee nuclear structure database. In *International Conference on Nuclear Data for Science and Technology*, pages 107–110. EDP Sciences, Dec 2007.

[33] S. Goriely, S. Hilaire, and A. J. Koning. Improved microscopic nuclear level densities within the Hartree-Fock-Bogoliubov plus combinatorial method. *Physical Review C*, 78(6), Dec 2008.

[34] R. B. Firestone, Shirley V. S., Baglin C. M., Chu Frank S. Y., and J Zipkin. The 8th edition of the table of isotopes, Sep 1997.

[35] M. Guttormsen, L. A. Bernstein, A. Görgen, B. Jurado, S. Siem, M. Aiche, Q. Ducasse, F. Giacoppo, F. Gunsing, T. W. Hagen, A. C. Larsen, M. Lebois, B. Leniau, T. Renstrøm, S. J. Rose, T. G. Tornyi, G. M. Tveten, M. Wiedeking, and J. N. Wilson. Scissors resonance in the quasicontinuum of Th, Pa, and U isotopes. *Physical Review C*, 89(1), Jan 2014.

[36] T. G. Tornyi, M. Guttormsen, T. K. Eriksen, A. Görgen, F. Giacoppo, T. W. Hagen, A. Krasznahorkay, A. C. Larsen, T. Renstrøm, S. J. Rose, S. Siem, and G. M. Tveten. Level density and γ-ray strength function in the odd-odd ^{238}Np nucleus. *Physical Review C*, 89(4), Apr 2014.

[37] R. Schwengner, G. Winter, W. Schauer, M. Grinberg, F. Becker, P. Von Brentano, J. Eberth, J. Enders, T. Von Egidy, R-D Herzberg, et al. Two-phonon j= 1 states in even-mass Te isotopes with A = 122–130. *Nuclear Physics A*, 620(3):277–295, Jul 1997.

[38] N. Pietralla, C. Fransen, D. Belic, P. Von Brentano, C. Frießner, U. Kneissl, A. Linnemann, A. Nord, H. H. Pitz, T. Otsuka, et al. Transition rates between mixed symmetry states: First measurement in ^{94}Mo. *Physical Review Letters*, 83(7):1303, Aug 1999.

[39] H Maser, N Pietralla, P Von Brentano, R-D Herzberg, U Kneissl, J Margraf, H H Pitz, and A Zilges. Observation of the 1^+ scissors mode in the γ-soft nucleus ^{134}Ba. *Physical Review C*, 54(5):R2129, Nov 1996.

[40] P Von Brentano, J Eberth, J Enders, L Esser, R-D Herzberg, N Huxel, H Meise, P von Neumann-Cosel, N Nicolay, N Pietralla, et al. First observation of the scissors mode in a γ-soft nucleus: The case of ^{196}Pt. *Physical Review Letters*, 76(12):2029, Mar 1996.

[41] A. Richter. Shell model and magnetic dipole modes in deformed nuclei. *Nuclear Physics A*, 507(1):99–128, Jan 1990.

[42] Noritaka Shimizu. Nuclear shell-model code for massive parallel computation (kshell). *arXiv preprint arXiv:1310.5431*, Oct 2013.

[43] J. E. Midtbø, A. C. Larsen, T. Renstrøm, F. L. Bello Garrote, and E. Lima. Consolidating the concept of low-energy magnetic dipole decay radiation. *Physical Review C*, 98(6), Dec 2018.

[44] K. Heyde and C. De Coster. Correlation between E2 and M1 transition strength in even-even vibrational, transitional, and deformed nuclei. *Phys. Rev. C*, 44:R2262, Dec 1991.

[45] R.R. Hilton, W. Höhenberger, and P. Ring. Magnetic dipole response in rare earth nuclei. *The European Physical Journal A-Hadrons and Nuclei*, 1(3):257–260, Mar 1998.

[46] P. Sarriguren, E. Moya De. Guerra, R Nojarov, and Amand Faessler. M1 spin strength distribution in ^{154}Sm. *Journal of Physics G: Nuclear and Particle Physics*, 19(2):291, Feb 1993.

[47] A Richter. Proceedings of the 4th international spring seminar on nuclear physics: The building blocks of nuclear structure. 1994.

[48] W. H. Dickhoff. Connection between brueckner ladders and pairing correlations. *Physics Letters B*, 210(1-2):15–19, Aug 1988.

[49] Christiaan De Coster, Kristiaan Heyde, and A Richter. Magnetic dipole spin excitations in rare-earth and actinide nuclei. *Nuclear Physics A*, 542(3):375–409, Jun 1992.

[50] D. Frekers, H. J. Wörtche, A. Richter, R. Abegg, R.E. Azuma, A. Celler, C. Chan, TE Drake, R. Helmer, K. P. Jackson, et al. Spin excitations in the deformed nuclei ^{154}Sm, ^{158}Gd and ^{168}Er. *Physics Letters B*, 244(2):178–182, Jul 1990.

[51] D Zawischa and J Speth. Orbital and spin-flip magnetic dipole resonances in heavy nonspherical nuclei. *Nuclear Physics A*, 569(1-2):343–352, Mar 1994.

[52] E. Litvinova and N. Belov. Low-energy limit of the radiative dipole strength in nuclei. *Physical Review C*, 88(3), Sep 2013.

[53] R. Schwengner, S. Frauendorf, and A. C. Larsen. Low-Energy Enhancement of Magnetic Dipole Radiation. *Physical Review Letters*, 111(23), Dec 2013.

[54] B. A. Brown and A. C. Larsen. Large Low- Energy M1 Strength for ^{56,57}Fe within the Nuclear Shell Model. *Physical Review Letters*, 113(25), Dec 2014.

[55] A. Voinov, E. Algin, U. Agvaanluvsan, T. Belgya, R. Chankova, M. Guttormsen, G. E. Mitchell, J. Rekstad, A. Schiller, and S. Siem. Large Enhancement of Radiative Strength for Soft Transitions in the Quasicontinuum. *Physical Review Letters*, 93(14), Sep 2004.

[56] M. Wiedeking, L. A. Bernstein, M. Krtička, D. L. Bleuel, J. M. Allmond, M. S. Basunia, J. T. Burke, P. Fallon, R. B. Firestone, B. L. Goldblum, R. Hatarik, P. T. Lake, I-Y. Lee, S. R. Lesher, S. Paschalis, M. Petri, L. Phair, and N. D. Scielzo. Low-Energy Enhancement in the Photon Strength of ^{95}Mo. *Physical Review Letters*, 108(16), Apr 2012.

[57] A. C. Larsen, S. Goriely, A. Bürger, M. Guttormsen, A. Görgen, S. Harissopulos, M. Kmiecik, T. Konstantinopoulos, A. Lagoyannis, T. Lönnroth, K. Mazurek, M. Norrby, H. T. Nyhus, G. Perdikakis, A. Schiller, S. Siem, A. Spyrou, N. U. H. Syed, H. K. Toft, G. M. Tveten, and A. Voinov. Primary γ-ray spectra in ^{44}Ti of astrophysical interest. *Physical Review C*, 85(1), Jan 2012.

[58] A. Bürger, A. C. Larsen, S. Hilaire, M. Guttormsen, S. Harissopulos, M. Kmiecik, T. Konstantinopoulos, M. Krtička, A. Lagoyannis, T. Lönnroth, K. Mazurek, M. Norrby, H. T. Nyhus, G. Perdikakis, S. Siem, A. Spyrou, and N. U. H. Syed. Nuclear level density and γ-ray strength function of ^{43}Sc. *Physical Review C*, 85(6), Jun 2012.

[59] N. U. H. Syed. *Nuclear structure and statistical decay properties of closed and near closed shell nuclei*. PhD thesis, University of Oslo, 2009.

[60] M. Guttormsen, A. Bürger, T. E. Hansen, and N. Lietaer. The SiRi particle-telescope system. *Nuclear Instruments and Methods in Physics Research Section A: Accelerators, Spectrometers, Detectors and Associated Equipment*, 648(1):168–173, Aug 2011.

[61] A. C. Larsen, R. Chankova, M. Guttormsen, F. Ingebretsen, S. Messelt, J. Rekstad, S. Siem, N. U. H. Syed, S. W. Ødegård, T. Lönnroth, A. Schiller, and A. Voinov. Microcanonical entropies and radiative strength functions of ^{50,51}V. *Physical Review C*, 73(6), Jun 2006.

[62] M. Guttormsen, R. Chankova, U. Agvaanluvsan, E. Algin, L. A. Bernstein, F. Ingebretsen, T. Lönnroth, S. Messelt, G. E. Mitchell, J. Rekstad, A. Schiller, S. Siem, A. C. Sunde, A. Voinov, and S. Ødegård. Radiative strength functions in $^{93-98}$Mo. *Physical Review C*, 71(4), Apr 2005.

[63] R. Schwengner, S. Frauendorf, and B. A. Brown. Low-Energy Magnetic Dipole Radiation in Open-Shell Nuclei. *Physical Review Letters*, 118(9), Mar 2017.

[64] B. V. Kheswa, M. Wiedeking, F. Giacoppo, S. Goriely, M. Guttormsen, A. C. Larsen, F. L. Bello Garrote, T. K. Eriksen, A. Görgen, T. W. Hagen, P. E. Koehler, M. Klintefjord, H. T. Nyhus, P. Papka, T. Renstrøm, S. Rose, E. Sahin, S. Siem, and T. Tornyi. Galactic production of ^{138}La: Impact of ^{138,139}La statistical properties. *Physics Letters B*, 744:268–272, May 2015.

[65] A. C. Larsen, J. E. Midtbø, M. Guttormsen, T. Renstrøm, S. N. Liddick, A. Spyrou, S. Karampagia, B. A. Brown, O. Achakovskiy, S. Kamerdzhiev, D. L. Bleuel, A. Couture, L. Crespo Campo, B. P. Crider, A. C. Dombos, R. Lewis, S. Mosby, F. Naqvi, G. Perdikakis, C. J. Prokop, S. J. Quinn, and S. Siem. Enhanced low-energy γ-decay strength of ^{70}Ni and its robustness within the shell model. *Physical Review C*, 97(5), May 2018.

[66] A. C. Larsen, M. Guttormsen, N. Blasi, A. Bracco, F. Camera, L. Crespo Campo, T. K. Eriksen, A. Görgen, T. W. Hagen, V. W. Ingeberg, B. V. Kheswa, S. Leoni, J. E. Midtbø, B. Million, H. T. Nyhus, T. Renstrøm, S. J. Rose, I. E. Ruud, S. Siem, T. G. Tornyi, G. M. Tveten, A. V. Voinov, M. Wiedeking, and F. Zeiser. Low-energy enhancement and fluctuations of γ-ray strength functions in ^{56,57}Fe: test of the Brink-Axel hypothesis. *Journal of Physics G: Nuclear and Particle Physics*, 44(6):064005, Apr 2017.

[67] M. Goldhabar and E.Teller. *Physics Rev*, 74(1046), 1948.

[68] R.B Firestone. The origin of the giant dipole resonance. (21.10.-k, 20.10.Ma, 21.10.Hw, 24.60.-K), Jul 2021.

[69] L. M. Donaldson, C. A. Bertulani, J. Carter, V. O. Nesterenko, P. von Neumann-Cosel, R. Neveling, V. Yu. Ponomarev, P. G. Reinhard, I. T. Usman, P. Adsley, et al. Deformation dependence of the isovector giant dipole resonance: The neodymium isotopic chain revisited. *Physics Letters B*, 776:133–138, Jan 2018.

[70] J. Kopecky and M. Uhl. Test of gamma-ray strength functions in nuclear reaction model calculations. *Physical Review C*, 41(5):1941–1955, May 1990.

[71] J. Kopecky, M. Uhl, and R.E. Chrien. Radiative strength in the compound nucleus ^{157}Gd. *Physical Review C*, 47(1):312, Jan 1993.

[72] A. C. Larsen. *Statistical properties in the quasi-continuum of atomic nuclei*. PhD thesis, University of Oslo, May 2008.

[73] N. Nelson, Y. Azmy, R. P. Gardner, J Mattingly, R Smith, L.G. Worrall, and S. Dewji. Validation and uncertainty quantification of detector response functions for a 1×2 nai collimated detector intended for inverse radioisotope source mapping applications. *nuclear instruments and methods in physics research b*, 410(1-15), Nov 2017.

[74] L. Crespo Campo et al. Statis- tical γ -decay properties of ^{64} Ni and deduced (n,γ) cross section of the s -process branch- point nucleus ^{63}Ni. *Physc rev C*, 94(4), Oct 2016.

[75] https://sites.google.com/site/puenggphysics/home/unit-iv/compton-effect accessed november 2021.

[76] http://electrons.wikidot.com/pair-production-and-annihilation. accessed november 2021 mse 5317.

[77] G. F. Knoll. *Radiation detection and measurement*. John Wiley & Sons, Inc., 3rd ed. edition, 2000.

[78] M. Guttormsen, T. S. Tveter, L. Bergholt, F. Ingebretsen, and J. Rekstad. The unfolding of continuum γ-ray spectra. *Nuclear Instruments and Methods in Physics Research Section A: Accelerators, Spectrometers, Detectors and Associated Equipment*, 374(3):371–376, Jun 1996.

[79] J. Rekstad, A. Henriquez, F. Ingebretsen, G. Midttun, B. Skaali, R. Øyan, J. Wikne, T. Engeland, T.F. Thorsteinsen, E. Hammaren, et al. A study of the nuclear structure at high energy and low spin. *Physica Scripta*, 1983(T5):45, Dec 1983.

[80] M. Guttormsen, T. Ramsøy, and J. Rekstad. The first generation of γ-rays from hot nuclei. *Nuclear Instruments and Methods in Physics Research Section A: Accelerators, Spectrometers, Detectors and Associated Equipment*, 255(3):518–523, Apr 1987.

[81] A. Bohr and B. Mottelson. *Nuclear Structure*, volume 1. New York, 1969.

[82] L. Henden, L. Bergholt, M. Guttormsen, J. Rekstad, and T. S. Tveter. On the relation between the statistical γ-decay and the level density in ^{162}Dy. *Nuclear Physics A*, 589(2):249–266, Jul 1995.

[83] D. M. Brink. Individual particle and collective aspects of the nuclear photoeffect. *Nuclear Physics*, 4:215–220, Aug 1957.

[84] P. Axel. Electric Dipole Ground-State Transition Width Strength Function and 7-Mev Photon Interactions. *Physical Review*, 126(2):671–683, Apr 1962.

[85] T. von Egidy and D. Bucurescu. Erratum: Systematics of nuclear level density parameters [Phys. Rev. C 72, 044311 (2005)]. *Physical Review C*, 73(4), Apr 2006.

[86] F. Giacoppo, F.L. Bello Garrote, L.A. Bernstein, D.L. Bleuel, R.B. Firestone, A. Görgen, M. Guttormsen, T. W. Hagen, M. Klintefjord, P. Edward Koehler, et al. γ decay from the quasicontinuum of ^{197,198}Au. *Physical Review C*, 91(5):054327, May 2015.

[87] U Agvaanluvsan, GE Mitchell, JF Shriner Jr, and M Pato. Parity dependence of nuclear level densities. *Physical Review C*, 67(6):064608, Jun 2003.

[88] A. C. Larsen, M. Guttormsen, R. Chankova, F. Ingebretsen, T. Lönnroth, S. Messelt, J. Rekstad, A. Schiller, S. Siem, N. U. H. Syed, and A. Voinov. Nuclear level densities and γ-ray strength functions ^{44,45}Sc. *Physical Review C*, 76(4), Oct 2007.

[89] N. U. H. Syed, A. C. Larsen, A. Bürger, M. Guttormsen, S. Harissopulos, M. Kmiecik, T. Konstantinopoulos, M. Krtička, A. Lagoyannis, T. Lönnroth, K. Mazurek, M. Norby, H. T. Nyhus, G. Perdikakis, S. Siem, and A. Spyrou. Extraction of thermal and electromagnetic properties in ^{45}Ti. *Physical Review C*, 80(4), Oct 2009.

[90] U Agvaanluvsan, A Schiller, JA Becker, LA Bernstein, PE Garrett, M Guttormsen, GE Mitchell, J Rekstad, S Siem, A Voinov, et al. Level densities and γ-ray strength functions in ^{170,171,172}Yb. *Physical Review C*, 70(5):054611, Nov 2004.

[91] U. Agvaanluvsan, A.C Larsen, R. Chankova, M. Guttormsen, G.E. Mitchell, A. Schiller, S. Siem, and A. Voinov. Enhanced radiative strength in the quasi-continuum of ^{117} Sn. *Physical Review Letters*, 102(16):162504, Apr 2009.

[92] M. Guttormsen, A. Atac, G. Løvhøiden, S. Messelt, T. Ramsøy, J. Rekstad, T. F. Thorsteinsen, T. S. Tveter, and Z. Zelazny. Statistical Gamma-Decay at Low Angular Momentum. *Physica Scripta*, T32:54–60, Jan 1990.

[93] *The homepage of the Oslo Cyclotron Laboratory (OCL)*, 2019.

[94] M. Guttormsen, A. C. Larsen, A. Bürger, A. Görgen, S. Harissopulos, M. Kmiecik, T. Konstantinopoulos, M. Krtička, A. Lagoyannis, T. Lönnroth, K. Mazurek, M. Norrby, H. T. Nyhus, G. Perdikakis, A. Schiller, S. Siem, A. Spyrou, N. U. H. Syed, H. K. Toft, G. M. Tveten, and A. Voinov. Fermi's golden rule applied to the γ decay in the quasicontinuum of ^{46}Ti. *Physical Review C*, 83(1), Jan 2011.

[95] K. L. Malatji. Nuclear level densities and gamma-ray strength functions in Ta isotopes and nucleo-synthesis of ^{180}Ta. Master's thesis, University of the Western Cape, Feb 2016.

[96] Vetle W. Ingeberg. oslocyclotronlab/Qkinz: Qkinz kinematics calculator, Jan 2018.

[97] H. Bethe. Bremsformel für Elektronen relativistischer Geschwindigkeit. *Zeitschrift für Physik*, 76(5-6):293–299, May 1932.

[98] J. F. Ziegler. Stopping of energetic light ions in elemental matter. *Journal of Applied Physics*, 85(3):1249–1272, Feb 1999.

[99] Brookhaven National Laboratory, USA, as of September 2018. *Data extracted from NuDat database on the National Nuclear Data Center*, 2019.

[100] S. F. Mughabghab. Recommended Thermal Cross Sections, Resonance Properties, and Resonance Parameters for Z = 62–102. In *Atlas of Neutron Resonances*, pages 89–822. Elsevier, Nov 2018.

[101] J. Kopecky, S. Goriely, S. Péru, S. Hilaire, and M. Martini. E1 and M1 strength functions from average resonance capture data. *Physical Review C*, 95(5), May 2017.

[102] D. M. Filipescu, I. Gheorghe, H. Utsunomiya, S. Goriely, T. Renstrøm, H. T. Nyhus, O. Tesileanu, T. Glodariu, T. Shima, K. Takahisa, S. Miyamoto, Y. W. Lui, S. Hilaire, S. Péru, M. Martini, and A. J. Koning. Photoneutron cross sections for samarium isotopes: Toward a unified understanding of (γ,n) and (n,γ) reactions in the rare earth region. *Physical Review C*, 90(6), Dec 2014.

[103] K. L. Malatji, K. S. Beckmann, M. Wiedeking, S. Siem, S. Goriely, A. C. Larsen, Kursad O Ay, F. L. Bello Garrote, L Crespo Campo, A. Görgen, et al. Statistical properties of the well deformed ^{153,155}Sm nuclei and the scissors resonance. *Physical Review C*, 103(1):014309, Jan 2021.

[104] L. G. Moretto, A. C. Larsen, F. Giacoppo, M. Guttormsen, and S. Siem. Experimental First Order Pairing Phase Transition in Atomic Nuclei. *Journal of Physics: Conference Series*, 580:012048, Feb 2015.

[105] A. Simon, M. Guttormsen, A. C. Larsen, C. W. Beausang, P. Humby, J. T. Burke, R. J. Casperson, R. O. Hughes, T. J. Ross, J. M. Allmond, R. Chyzh, M. Dag, J. Koglin, E. McCleskey, M. McCleskey, S. Ota, and A. Saastamoinen. First observation of low-energy γ-ray enhancement in the rare-earth region. *Physical Review C*, 93(3), Mar 2016.

[106] P Möller, Arnold John Sierk, Takatoshi Ichikawa, and Hiroyuki Sagawa. Nuclear ground-state masses and deformations: Frdm (2012). *Atomic Data and Nuclear Data Tables*, 109:1–204, May 2016.

[107] N. Pietralla, P. von Brentano, R.-D. Herzberg, U. Kneissl, N. Lo Iudice, H. Maser, H. H. Pitz, and A. Zilges. Systematics of the excitation energy of the 1^+ scissors mode and its empirical dependence on the nuclear deformation parameter. *Physical Review C*, 58(1):184–190, Jul 1998.

Appendix A

Extra figures

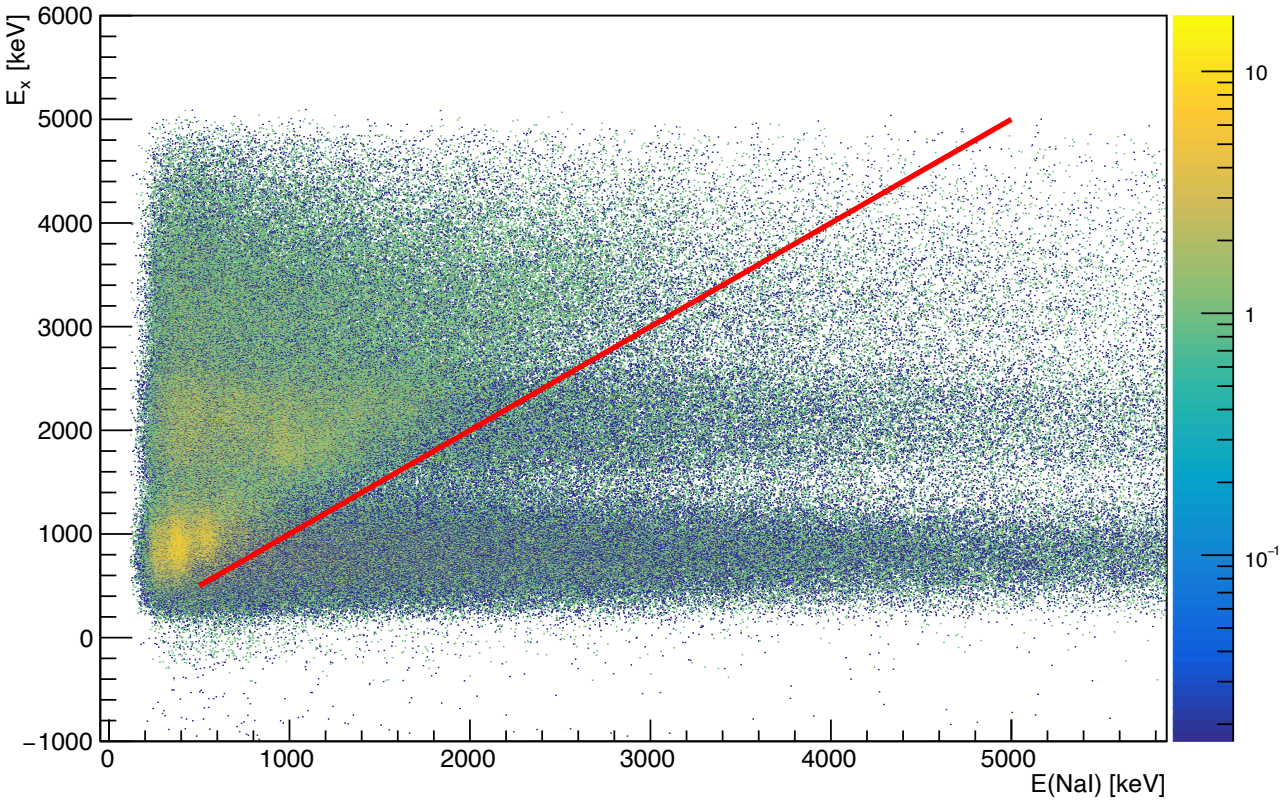


Figure A.1: The ^{151}Sm raw matrix with the red line representing decays to ground state where $E_g = E_x$

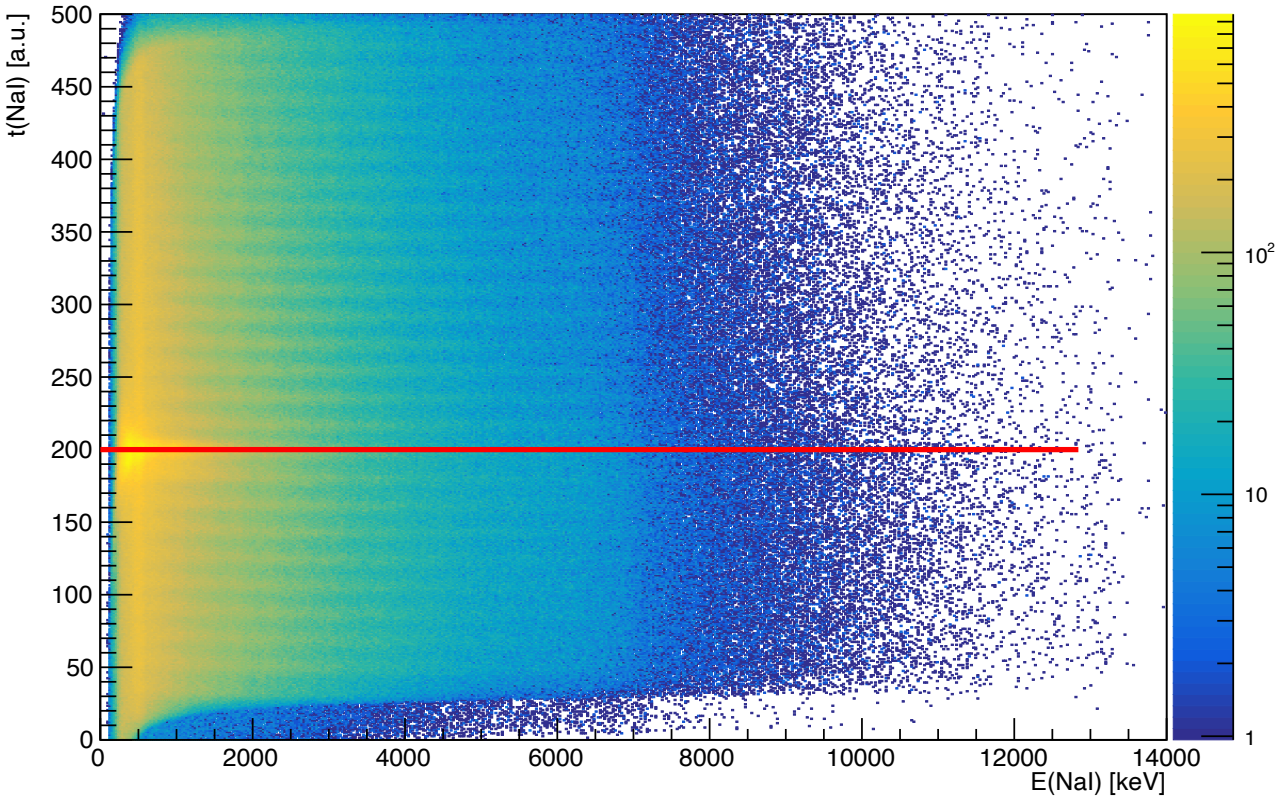


Figure A.2: The ^{152}Sm(d,tγ) energy vs time matrix for the NaI(Tl) detectors after being corrected for the time walk effect, with the red line showing the accuracy of the walk effect on the main events.